Doctoral Dissertations 1896 - February 2014

1-1-1986

A vibrational study of high performance fiber and a model composite/

Peter K. Kim
University of Massachusetts Amherst

Follow this and additional works at: https://scholarworks.umass.edu/dissertations_1

A VIBRATIONAL STUDY OF HIGH PERFORMANCE FIBER
AND A MODEL COMPOSITE

A Dissertation Presented

By

Peter K. Kim

Submitted to the Graduate School of the
University of Massachusetts in partial fulfillment
of the requirements for the degree of

DOCTOR OF PHILOSOPHY

September 1986

Polymer Science and Engineering

iii

A VIBRATIONAL STUDY OF HIGH PERFORMANCE POLYMERIC FIBERS
AND A MODEL COMPOSITE

.

A Dissertation Presented

by

Peter K. Kim

Approved as to style and content by:
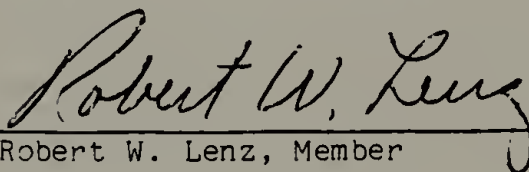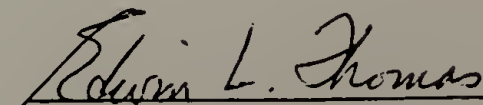
_____

Shaw Ling Hsu, Chairperson of Committee

_____

Richard J. Farris, Member

_____

Robert W. Lenz, Member

_____

Edwin L. Thomas, Head
Polymer Science and Engineering

To my parents and Yoonjung

ACKNOWLEDGEMENTS

I would first like to acknowledge the help, guidance, and inspiration that I received from my thesis advisor, Professor Shaw Ling Hsu. I would also like to thank Professor R.J. Farris for his constructive criticism and encouragement, especially during composite studies. Sincere contribution of Professor R.W. Lenz is also greatly appreciated.

I would like to thank other professors and the students, particularly Dave Waldman and Larry Coyne for their advice and friendship.

I wish to express my gratitude to the University of Massachusetts-Industry Research on Polymers (CUMIRP) and the Santos Go Memorial Foundation for their financial support.

I would also like to extend my thanks to Marilyn Putnam and Sue Rusiecki who helped me to put this thesis together.

This thesis is my gift to Yoonjung whose many sacrifices, life-giving decisions, and unending love have enabled me to start and to complete this degree.

Finally, I thank my family, especially my parents and Yoonjung's parents for their continuous support and encouragement during my education.

ABSTRACT

A VIBRATIONAL STUDY OF HIGH PERFORMANCE FIBER
· AND A MODEL COMPOSITE

(September 1986)

Peter K. Kim, B.S. Massachusetts Institute of Technology
Ph.D. University of Massachusetts

Directed by: Professor Shaw Ling Hsu

Vibrational characteristics of poly(p-phenylene terephthalamide) (PPTA) and its model compound, benzanilide, are analyzed. Normal coordinate analysis of these molecules was done in terms of specific non-redundant coordinates to overcome the difficulties usually encountered in defining an appropriate force field using internal coordinates. Satisfactory assignments were made for the bands above 900 cm^{-1} without any refinements in the force constants previously calculated for smaller molecules. Poorly defined spectroscopic features of highly ordered PPTA were explained by the difference in local environments of the same chemical groups in the repeat unit. The theoretical modulus of PPTA was calculated to be 241 GPa.

In order to study the deformation behavior of these high performance fibers in a composite, we have developed a combined spectroscopic-mechanical technique using polydiacetylene single crystal

fiber as a model for reinforcement fiber. This technique has high spacial resolution, frequency-strain coefficient, and selective sensitivity to the fiber alone. The strain distribution along the fiber axis was measured using a Raman spectrometer. The existance, magnitude, and effects of residual strains due to curing reaction and differences in the thermal expansion coefficients and moduli between the fiber and the matrix were evaluated.

TABLE OF CONTENTS

LIST OF TABLES

LIST OF FIGURES

C H A P T E R   I

INTRODUCTION

I.1 HIGH PERFORMANCE POLYARAMID FIBER: PPTA

In engineering applications where weight is a critical factor, the advantage of low density and high modulus/strength organic polymeric fiber is apparent. Furthermore, it has been established that the incorporation of these fibers in a polymer matrix can significantly improve the mechanical properties of the composites [1,2]. For the future development of these fibers and their applications in composites, it is important to understand in detail their structure-property relationships and deformation behaviors under various conditions.

In recent years there has been active research and development of high performance organic fibers. Currently, there are two very different types of organic polymers which have been shown to exhibit these desired high mechanical properties. These two classes of polymers are based either on rod-like aromatic polymers or on the flexible chain polymers [3-5]. The molecular basis for the high modulus, however, is identical for both types of polymers. In fact, when oriented and extended, any polymer, including the flexible type, will typically exhibit high modulus [6-8]. On the other hand, the fiber strength achievable and the characteristics of its transverse properties will

1

depend on the specificity and the magnitude of the lateral ordering of the oriented molecules. Since polymer chains are oriented parallel to each other, the strong covalent bonds lie almost entirely in the direction of the chain. Therefore, the strength in this direction is directly dependent upon the bond strength and the continuity of polymer chains. Lateral strength then becomes dependent on the much weaker secondary forces such as dipole-dipole interactions, van der Waals forces and the number and strength of hydrogen bonds. If a highly ordered state with strong mutual interactions between fiber structural units can be achieved, then the favorable force distribution among the components via transverse coupling will cause these polymers to ultimately exhibit high transverse strength as well as high modulus.

As a result of the possibility of the high processing efficiency of rigid-rod polymers relative to that of flexible polymers, rigid-rod polymers that can form liquid crystalline states are particularly attractive as candidates for the development of high performance materials. There has been a number of studies concerning synthesis, structure-property relationships, and mechanical and rheological properties of several aromatic, rigid-rod polymers [9-15]. The most common polymer of these type is poly(p-phenylene terephthalamide) (PPTA),
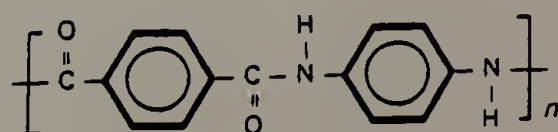
which is marketed under the tradename Kevlar[R] by E.I. duPont de Nemours
and Co. PPTA is a condensation polymer of terephthaloyl chloride and
p-phenylene diamine [16-18]. In general, the formation of fibers from
these rigid-rod polymers involves several steps: (1) dissolution in
strong acids such as chlorosulfonic acid, methane sulfonic acid, or
sulfuric acid to form a lyotropic liquid crystalline solution, (2)
extrusion of this solution through a spinneret, where the liquid
crystalline domains are oriented in the direction of the shear, and
stretching in an air gap before entering a coagulation bath, (3) washing
and neutralization of the spun fiber, and (4) post-processing heat
treatment. Therefore, in order to quantitatively deduce the structure-
property relationships, knowledge of the molecular structure in
solution, polymer-solvent interaction, chain segment orientation, and
the nature, specificity, and magnitude of the intermolecular
interactions are all important from both the practical and fundamental
viewpoints.

It has been suggeted that PPTA fibers are consisted of fibrils of
roughly 600 nm in diameter [19]. Within the fibrils of Kevlar[R], the
extended chains exist laterally as hydrogen-bonded sheets that are
regularly pleated along their long axis and arranged radially [19-21].
The fibrils are fully crystalline with a monoclinic unit cell structure
[22]. The hydrogen-bonded, extended chain morphology exhibits
exceptionally high longitudinal tensile properties [23-25]. For
example, Kevlar[R] 49 filaments exhibit an ultimate tensile strength of
2860 MPa and Young's modulus of 124 GPa at a density of 1.45 g/cm^3,

which compares very favorably with high tensile strength graphite

filament (3170 MPa, 248 GPa, 1.8 g/cm^3) [26]. Also the fibers are

highly anisotropic in radial-to-longitudinal stiffness and tensile

strength [27,28]. Compressive strength of PPTA filaments is also

substantially lower than tensile strength because of the weak lateral

ordering as seen in the loop tests [29-32]. Compressive yielding

manifests itself virtually as a kink band. For PPTA, kink bands occur

at 0.53% [30], very close to its compressive yield strain value.

DeTeresa has studied microstructural models of compressive behavior of

these highly anisotropic fibers [30], but there has not been much work

in the analysis of stress induced changes of PPTA at the molecular level

both in tension and in compression.

X-ray diffraction suggests two crystal modifications for the

regenerated PPTA films which are prepared by first dissolving Kevlar[R] 29

fiber in 100% sulfuric acid. Then thin film of this solution is made by

coagulating the thin coating of this solution in various solvents.

Modification I, which constitutes Kevlar[R] 49 fiber, is formed by

coagulating the polymer solution in methanol [22,33,34]. Haraguchi and

his coworkers reported another crystal structure of PPTA, modification

II, for the polymer solution coagulated in water [35]. In addition, for

samples prepared from low polymer concentration solution, modification

II is readily transformed into modification I by thermal annealing.

Characterizations of these two crystal modifications will be informative

in understanding the microstructure-property relationship of PPTA since

these two crystal modifications show very different mechanical

properties as well. For example, modification I shows brittle fracture whereas modification II shows ductile deformation behavior upon tensile deformation [36]. These two different deformation behaviors have been attributed to the orientation and the strength of the hydrogen-bonded sheets with respect to the film plane [36]. There are differences observed in the far-infrared spectra of these two modifications as well. Low frequency vibrations occuring between 400 cm^{-1} to 20 cm^{-1} are generally delocalized in nature and may be quite sensitive to both the specificity and the magnitude of intermolecular interactions. Stress induced frequency and intensity changes of the vibrational bands of PPTA in the mid-infrared region have been observed as well [37,38]. Therefore, understanding the vibrational spectra of these regenerated PPTA films as a function of temperature, crystal modification, and lateral order would be useful for study of these intermolecular interactions and their influence to the mechanical properties in conjunction with the available X-ray data. Also, it may be possible to study the stress-strain behavior of PPTA at the molecular level using a spectroscopic-mechanical technique.

Vibrational spectroscopy has been profitably employed to study microstructures and their changes during deformation. In many polymers vibrational spectra exhibit absorption bands which can be assigned to vibrations of specific chain segments or chemical groups. If band assignments are properly established and, additionally, if the directions of the corresponding transition moments with respect to the chain axis are known, then vibrational spectroscopy offers the unique

advantage in that the stress induced changes in orientation, conformation, and packing of the polymer chains can all be measured with a combined spectroscopic-mechanical technique [39-42]. However, in order to use vibrational techniques to study the microstructures and the stress induced molecular deformations of PPTA, one must first have complete understanding of its vibrational characteristics. Spectroscopic characterization of PPTA has been quite limited because of its complex chemical structure, experimental difficulties, and fundamental problems associated with redundant coordinates in the normal coordinate analysis of molecules as complex as PPTA [35,43-45].

The main objective of the first part of this thesis is to analyze the vibrational characteristics of PPTA and to apply the result to study both the structure-property relationships of PPTA and its molecular deformation behavior using vibrational spectroscopy.

I.2 HIGH PERFORMANCE STRUCTURAL COMPOSITES

There has been great interest in the application of high modulus/strength fibers like PPTA as a reinforcement in structural composites where strong mechanical properties and lightweight are important considerations [46,47]. Based on use, the most common reinforcing fibers are presently glass, graphite, and polyaramids. Among them, the utilization of graphite and polyaramid reinforced composites for high performance structural applications are rapidly

increasing. Furthmore, there is an increase in the use of short fibers as reinforcement components in the polymer matrix in order to produce complex composite geometries and to use the existing flow molding technology. Epoxy resins are generally used as the matrix in the majority of high performance composites.

The properties of these fiber-reinforced composites depend upon the individual properties of the fiber, the resin, and the interphase between them [48]. In development of high performance composites, the objective is to distribute the stress in the composite so that the stronger reinforcement fibers will be subjected to the majority of the applied load. For continuous fiber reinforced composites, load is applied directly to these fibers so that the resultant stress is constant over the whole length of the fiber, while little load is carried by the matrix in deformations parallel to the fiber axis. For discontinuous fiber reinforced composites, both fiber and matrix carry a considerable amount of the load and the relative amounts are determined by the stress transfer characteristics of the interphase and matrix. The applied stress is transferred from the matrix to the fiber by the formation of shear stress at the interface. When a composite is stressed in the direction parallel to the fiber, the axial displacements in the fiber and matrix near fiber ends will differ due to the differences in elastic moduli between them. Therefore, shear stresses are developed at the interface in the direction of the fiber. Interface bond strength is determined by a large number of physical and chemical factors [49-52]. The interdependancy of these molecular factors

complicate the analysis of the nature and the performance of the interphase. Because of the difficulties in defining the interface or interphase regions, and in characterizing the specific interactions possible at the interface, the experimental studies of the composite interface and its influence on the composite properties have been limited.

Many theoretical studies of the stress transfer using simplified physical models are available in order to determine the relative importance of various physical and chemical parameters of the interphase and the matrix [53-56]. Because of the complexity due to the discontinuities of the fiber ends, various degrees of simplifying assumptions were necessary in all of these theoretical studies in order to obtain closed form solutions. All these theories are fundamentally based upon the shear-lag analysis wherein the stress transfer across the interface occurs due to the shear stress buildup at the interface. The major assumptions made in these studies consist of perfect bonding at the interface, no stress transfer through the fiber ends, isotropic linear elastic stress-strain behavior of the constituents, homogeneity of the matrix properties, and regular or repeating arrays of fibers. Recently, advances in computational techniques using finite element analysis have significantly improved the theoretical understanding of the reinforcement mechanism of fibers in composites, by studying the effect of fiber end geometry, interphase layer, non-perfect bonding at the interface, plasticity of the interphase and matrix, and the stress concentrations present in the form of defects at the interface [57-61].

Currently, there have been many experimental studies to test these theories by measuring the stress distributions in the matrix with photoelastic techniques [62-65]. Although the objective of the fiber reinforcements is to maximize the load carried by the fibers, there has not as yet been any extensive studies on the direct method of determining the stress on the fiber embedded in a matrix. Direct measurement of stress distributions in the reinforced fiber would provide additional data for further theoretical analysis to better understand the reinforcement mechanism of composites

In addition to applied mechanical stress, temperature changes and/or curing process can generate local stresses at or near the interface as well as in the bulk. Polymers are usually processed at high temperature to facilitate processing. Therefore when these fabricated parts are allowed to cool, residual stresses will inevitably build up because of differences in the thermal expansion behavior between the fiber and the matrix, and due to the volume shrinkage that occurs during curing or crystallization [66,67]. These residual stresses will superimpose over the externally applied stresses and can cause erratic or premature composite failures [68-70]. Such residual stresses may influence the fiber/matrix interfacial properties and thus the overall composite properties as a result of possible slip that can occur at the interface when the residual stress reaches a critical value. But, if controlled properly, the compressive residual stresses can actually be advantageous since the frictional bonding at the interface is proportional to the compressive force normal to the

interface [71,72]. Although the importance of these residual stresses on the composite properties has been realized for a long time, there have been few studies undertaken to explicitly understand the effect of residual stresses on the overall composite properties at the fiber-matrix level [73-75].

Similar to the theoretical analyses of the stress distribution in composites subjected to the external loads, there has been a number of thermoelastic analyses and experimental studies in the literature regarding the study of residual stresses [76-81]. Recently, the effect of anisotropy of the fiber and the interphase layer has been taken into consideration in the thermoelastic analyses as well [82,83]. However, as previously mentioned, there has been only limited experimental study of the residual stress distribution in the matrix utilizing only photoelastic techniques [55,57-59] and in particular the effect of the residual stresses on fiber and the integrity of the interphase has not been well understood.

Therefore, in the second part of this thesis, development of a combined of spectroscopic-mechanical technique that can selectively probe the strain distribution in the fiber embedded in a matrix is presented. For this study, a model composite is chosen, consisted of a single polydiacetylene single crystal fiber as a reinforcement embedded in a epoxy matrix. Its application to study the deformation behavior of a fiber incorporated in an epoxy resin as a function of both the tensile strain and the residual strain due to curing and differences in the thermal expansion coefficients are discussed as well.

C H A P T E R   II

NORMAL COORDINATE ANALYSIS OF BENZANILIDE: A MODEL COMPOUND
FOR POLY(p-PHENYLENE TEREPHTHALAMIDE)

II.1   INTRODUCTION

Although it is generally agreed that the vibrational spectroscopy

is a valuable technique in studying the structure-property relationship

of a polymer at the molecular level, the vibrational spectroscopic

characterization of PPTA has been quite limited [43-45]. This has been

primarily due to the lack of both the experimental data and the

theoretical normal coordinate analysis. The second cause is serious and

is mainly due to the lack of transferable force field. Normal

coordinate analysis is a theoretical calculation that uses the atomic

masses, the geometry of the molecule, and the force constants that

describe the potential energy of the molecule to calculate the normal

mode vibrational frequencies and displacements of atoms involved in each

calculated normal modes [84]. Normal coordinate analysis is normally

done using the internal coordinates because it is easier to recognize

the vibrational motions in terms of these coordinates and the force

constants in terms of these coordinates are somewhat more meaningful.

The internal coordinates are defined as bond stretching, various types

of angle bending, and bond torsions. There are $3n-4$ independent

coordinates for the complete description of the vibrational motions of a

polymer with n atoms in its translational repeat unit. But, for complex

11

molecules such as PPTA, the internal coordinate system contains more than this in order to preserve its local symmetry because of the presence of a considerable number of branching and cyclic redundancies. This naturally increases the number of force constants that are needed for the normal coordinate analysis.

The usual practice is to transfer parts of force field from other molecules to analyze more complicated molecules. However, this cannot be done easily for PPTA. When redundant coordinates are used in the normal coordinate analysis, not only is a large number of force constants necessary, but also the force field is really indeterminant for complicated molecules such as PPTA. An extreme example has been given by Groner and Gunthard [85]: the two force field matrices shown below

$$
\begin{bmatrix}
F_a & 0 & 0 \\
0 & F_b & 0 \\
0 & 0 & F_c
\end{bmatrix}
\quad (1)
\qquad
\begin{bmatrix}
0 & \frac{1}{2}(F_a+F_b) & -\frac{1}{2}(F_a+F_c) \\
-\frac{1}{2}(F_a+F_b) & 0 & \frac{1}{2}(F_b+F_c) \\
-\frac{1}{2}(F_a+F_c) & -\frac{1}{2}(F_b+F_c) & 0
\end{bmatrix}
\quad (2)
$$

yield the same set of vibrational frequencies, if the three coordinates a, b, and c are related by the redundancy condition, a+b+c=0. In other words, without affecting the eigenvalues (frequencies) and eigenvectors (atomic displacements) calculated from secular equations, the force constants associated with redundant coordinates in a different set of potential energy fields are related to each other by an arbitrary

constant [see Appendix A]. Therefore, one should be extremely wary when transfering force fields from one molecule to another or to use them for other types of calculations when the redundancy of the internal coordinates used has not been considered.

In this study, we analyzed the vibrational motions of PPTA using non-redundant coordinates in the normal coordinate analysis. In order to construct a set of non-redundant coordinates and to test the transferability of both these non-redundant coordinates and the associated force field, we first carried out a normal coordinate analysis on a model compound of PPTA, benzanilide. Also, by analyzing this model compound, we can test the applicability of these coordinates and the force fields to describe the vibrational motions of the amide group and benzene ring when they are connected. The chemical structure of benzanilide is shown in Figure 1. We constructed a set of non-redundant coordinates for the benzene ring and the amide group separately before combining them. The force constants for benzene ring and amide group are derived earlier theoretical studies on benzene [86] and polypeptide [87]. The construction of non-redundant coordinates for the benzene ring and the amide group, and the results of the normal coordinate analysis of benzanilide will be presented in this chapter.

II.2   NORMAL COORDINATE ANALYSIS

II.2.1   Structure and Symmetry

The exact structure of the model compound, benzanilide, has been given by Kashino and his coworkers [88]. It has a non-planar configuration with a dihedral angle of approximately $\pm 30^{\circ}$ between the benzene ring and the amide plane, similar to the measured PPTA structure [43]. These internal dihedral angles were deduced by considering the resonance effect trying to stabilize coplanarity of the amide group and the benzene rings and the counter-acting steric hindrance found between the oxygen and ortho-hydrogen of the adjacent benzene ring, and between the amide hydrogen and ortho-hydrogen of the other ring [43]. The structural parameters for benzanilide used in our analysis are listed in Table 1. The structural parameters are also shown in Figure 1.

As mentioned earlier, for convenience or for preservation of molecular local symmetry, experimental force fields are often expressed in terms of the internal coordinates which usually include redundant coordinates in the normal coordinate analysis. This procedure causes physically identical force fields to assume different numerical forms in different redundant coordinates. Another aspect of redundancy is the introduction of such high correlations between force constants of some internal coordinates making the refinement of force fields difficult, or even worse, meaningless. For these reasons, the use of redundant coordinates actually causes the resultant force fields to be less

TABLE 1

Structural Parameters of a Proposed Geometry of Benzanilide

Length (A)		Valence Angle (°)		Dihedral Angle (°)	
C–C	1.397	<(CCC)	120	τ(CCCC)	180
C–H	1.084	<(CCH)	120	τ(CCCH)	0
N–H	1.084	<(CCN)	120	τ(C_4C_5HN)	30
C–N	1.420	<(CCC')	120	τ(C_4C_5NH)	210
N–C'	1.340	<(CNH)	120	τ(HNC'O)	0
C'–O	1.240	<(CNC')	125	τ(NC'$C_{16}C_{21}$)	210
C'–C*	1.470	<(CC'O)	120	τ(OC'$C_{16}C_{21}$)	30
		<(NC'C)	117		

*   C' = carbonyl carbon
    C = benzene ring carbon

Figure 1.   Schematic diagram of the chemical structure of benzanilide.
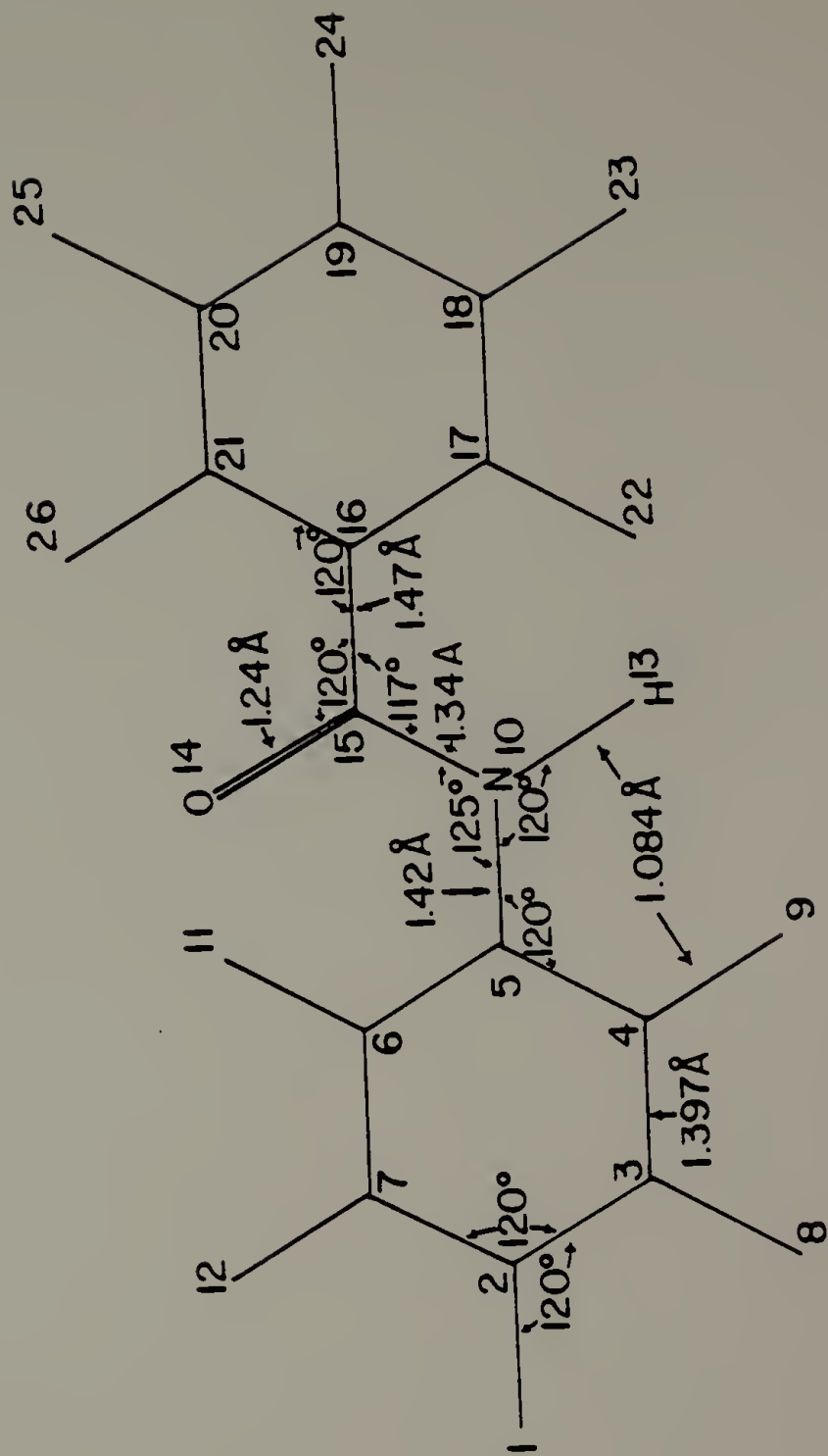
Figure 1.

transferable among the related molecules. This problem of redundancy is particularly serious for PPTA and its model compounds because, in addition to branching redundancies, cyclic redundancies exist for the benzene rings. For each n-membered cyclic molecules, the usual internal coordinates used for a cyclic molecules, i.e. n bond stretching, n angle bending, and n bond torsional coordinates, contain six redundant coordinates since there are only 3n-6 independent coordinates. These cyclic redundancy conditions introduce very high correlations among the internal coordinates involved and consequently among the force constants for the benzene rings. In order to simplify our normal coordinate analysis, we decided to analyze benzanilide in parts by separating it into two monosubstituted benzene rings and an amide group, -CONH-, and PPTA by separating it into two para-substituted benzene rings and two amide groups. Furthermore, all calculations are based on individual sets of non-redundant coordinates. This procedure greatly simplifies the vibrational analysis in two ways: first, the force field and the associated coordinates for each part are readily available from previous calculations and, second, the identification of the normal vibrations is much more easily accomplished by selecting the proper non-redundant coordinates.

In general there are two methods to obtain non-redundant coordinates for a complex molecule with low symmetry. The first method is quite suitable for computer calculations and this has been proposed by Gussoli and Zerbi [89]. Because of the redundancy conditions, the dynamic matrix, G, is a singular matrix. Then all redundant internal

$$S_2 = \frac{1}{\sqrt{6}} \ (2\Delta\phi_3 - \Delta\phi_1 - \Delta\phi_2)$$

coordinates can be identified by finding the eigenvectors which belong to zero eigenvalues of G. Once these redundant coordinates are available, other desired non-redundant orthonormal coordinates are obtained by using the Gram-Schmidt orthogonalization process. The advantage of this method is that the whole procedure can be done by computer and can be applied regardless of the complexity of the molecule and the number and type of redundancies. The major disadvantage is that these non-redundant coordinates formed may have considerable mixing of internal coordinates, making the vibrational motions too complicated to recognize. A second method which may not be generally applicable to all molecules involves locating the local redundancies and then removing them by using local symmetry coordinates [90]. Therefore, one can overcome the disadvantage of the first method by selecting the proper linear combinations of internal coordinates so that each constructed non-redundant symmetry coordinate will be easier to visualize. We adopted this method in our analysis.

For the benzene ring, branching redundancies can easily be removed by using the following local symmetry coordinates.

$$S_1 = \frac{1}{\sqrt{2}} \ (\Delta\phi_1 - \Delta\phi_2) \tag{3}$$

$$S_2 = \frac{1}{\sqrt{6}} \ (2\Delta\phi_3 - \Delta\phi_1 - \Delta\phi_2) \tag{4}$$

where $\Delta\phi_1$, $\Delta\phi_2$, and $\Delta\phi_3$ are the changes in the valence angles around each carbon of the benzene ring. The additional six cyclic redundancies for each benzene ring are more difficult to remove since there is no unique set of non-redundant coordinates. Therefore, it is advantageous to choose a set that describes the vibrational motions of the molecule most clearly. For benzene, we adopted the set described by Pulay et al. [86]. Each monosubstituted benzene ring has 42 internal coordinates, including 12 bond stretchings, 18 angle bendings, 6 torsions, and 6 out-of-plane bendings. Subtracting the 12 redundancies (6 branching and 6 cyclic) from the total number of internal coordinates, there should be 30 non-redundant coordinates as expected. The definitions of each coordinates are the same as those in the reference 5 except for out-of-plane bending coordinates, for which the definition by Abe and Krimm [91] is used.

For the amide group, two branching redundancies are removed by the use of local symmetry coordinates as described above. The convention for the in-plane bending, out-of-plane bending, and torsion coordinates of the amide group have been defined by Abe and Krimm previously [91]. Only skeletal atoms of the amide group are used for the three torsion coordinates between two rings.

In summary, 98 internal coordinates can be used to describe vibrational motions of benzanilide, but only 72 of them are independent. The 26 redundancies consist of two from the amide group and 24 from the two monosubstituted benzene rings. The complete set of internal coordinates and the associated non-redundant coordinates used for our

benzanilide analysis are listed in Tables 2 and 3. The definitions of the non-redundant coordinates are also shown schematically in Figure 2.

II.2.2   Force Field

In our analysis, the force field associated with benzene rings were obtained from Pulay and his coworkers [86]. This set was chosen since it is most complete. These values are based on ab initio calculations and agree quite well with the ones refined to a series of benzene derivatives [92]. The force constant changes needed for benzanilide due to differences between CC(O) and CN bonds connecting the amide group to each benzene ring were quite minor. Force constants involving the stretching, in-plane bending, and out-of-plane bending modes of these connecting bonds were taken from the corresponding values for monosubstituted benzene rings [92]. The force constants for the amide group were transferred from the work by Dwivedi and Krimm for a series of polypeptides [87]. The entire set of force constants are listed in Table 4. All normal coordinate analysis were performed using Wilson's GF matrices with a set of programs modified from the earlier ones by Schachtschneider and Snyder [93].

II.3   EXPERIMENTAL

The benzanilide used in this study was purchased from Aldrich Chemical Company and recrystallized in EtOH three times. Deuterated benzanilide was prepared by placing the purified benzanilide into a small glass vial. The platlet crystals were heated until completely melted. A few drops of D_2O were added to the hot glass vial, immediately saturating the container. The container was then cooled in order to crystallize the model compound. This simple procedure resulted in more than 90% deuteration. Since only one exchange site exists, i.e. secondary amine hydrogen of the amide group, no complications such as NHD groups arise. Spectral subtraction by FTIR and computerized Raman spectrometers yielded well-separated spectra for deuterated species without interference from the hydrogenated species.

Infrared spectra were obtained for samples in potassium bromide. In each case, very high signal to noise ratios were obtained using an International Business Machine model 98 spectrometer. Raman spectra of benzanilide and its EtOH solution were taken with a Jobin-Yvon HG.2S spectrometer. This instrument can be controlled by a Cromenco System III computer. The data are transferred to the Nicolet Fourier transform instrument computer or IBM 9000 computer for further analysis.

The infrared and Raman spectra of benzanilide are shown in Figures 3 and 4, respectively. The Raman spectra of benzanilide in EtOH solution are shown in Figure 5. The difference infrared and Raman spectra obtained for the deuterated benzanilide are shown in Figure 6.

TABLE 2

Definitions of Internal Coordinates

Stretching

		Atoms
R_1	= r(C-H)	(2,1)
R_2	= r(C-H)	(3,8)
R_3	= r(C-H)	(4,9)
R_4	= r(C-N)	(5,10)
R_5	= r(C-H)	(6,11)
R_6	= r(C-H)	(7,12)
R_7	= r(C-C)	(2,3)
R_8	= r(C-C)	(3,4)
R_9	= r(C-C)	(4,5)
R_{10}	= r(C-C)	(5,6)
R_{11}	= r(C-C)	(6,7)
R_{12}	= r(C-C)	(7,2)
R_{13}	= r(N-H)	(10,13)
R_{14}	= r(N-C')	(10,15)
R_{15}	= r(C'-O)	(15,14)
R_{16}	= r(C'-C)	(15,16)
R_{17}	= r(C-H)	(17,22)
R_{18}	= r(C-H)	(18,23)
R_{19}	= r(C-H)	(19,24)
R_{20}	= r(C-H)	(20,25)
R_{21}	= r(C-H)	(21,26)
R_{22}	= r(C-C)	(16,17)
R_{23}	= r(C-C)	(17,18)
R_{24}	= r(C-C)	(18,19)
R_{25}	= r(C-C)	(19,20)
R_{26}	= r(C-C)	(20,21)
R_{27}	= r(C-C)	(21,16)

TABLE 2 (continued)

Angle bending

			Atoms
R_{28}	=	<(CCH)	(7,2,1)
R_{29}	=	<(HCC)	(1,2,3)
R_{30}	=	<(CCH)	(2,3,8)
R_{31}	=	<(HCC)	(8,3,4)
R_{32}	=	<(CCH)	(3,4,9)
R_{33}	=	<(HCC)	(9,4,5)
R_{34}	=	<(CCN)	(4,5,10)
R_{35}	=	<(NCC)	(10,5,6)
R_{36}	=	<(CCH)	(5,6,11)
R_{37}	=	<(HCC)	(11,6,7)
R_{38}	=	<(CCH)	(6,7,12)
R_{39}	=	<(HCC)	(12,7,2)
R_{40}	=	<(CCC)	(7,2,3)
R_{41}	=	<(CCC)	(2,3,4)
R_{42}	=	<(CCC)	(3,4,5)
R_{43}	=	<(CCC)	(4,5,6)
R_{44}	=	<(CCC)	(5,6,7)
R_{45}	=	<(CCC)	(6,7,2)
R_{46}	=	<(CNH)	(5,10,13)
R_{47}	=	<(HNC')	(13,10,15)
R_{48}	=	<(CNC')	(5,10,15)
R_{49}	=	<(NC'O)	(10,15,14)
R_{50}	=	<(OC'C)	(14,15,16)
R_{51}	=	<(NC'C)	(10,15,16)
R_{52}	=	<(CCC')	(21,16,15)
R_{53}	=	<(C'CC)	(15,16,17)
R_{54}	=	<(CCH)	(16,17,22)
R_{55}	=	<(HCC)	(22,17,18)
R_{56}	=	<(CCH)	(17,18,23)
R_{57}	=	<(HCC)	(23,18,19)
R_{58}	=	<(CCH)	(18,19,20)
R_{59}	=	<(HCC)	(24,19,20)
R_{60}	=	<(CCH)	(20,21,26)
R_{61}	=	<(HCC)	(25,20,21)
R_{62}	=	<(CCH)	(20,21,26)
R_{63}	=	<(HCC)	(26,21,16)
R_{64}	=	<(CCC)	(21,16,17)
R_{65}	=	<(CCC)	(16,17,18)
R_{66}	=	<(CCC)	(17,18,19)
R_{67}	=	<(CCC)	(18,19,20)
R_{68}	=	<(CCC)	(19,20,21)
R_{69}	=	<(CCC)	(20,21,16)

TABLE 2 (continued)

Out-of-Plane Bending[*]

		Atoms
R_{70} = CH opb		(2,1,7,3)
R_{71} = CH opb		(3,8,2,4)
R_{72} = CH opb		(4,9,3,5)
R_{73} = CN opb		(5,10,4,6)
R_{74} = CH opb		(6,11,5,7)
R_{75} = CH opb		(7,12,6,2)
R_{76} = NH opb		(10,13,15,5)
R_{77} = C'O opb		(15,14,16,10)
R_{78} = CC' opb		(16,15,21,17)
R_{79} = CH opb		(17,22,16,18)
R_{80} = CH opb		(18,23,17,19)
R_{81} = CH opb		(19,24,18,20)
R_{82} = CH opb		(20,25,19,21)
R_{83} = CH opb		(21,26,20,16)

Torsion

	Atoms
R_{84} = C-C tor	(2,3)
R_{85} = C-C tor	(3,4)
R_{86} = C-C tor	(4,5)
R_{87} = C-C tor	(5,6)
R_{88} = C-C tor	(6,7)
R_{89} = C-C tor	(7,2)
R_{90} = C-N tor	(10,5)
R_{91} = N-C' tor	(15,10)
R_{92} = C'-C tor	(16,15)
R_{93} = C-C tor	(16,17)
R_{94} = C-C tor	(17,18)
R_{95} = C-C tor	(18,19)
R_{96} = C-C tor	(19,20)
R_{97} = C-C tor	(20,21)
R_{98} = C-C tor	(21,16)

* opb definitions of the ring differ from ref. 10 by a multiplication factor of sin(<CCC).

TABLE 3

Definition of Local Non-Redundant Symmetry Coordinates for Benzanilide

	Notation	Ring A
C-H str	r	$S_1 = R_1$
C-H str		$S_2 = R_2$
C-H str		$S_3 = R_3$
C-H str		$S_4 = R_5$
C-H str		$S_5 = R_6$
C-N str	r'	$S_6 = R_4$
C-C str	R	$S_7 = R_7$
C-C str		$S_8 = R_8$
C-C str		$S_9 = R_9$
C-C str		$S_{10} = R_{10}$
C-C str		$S_{11} = R_{11}$
C-C str		$S_{12} = R_{12}$
CH ipb	β	$S_{13} = (R_{29}-R_{28})/\sqrt{2}$
CH ipb		$S_{14} = (R_{31}-R_{30})/\sqrt{2}$
CH ipb		$S_{15} = (R_{33}-R_{32})/\sqrt{2}$
CH ipb		$S_{16} = (R_{37}-R_{36})/\sqrt{2}$
CH ipb		$S_{17} = (R_{39}-R_{38})/\sqrt{2}$
CN ipb	β'	$S_{18} = (R_{35}-R_{34})/\sqrt{2}$
trigonal def.	q_{19}	$S_{19} = (R_{40}-R_{41}+R_{42}-R_{43}+R_{44}-R_{45})/\sqrt{6}$
asy. def. A	q_{20}	$S_{20} = (2R_{40}-R_{41}-R_{42}+2R_{43}-R_{44}-R_{45})/\sqrt{12}$
asy. def. B	q_{21}	$S_{21} = (R_{41}-R_{42}+R_{44}-R_{45})/2$
CH opb	γ	$S_{22} = R_{70}$
CH opb		$S_{23} = R_{71}$
CH opb		$S_{24} = R_{72}$
CH opb		$S_{25} = R_{74}$
CH opb		$S_{26} = R_{75}$
CN opb	γ'	$S_{27} = R_{73}$
puckering	q_{28}	$S_{28} = (R_{84}-R_{85}+R_{86}-R_{87}+R_{88}-R_{89})/\sqrt{6}$
asy. tor. A	q_{29}	$S_{29} = (-R_{84}+R_{86}-R_{87}+R_{89})/2$
asy. tor. B	q_{30}	$S_{30} = (-R_{84}+2R_{85}-R_{86}-R_{87}+2R_{88}-R_{89})/\sqrt{12}$

TABLE 3 (continued)

	Notation	Ring B
C-H str	r	$S_{31} = R_{17}$
C-H str		$S_{32} = R_{18}$
C-H str		$S_{33} = R_{19}$
C-H str		$S_{34} = R_{20}$
C-H str		$S_{35} = R_{21}$
C-C' str	r''	$S_{36} = R_{16}$
C-C str	R	$S_{37} = R_{22}$
C-C str		$S_{38} = R_{23}$
C-C str		$S_{39} = R_{24}$
C-C str		$S_{40} = R_{25}$
C-C str		$S_{41} = R_{26}$
C-C str		$S_{42} = R_{27}$
CH ipb	β	$S_{43} = (R_{55}-R_{54})/\sqrt{2}$
CH ipb		$S_{44} = (R_{57}-R_{56})/\sqrt{2}$
CH ipb		$S_{45} = (R_{59}-R_{58})/\sqrt{2}$
CH ipb		$S_{46} = (R_{61}-R_{60})/\sqrt{2}$
CH ipb		$S_{47} = (R_{63}-R_{62})/\sqrt{2}$
CC' ipb	β''	$S_{48} = (R_{53}-R_{52})/\sqrt{2}$
trigonal def.	q_{19}	$S_{49} = (R_{64}-R_{65}+R_{66}-R_{67}+R_{68}-R_{69})/\sqrt{6}$
asy. def. A	q_{20}	$S_{50} = (2R_{64}-R_{65}-R_{66}+2R_{67}-R_{68}-R_{69})/\sqrt{12}$
asy. def. B	q_{21}	$S_{51} = (R_{65}-R_{66}+R_{68}-R_{69})/2$
CH opb	γ	$S_{52} = R_{79}$
CH opb		$S_{53} = R_{80}$
CH opb		$S_{54} = R_{81}$
CH opb		$S_{55} = R_{82}$
CH opb		$S_{56} = R_{83}$
CC' opb	γ''	$S_{57} = R_{78}$
puckering	q_{28}	$S_{58} = (R_{93}-R_{94}+R_{95}-R_{96}+R_{97}-R_{98})/\sqrt{6}$
asy. tor. A	q_{29}	$S_{59} = (-R_{93}+R_{95}-R_{96}+R_{98})/2$
asy. tor. B	q_{30}	$S_{60} = (-R_{93}+2R_{94}-R_{95}-R_{96}+2R_{97}-R_{98})/\sqrt{12}$

TABLE 3 (continued)

	Notation	Amide Group
N–H str	t	$S_{61} = R_{13}$
N–C' str	R'	$S_{62} = R_{14}$
C'–O str	S	$S_{63} = R_{15}$
NH ipb	θ	$S_{64} = (R_{47} - R_{46})/\sqrt{2}$
<C'NC def.	δ	$S_{65} = (2R_{48} - R_{47} - R_{46})/\sqrt{6}$
C'O ipb	θ'	$S_{66} = (R_{50} - R_{49})/\sqrt{2}$
<NC'C def.	δ'	$S_{67} = (2R_{51} - R_{50} - R_{49})/\sqrt{6}$
NH opb	μ	$S_{68} = R_{76}$
C'O opb	μ'	$S_{69} = R_{77}$
C–N tor.	τ_1	$S_{70} = R_{90}$
N–C' tor.	τ_2	$S_{71} = R_{91}$
C'–C tor.	τ_3	$S_{72} = R_{92}$

Figure 2. Definition of some of the non-redundant local symmetry
coordinates.
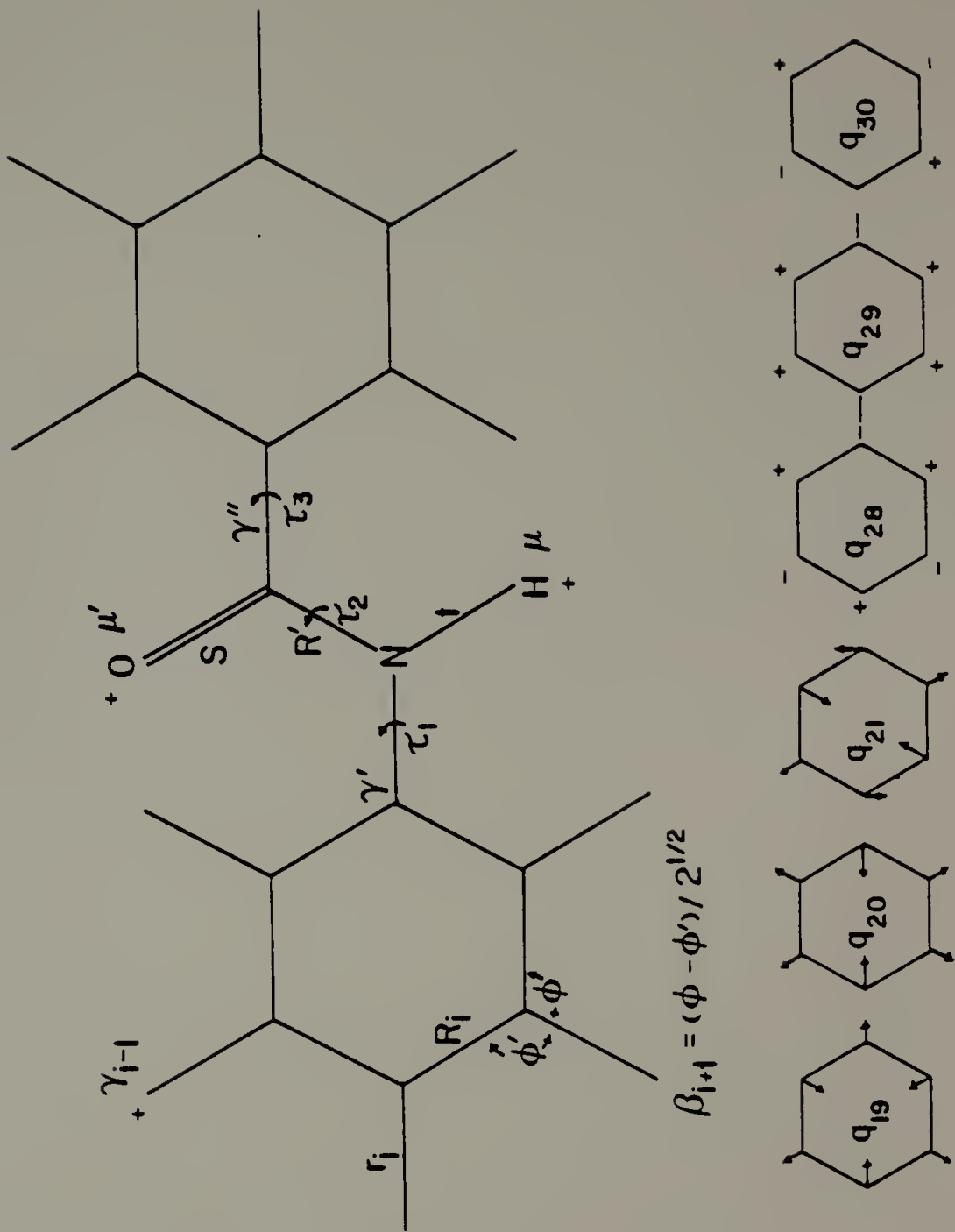
Figure 2.

TABLE 4

Force Constants for Benzanilide

Force Constant	Value	Force Constant	Value
(a) phenyl group			
$K(r)$	5.104	$F(r_2 q_{21})$	-0.08574
$K(r')$	4.043	$F(r_3 q_{21})$	0.08574
$K(r'')$	4.409	$F(R)^o$	0.633
$K(R)$	6.500	$F(R)^m$	-0.442
$H(\beta)$	0.512	$F(R)^p$	0.440
$H(\beta')$	0.8375	$F(R_1 \beta_1)$	0.167
$H(\beta'')$	0.8375	$F(R_1 \beta_3)$	-0.010
$H(q_{19})$	1.236	$F(R_1 \beta_4)$	0.019
$H(q_{20})$	1.236	$F(R_1 q_{20})$	0.134
$H(q_{21})$	1.236	$F(R_2 q_{20})$	-0.268
$H(\gamma)$	0.5852	$F(R_3 q_{20})$	-0.067
$H(\gamma')$	0.6581	$F(R_1 q_{21})$	0.2321
$H(\gamma'')$	0.6581	$F(R_3 q_{21})$	-0.2321
$H(q_{28})$	0.3763	$F(\beta)^o$	0.009
$H(q_{29})$	0.3156	$F(\beta)^m$	0.010
$H(q_{30})$	0.3156	$F(\beta)^p$	-0.001
$F(r)^o$	0.016	$F(\beta_2 q_{20})$	-0.067
$F(r)^m$	0.005	$F(\beta_1 q_{21})$	0.07736
$F(r)^p$	0.001	$F(\beta_2 q_{21})$	-0.03863
$F(r_1 R_1)$	0.079	$F(\gamma)^o$	-0.092
$F(r_1 R_2)$	-0.002	$F(\gamma)^m$	-0.0004
$F(r_1 R_3)$	-0.022	$F(\gamma)^p$	-0.0235
$F(r_1 \beta_2)$	0.005	$F(\gamma_1 q_{28})$	-0.1681
$F(r_1 \beta_3)$	-0.007	$F(\gamma_2 q_{28})$	0.1681

TABLE 4 (continued)

Force Constant	Value	Force Constant	Value
(a) phenyl group (cont)			
$F(r_1 q_{19})$	−0.105	$F(\gamma_1 q_{29})$	0.1700
$F(r_2 q_{19})$	0.105	$F(\gamma_2 q_{29})$	−0.0850
$F(r_1 q_{20})$	−0.099	$F(\gamma_2 q_{30})$	−0.1472
$F(r_2 q_{20})$	0.0495	$F(\gamma_3 q_{30})$	0.1472
$F(r' R_1)$	0.300	$F(R_1 \beta')$	0.220
$F(r'' R_1)$	0.2506	$F(R_1 \beta'')$	0.220
(b) amide group			
$K(t)$	6.168	$F(R' \theta')$	−0.1414
$K(R')$	6.415	$F(R' \delta)$	0.1249
$K(S)$	9.582	$F(R' \delta')$	0.1633
$H(\theta)$	0.6205	$F(S \delta')$	−0.4899
$H(\delta)$	0.6625	$F(R'' \theta')$	0.1414
$H(\theta')$	1.246	$F(r'' \delta')$	0.1633
$H(\delta')$	1.3487	$F(r' \theta)$	−0.2079
$H(\mu)$	0.129	$F(r' \delta')$	0.1249
$H(\mu')$	0.587	$F(\theta \theta')$	−0.1255
$H(\tau_1)$	0.010	$F(\delta \delta')$	−0.0248
$H(\tau_2)$	0.680	$F(\theta' \delta)$	0.0725
$H(\tau_3)$	0.010	$F(\theta \delta')$	0.0430
$F(\gamma' R')$	0.680	$F(\theta \delta)$	0.0231
$F(R' S)$	0.010	$F(\mu \mu')$	0.0100
$F(r'' R')$	0.300	$F(\mu' \tau_2)$	0.0110
$F(r'' S)$	0.500	$F(\mu \tau_2)$	−0.1677
$F(R' \theta)$	0.2076		

Figure 3. Infrared spectra of benzanilide. Resolution 2 cm^{-1};
500 scans.
    (a) 50-450 cm^{-1} region, far-infrared data;
    (b) 500-1800 cm^{-1} region;
    (c) 2900-3400 cm^{-1} region.

(a)

WAVENUMBERS

Figure 3(a)

34

(b)

(c)
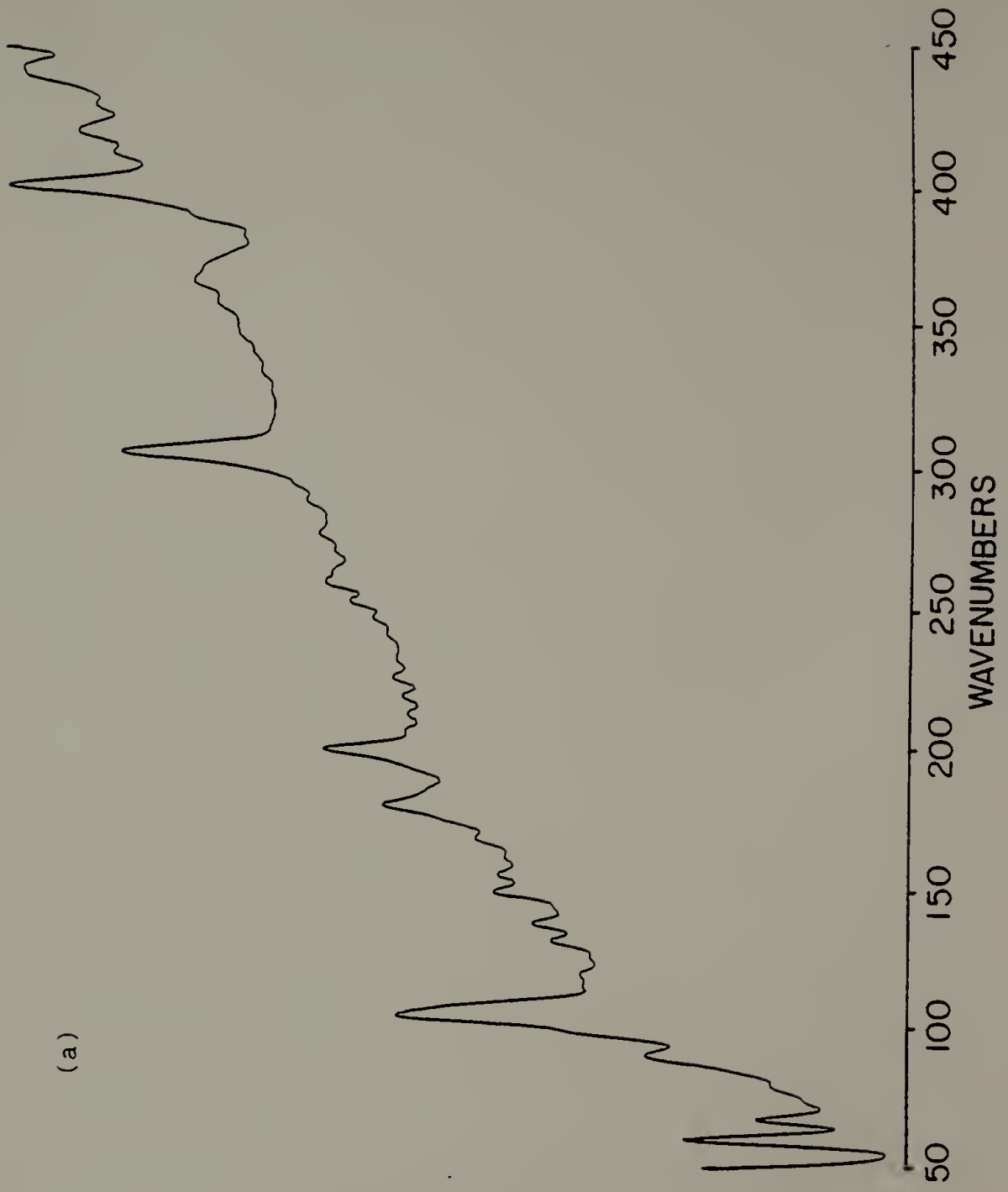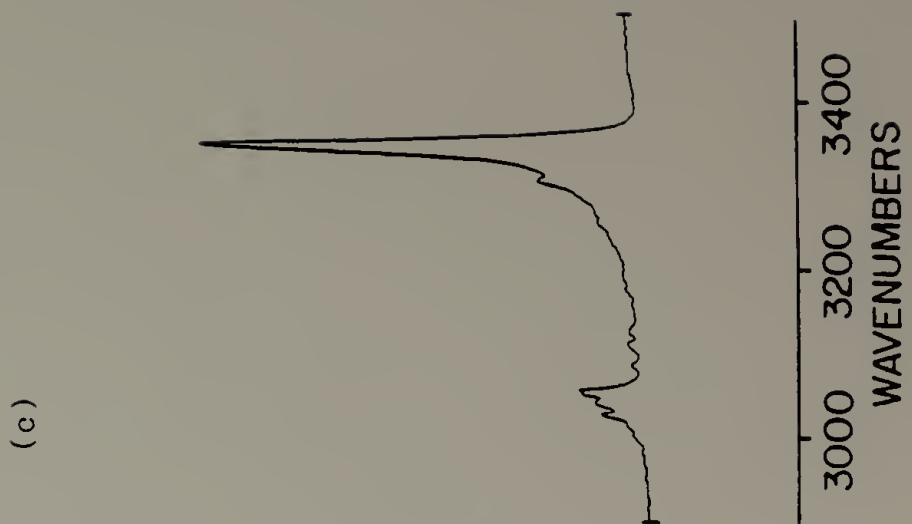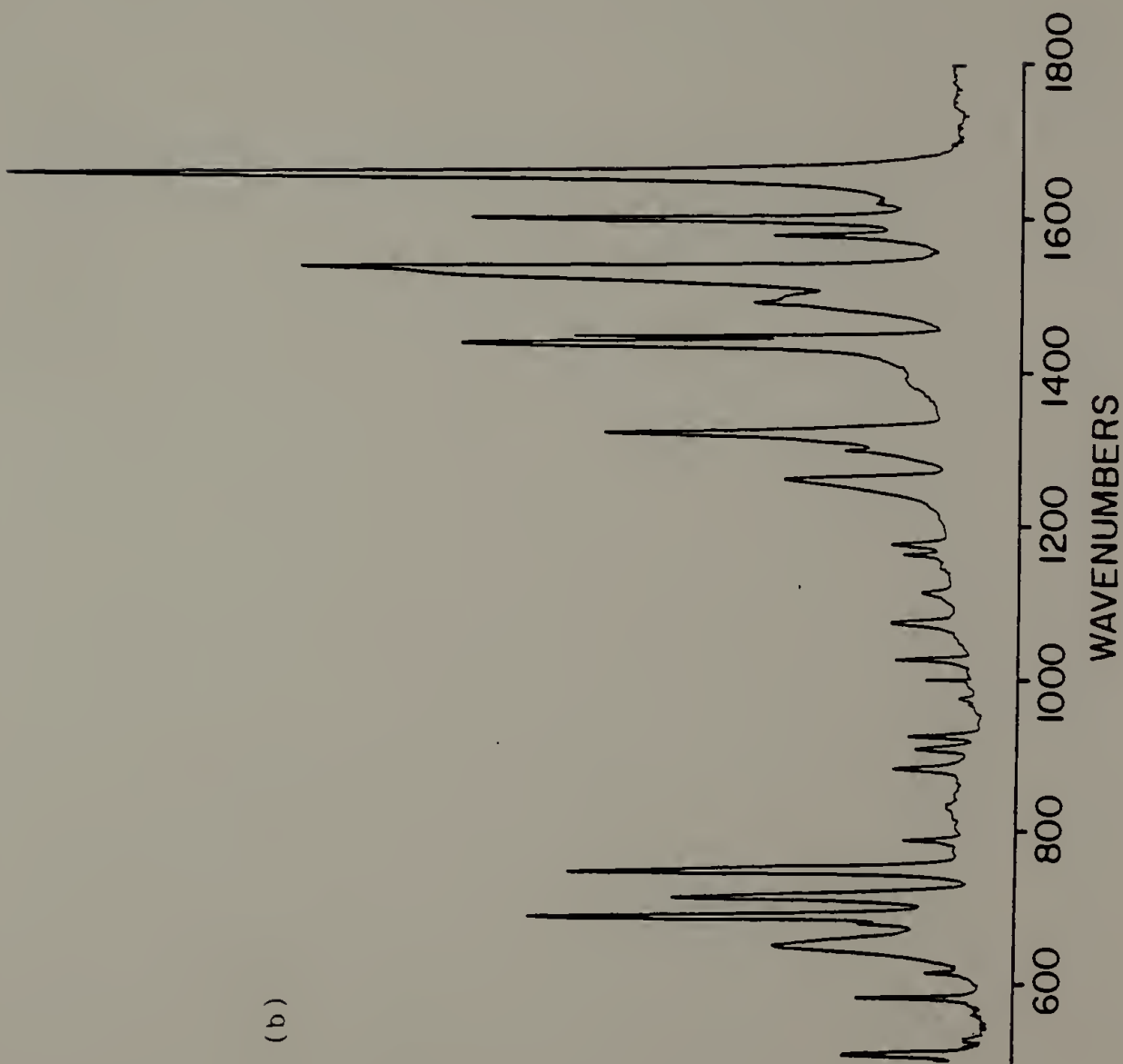
Figure 3(b) & (c)

Figure 4. Raman spectra of benzanilide. Incident excitation radiation wavelength is 514.5 nm; 2 cm-1 bandpass at 500 nm. (a) 0-1800 cm^{-1} region; (b) 2900-3400 cm^{-1} region.

WAVENUMBERS
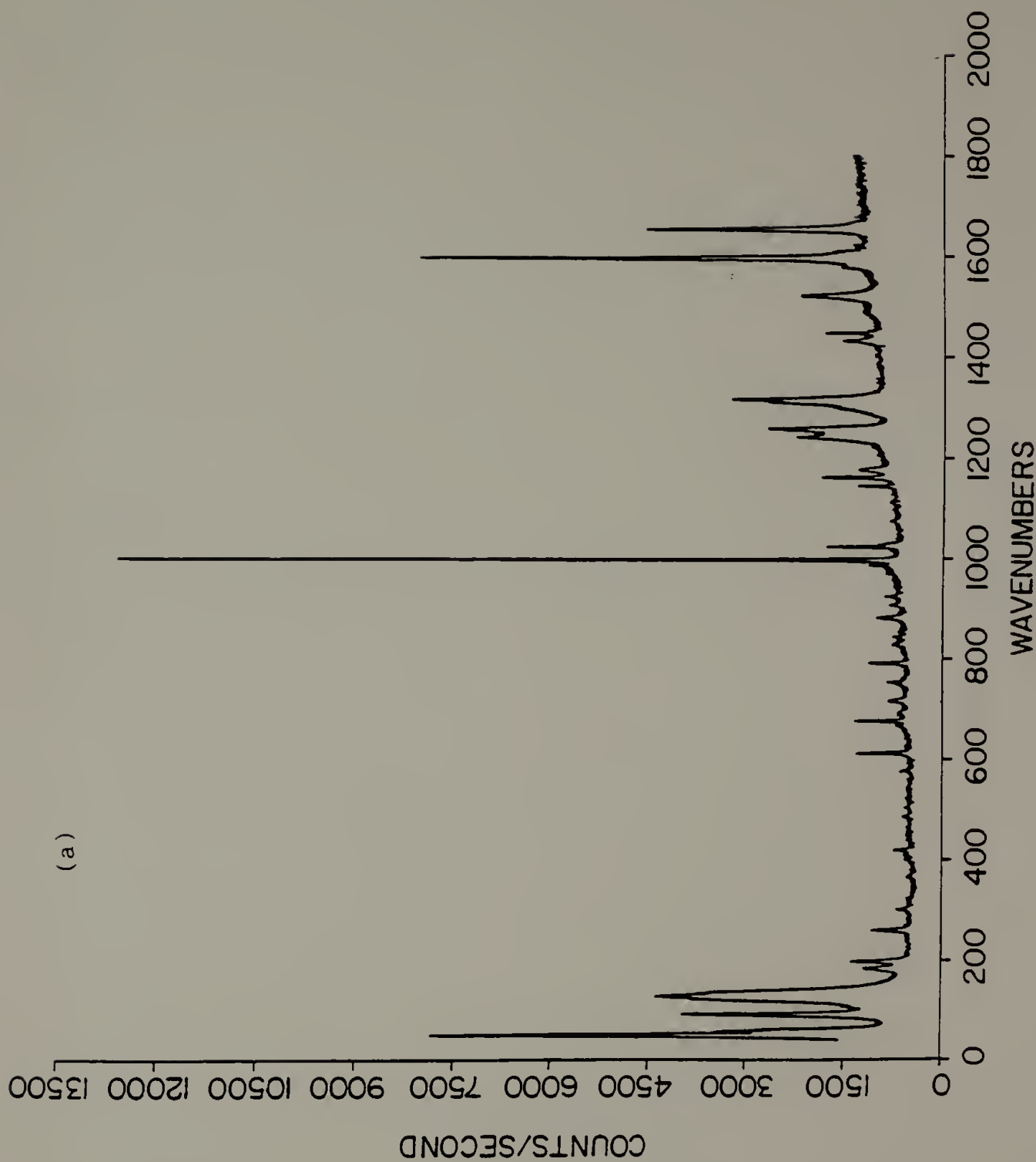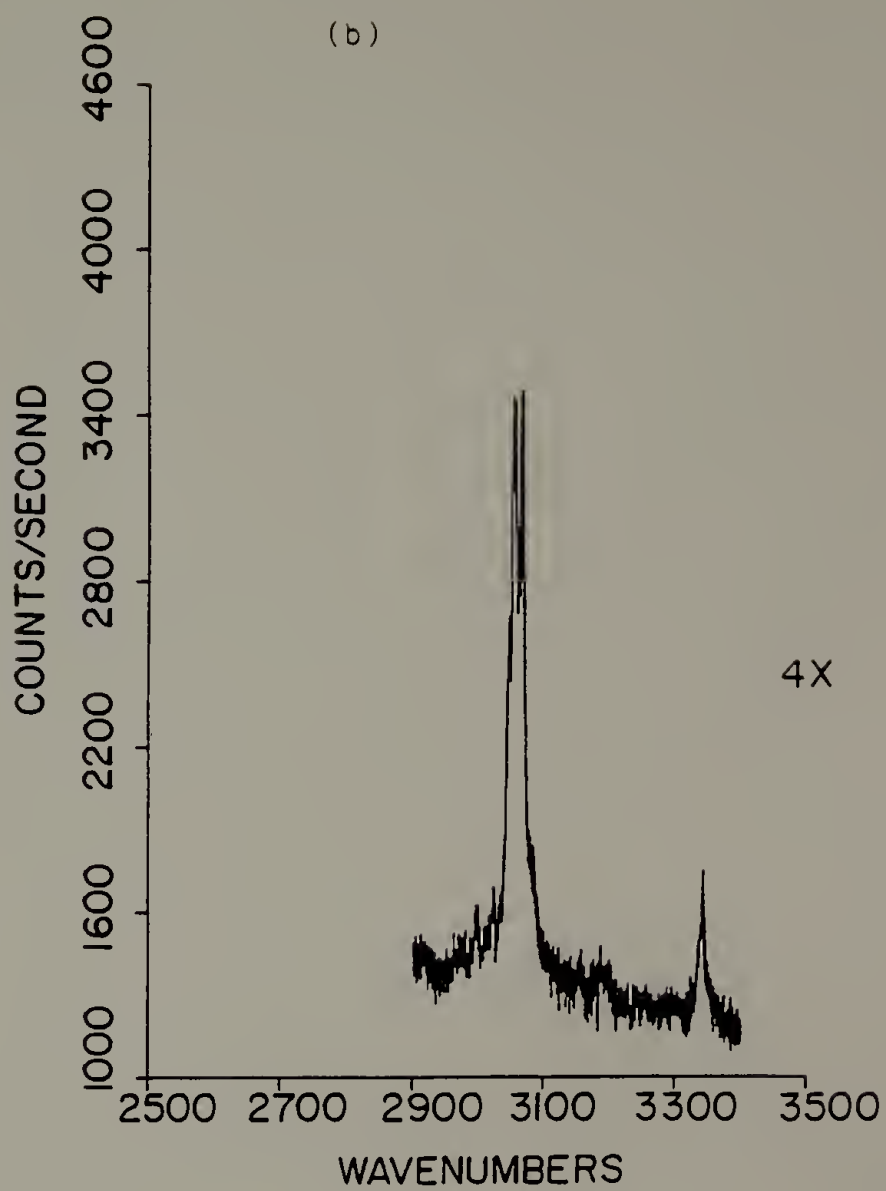
Figure 4.

Figure 4.

Figure 5. Raman spectra of benzanilide in EtOH solution. Concentration
is 10% by weight. Incident excitation radiation wavelength is 514.5 nm;
2 cm^{-1} bandpass at 500 nm.
(a) 0-1700 cm^{-1} region, parallel polarized scattering;
(b) 3000-3600 cm^{-1} region, parallel polarized scattering;
(c) 0-1700 cm^{-1} region, perpendicular polarized scattering;
(d) 3000-3600 cm^{-1} region, perpendicular polarized scattering.

WAVENUMBERS

Figure 5.

(a)

Figure 5.

WAVENUMBERS

Figure 5.

42
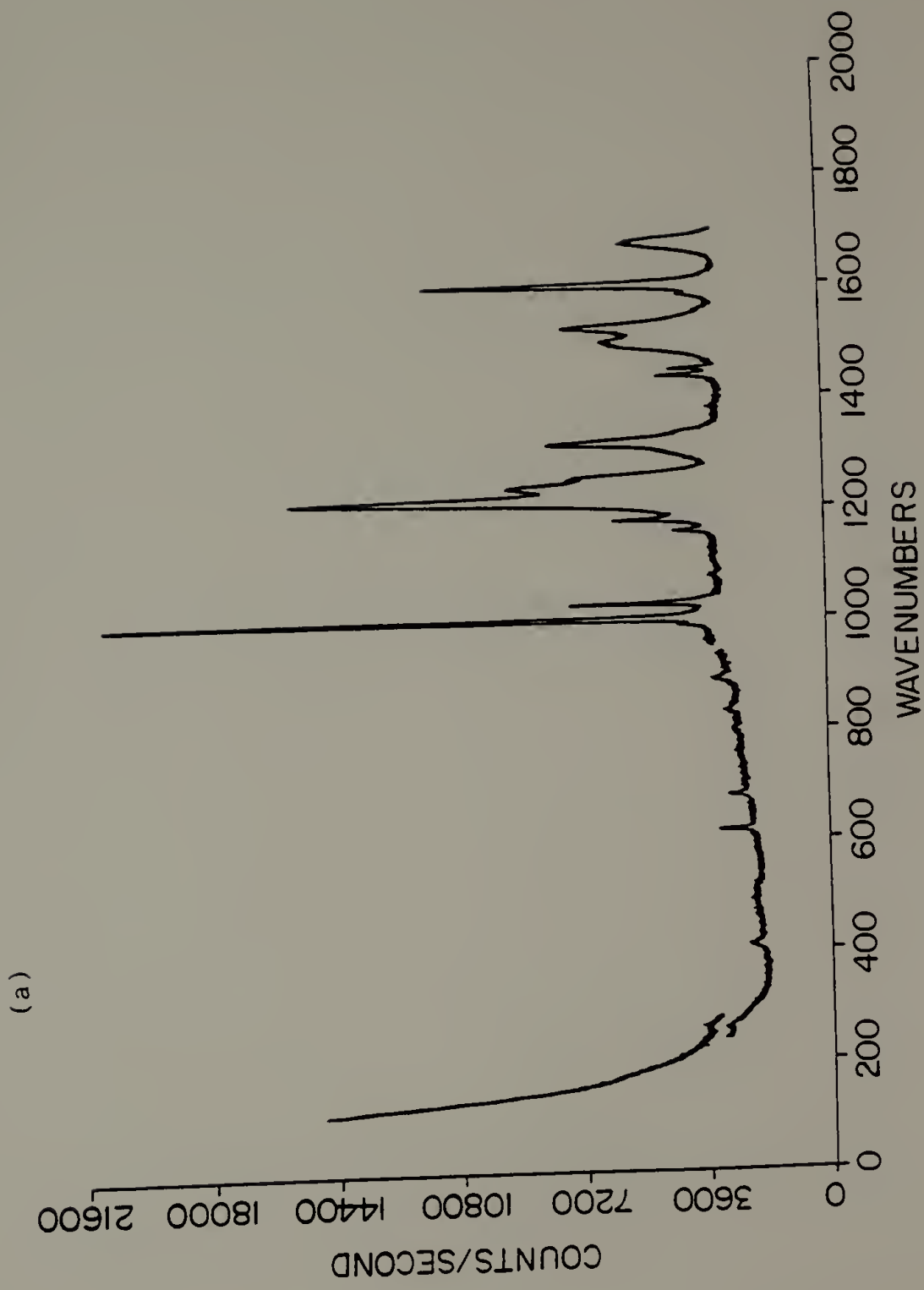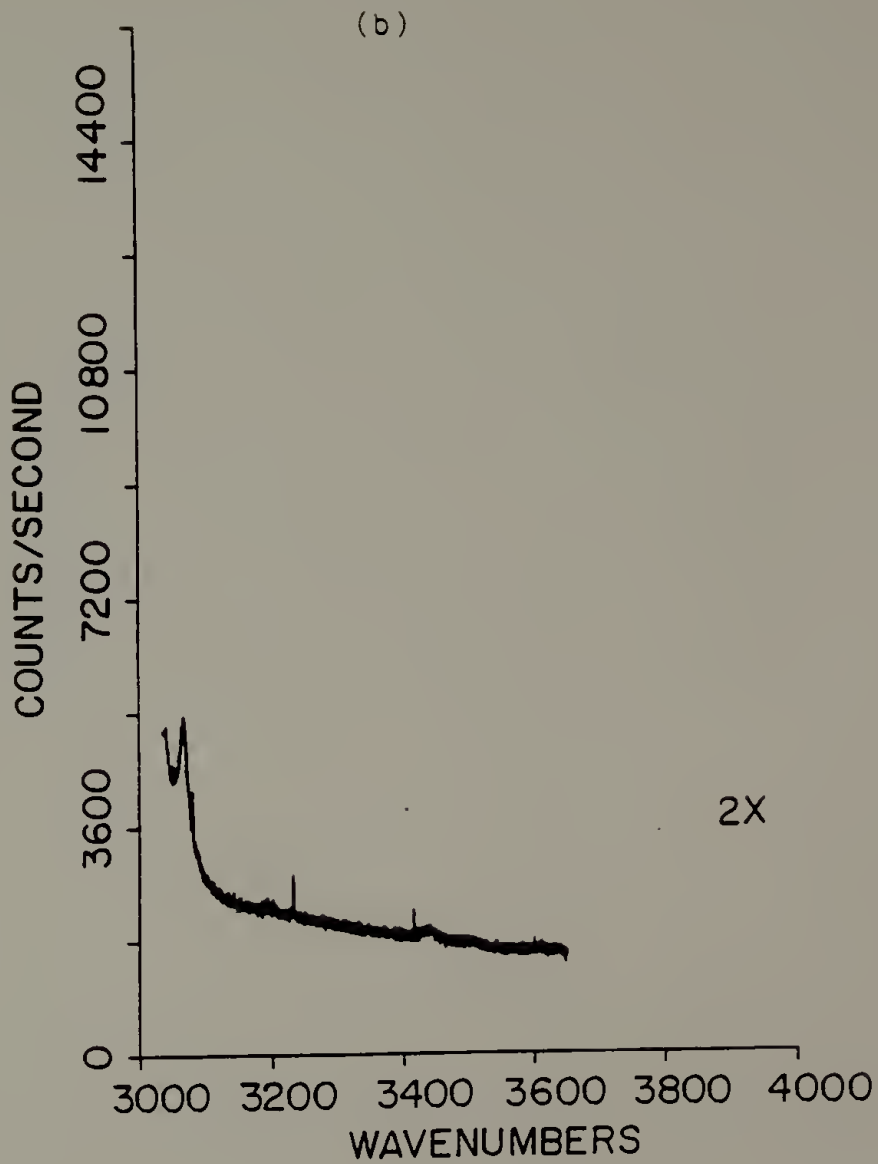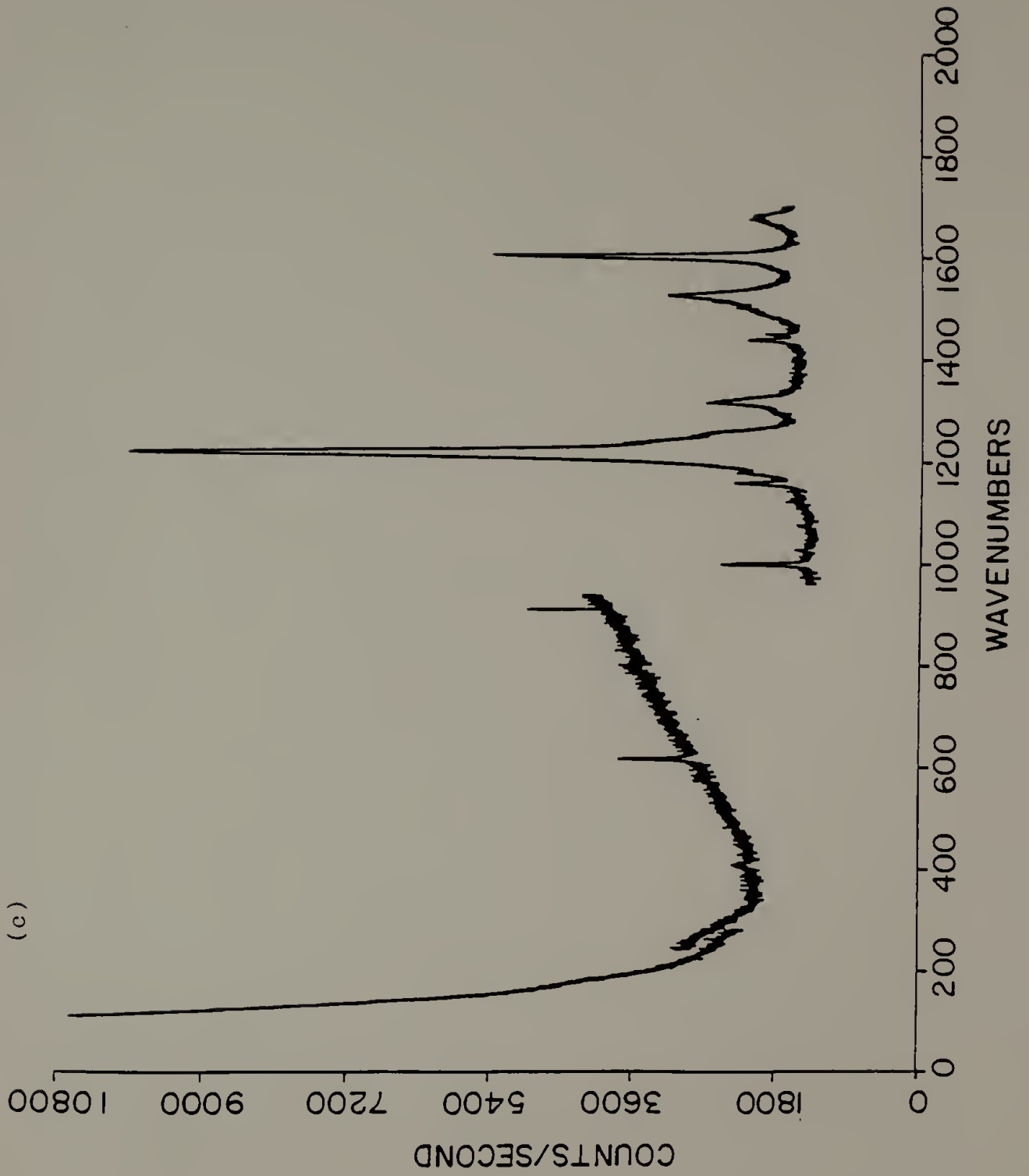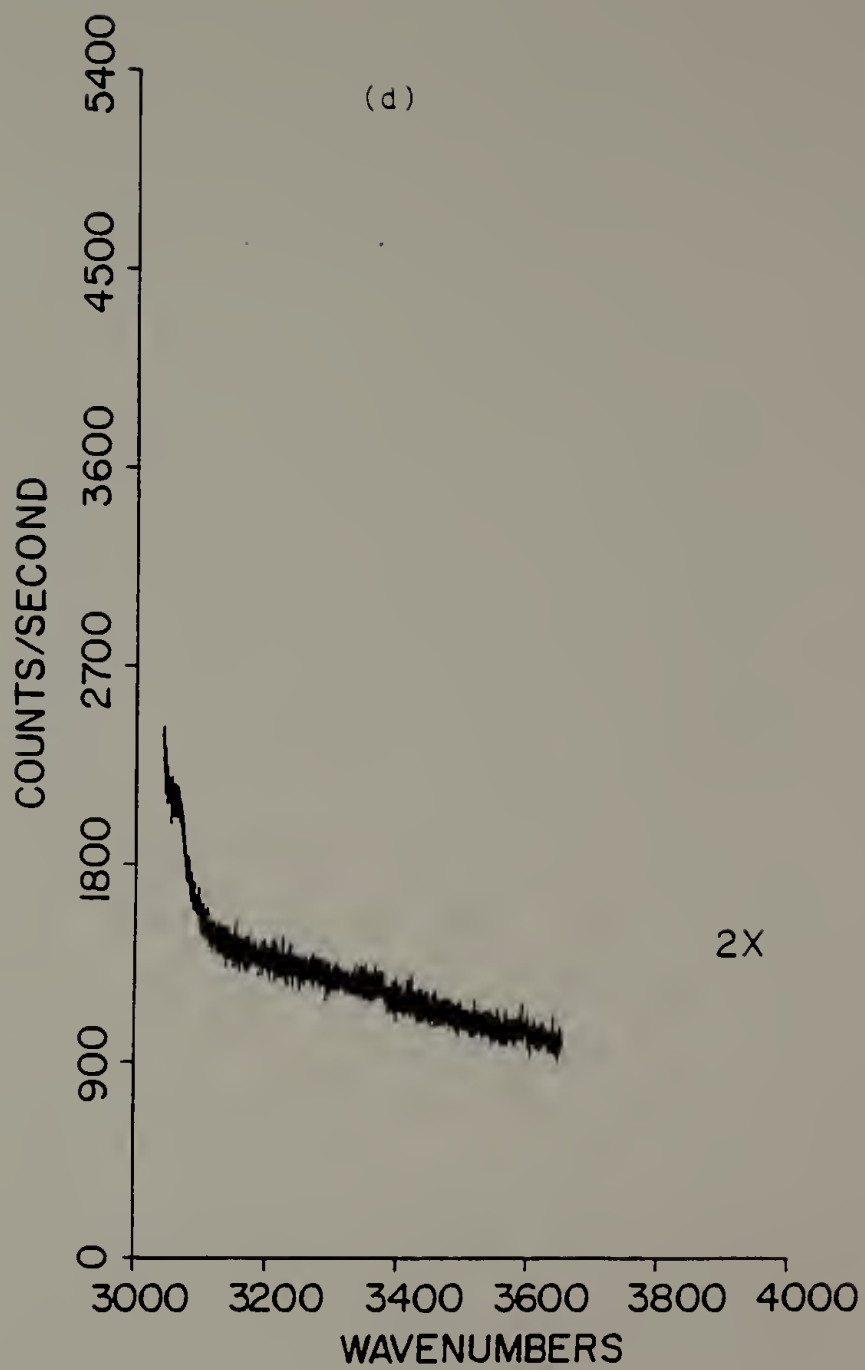
Figure 5.

Figure 6. Vibrational difiference spectra of deuterated benzanilide;
Contributions·of the protonated species are digitally subtracted.
2 cm^{-1} bandpass at 500 nm. (b) Infrared spectrum, 2 cm^{-1} resolution.
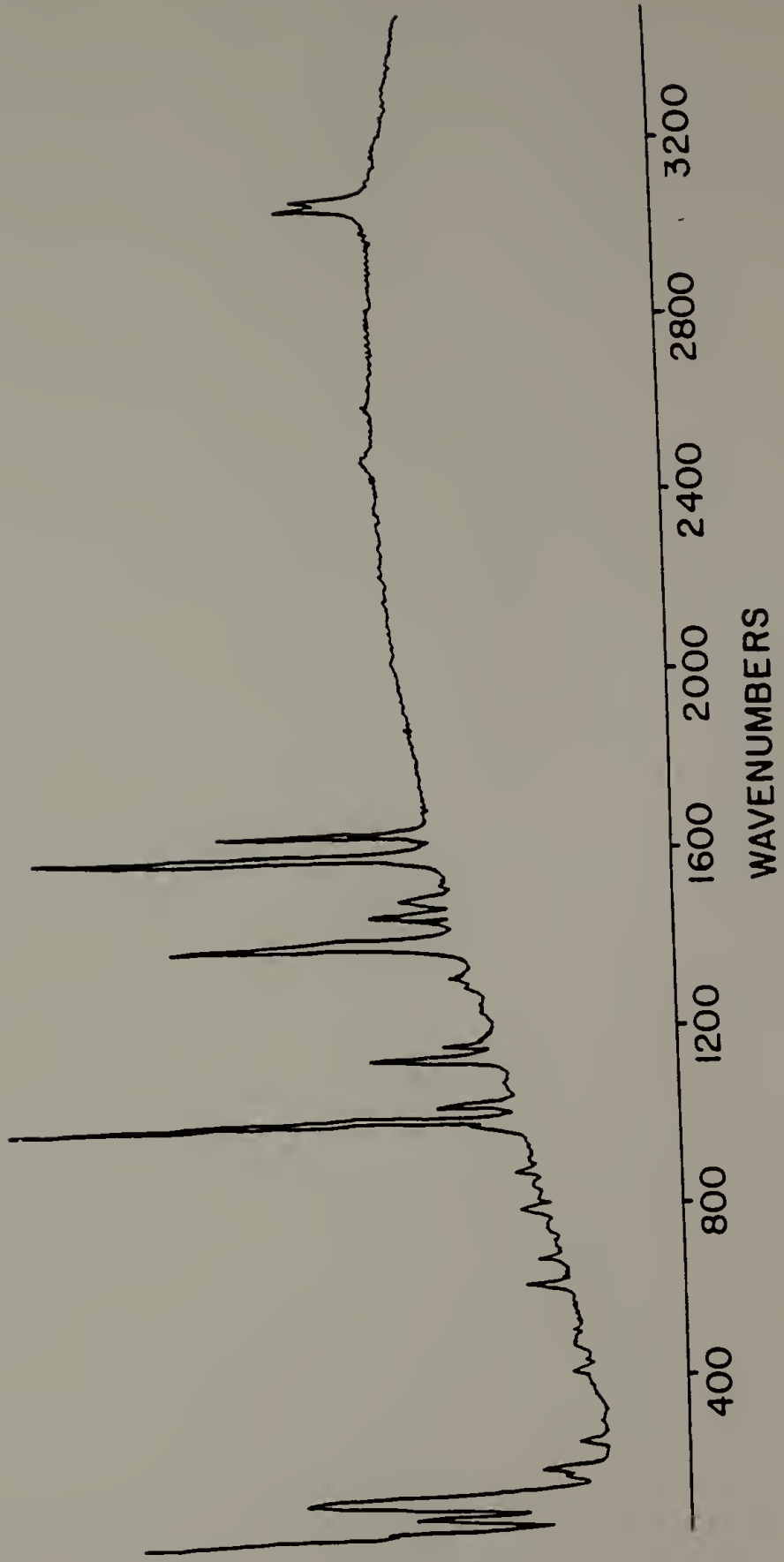
Figure 6.

(b)
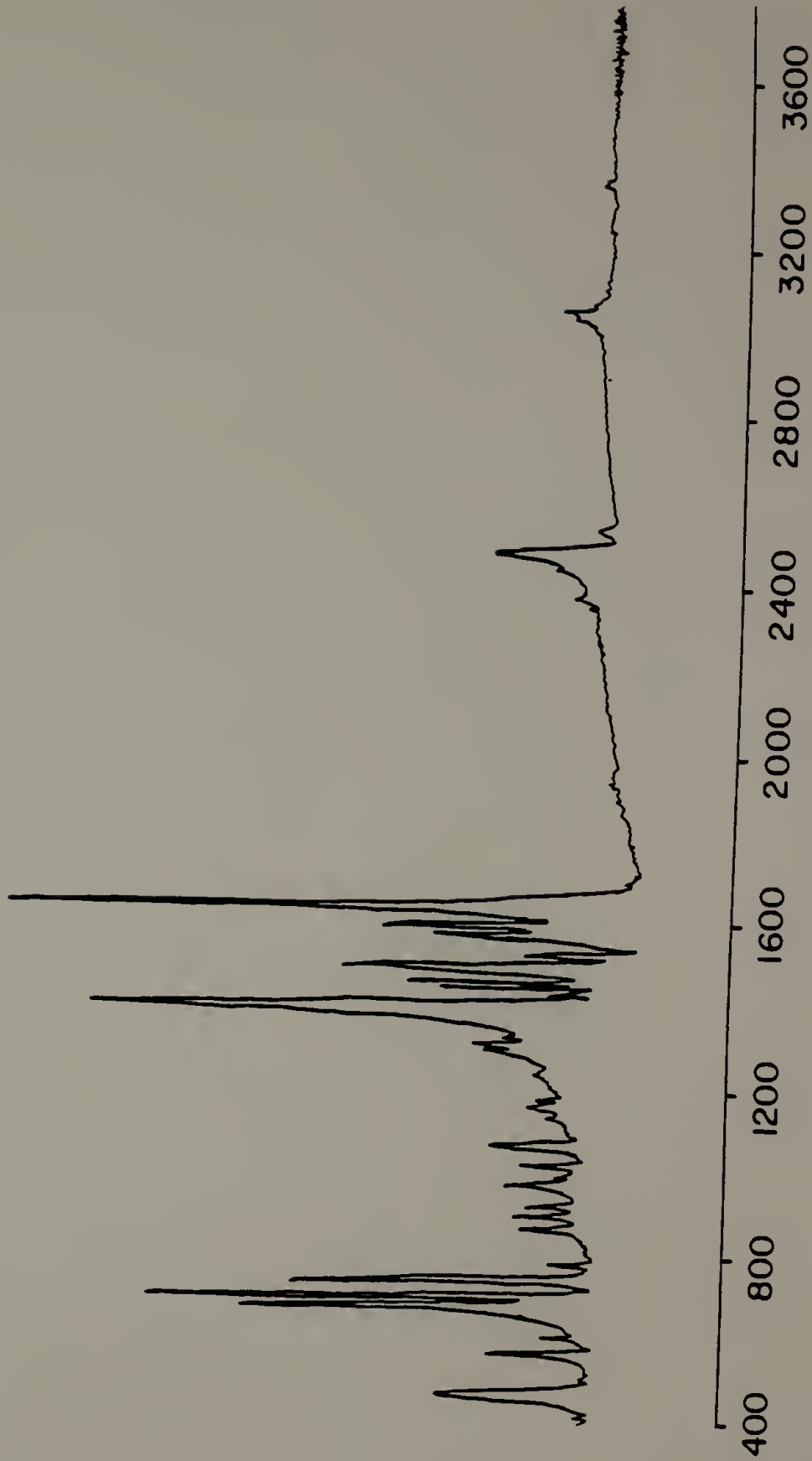
WAVENUMBERS

Figure 6.

46

II.4   RESULTS AND DISCUSSION

The benzanilide samples we obtained are comprised of entirely crystalline units. However, the crystallites are small, making polarized infrared spectra impossible to obtain. The observed (both infrared and Raman) and calculated frequencies of both hydrogenated and deuterated benzanilide are tabulated in Table 5 along with the major contributions to the potential energy distribution (PED) of each mode. The assignments of the calculated bands involving amide group motion are greatly aided by the availability of the deuterated species, -COND-. Furthermore, our results were strongly guided by the experimental and theoretical studies associated with monosubstituted benzenes [92]. This was done under the assumption that most vibrational bands of ring vibrations in the substituted benzene would not be significantly affected by the different types of substituents. As expected, the most difficult regions to assign are some of the skeletal vibrations with considerable mixing of coordinates that exist in the low frequency region.

Amide group frequencies are usually easy to distinguish from others when NH is exchanged to ND. The strong band at 3345 cm^{-1} in the infrared spectrum is assigned to a mode involving mostly NH stretching motion. This band shifts down to 2475 cm^{-1} after deuteration, which is slightly higher than the calculated value.

A strong band at 1656 cm^{-1} in both infrared and Raman spectra is assigned to the Amide I mode which is dominated by C=O stretching

TABLE 5

Observed and Calculated Frequencies (in cm-1) of Benzannilide

(a) -NHCO-

IR	Raman	Calculated	Potential Energy Distribution[+]
3345	3342	3344	17(100)
	3070	3070	1B(94)
		3070	1A(94)
3050	3056	3059	1B(97)
		3059	1A(97)
	3049	3049	1B(100)
		3049	1A(100)
3041		3040	1B(100)
		3040	1A(100)
3027		3032	1B(75) 1A(26)
		3032	1A(75) 1B(26)
1656	1658	1657	19(62) 18(18) 22(·13) 28(11) 15(5)
1600	1600	1605	2B(25) 19(7) 25(13) 14(10) 2B(31) 3B(7)
		1593	2A(48) 3A(10) 2B(32) 3B(7)
	1583	1587	2A(73) 3A(21) 5A(6)
	1579	1577	19(7) 2B(71) 3B(22) 6B(6)
1536	1524	1537	2A(12) 3A(6) 18(18) 23(6) 25(27) 14(7)
			2B(20) 3B(9)
1502		1499	2A(31) 3A(52) 2B(5) 3B(9)
1493	1495	1489	2A(6) 3A(10) 25(10) 2B(24) 3B(49)
1449	1453	1449	2A(23) 3A(40) 2B(11) 3B(20)
1440	1437	1442	2A(9) 3A(17) 2B(23) 3B(43)
1329		1329	2A(29) 3A(44) 25(13) 14(8) 3B(18)
	1317	1315	3A(22) 2B(6) 3B(69)
1301	1300	1304	2A(67) 3A(40) 25(11) 3B(6)
		1288	2B(139) 3B(27)
1262	1262	1259	12(8) 2A(79) 3A(17) 25(17)
	1244	1237	12(27) 2A(26) 3A(10) 14(16) 2B(15) 3B(7)
1180	1179	1179	2B(8) 3B(82)

TABLE 5 (continued)

IR	Raman	Calculated	Potential Energy Distribution[+]
		1179	2A(9) 2B(80)
1166	1164	1162	3A(10) 2B(21) 3B(63)
		1162	2A(21) 3A(63) 3B(10)
1116	1113	1096	18(16) 19(7) 25(6) 2B(22) 3B(9) 4B(13)
1076	1079	1071	2A(47) 3A(33)
		1068	2B(43) 3B(31)
1028	1027	1019	2A(45) 3A(15) 4A(16) 2B(4)
		1016	2A(6) 2B(40) 3B(13) 4B(24)
1001	999	985	2A(36) 4A(37) 2B(9) 4B(10)
	991	984	2A(10) 4A(8) 2B(40) 4B(32)
979		982	7A(85) 8A(20) 7B(50) 8B(12)
		982	7A(51) 8A(11) 7B(86) 8B(19)
	968	963	7A(6) 7B(120) 10B(11)
		963	7A(120) 10A(11) 7B(6)
928	922	928	7A(56) 8A(12) 9A(7) 13(11) 16(7) 7B(37) 8B(8) 9B(5)
909	909	913	7A(44) 8A(5) 16(6) 7B(73) 8B(8) 9B(6)
886	884	870	7A(18) 18(11) 19(8) 22(11) 23(10) 24(15)
	846	838	7A(22) 17B(91)
	830	838	7A(91) 7B(22)
		825	7A(6) 8A(6) 13(5) 8A(8) 23(7) 27(9) 16(12) 7B(16) 8B(18)
792	797	800	11(13) 2A(22) 4A(11) 5A(10) 7A(8) 13(8) 8A(13)
750	757	775	2A(22) 7A(17) 13(12) 8A(22) 21(17) 16(16) 7B(22) 8B(27)
716		699	7A(35) 21(6) 7B(46) 8B(44)
		695	7A(68) 8A(59) 8B(16)
691	699	691	7A(8) 21(26) 5B(7) 7B(58)
	683	674	5A(6) 7A(5) 8A(16) 21(7) 23(9) 14(5) 28(8) 5B(38) 7B(5) 8B(8)
652		638	7A(17) 8A(51) 10(5) 21(6) 27(11) 7B(16) 8B(47)
		625	6B(79)
616	619	620	6A(82)
584	583	576	5A(40) 22(15) 23(7) 8B(8)
509	485	487	5A(13) 7A(5) 13(13) 9A(24) 5B(11) 16(13) 7B(5) 9B(28)
		430	5A(5) 7A(7) 13(26) 9A(74) 21(8) 23(5) 9B(5)

TABLE 5 (continued)

IR	Raman	Calculated	Potential Energy Distribution[+]
	405	403	16(9) 7B(17) 9B(33) 10B(83)
		401	7A(27) 10A(136)
371	372	399	12(5) 16(12) 7B(17) 9B(41) 10B(74)
307	305	317	12(26) 9A(10) 20(7) 23(27) 24(11)
261	263	263	11(7) 12(10) 5A(6) 20(12) 14(11) 15(19) 5B(8)
202	199	222	7A(7) 13(7) 9A(22) 20(60) 24(5) 27(35)
182	186	177	13(8) 9A(11) 21(9) 22(6) 13(21) 16(10) 7B(7) 9B(19)
	130	150	12(13) 20(5) 22(9) 24(14) 27(8) 15(14) 16(13) 9B(8)
106	93	82	13(10) 9A(6) 20(12) 26(32) 27(25) 28(9) 16(12)
61	59	66	12(15) 22(17) 24(36) 15(8) 16(13)
	51	51	13(15) 20(11) 26(12) 27(34) 28(42)
	36	32	13(5) 26(48) 27(5) 28(41)

(b) −NDCO−

IR	Raman	Calculated	Potential Energy Distribution[+]
	3070	3070	1A(11) 1B(88)
		3070	1A(88) 1B(11)
		3059	1A(89) 1B(10)
		3059	1A(10) 1B(89)
3050	3050	3049	1A(15) 1B(85)
		3049	1A(85) 1B(15)
		3040	1A(97)
3035		3032	1A(92) 1B(9)
		3032	1A(92) 1B(9)
2475		2462	12(97)
1647	1646	1654	18(19) 19(61) 22(12) 2B(13) 15(5)
	1596	1596	2A(9) 19(6) 14(10) 20(60) 3B(15) 5B(8)
1589		1593	11(5) 2A(67) 3A(15) 5A(7) 28(13)
		1585	2A(78) 3A(22) 6A(8)
1579		1577	19(8) 2B(70) 3B(22) 68(6)
1502		1511	11(5) 2A(12) 3A(14) 18(9) 14(9) 2B(23) 3B(26)
1490	1495	1498	2A(24) 3A(41) 2B(12) 3B(20)

TABLE 5 (continued)

IR	Raman	Calculated	Potential Energy Distribution[+]
1465	1463	1460	2A(9) 3A(16) 18(10) 2B(13) 3B(28)
1449	1448	1460	2A(24) 3A(42) 2B(10) 3B(18)
1439		1437	2A(5) 3A(11) 18(14) 2B(20) 3B(38)
1400	1400		
1332	1330	1319	2A(6) 3A(59) 38(28)
1317	1317	1315	3A(31) 2B(5) 3B(59)
1300	1300	1287	2B(141) 3B(26)
		1285	2A(146) 3A(26)
1240		1236	11(32) 2A(14) 3A(12) 4A(10) 14(12) 2B(13) 3B(6)
118 0		1180	3A(28) 2B(5) 3B(56)
		1179	2A(6) 3A(55) 3B(28)
1165	1165	1163	2A(6) 3A(18) 2B(18) 3B(53)
		1162	2A(18) 3A(55) 2B(6) 3B(19)
1138	1138	1137	2A(9) 4A(5) 18(7) 25(12) 14(12) 2B(18) 3B(9) 4B(13)
1077		1071	2A(34) 3A(24) 2B(14) 3B(10)
		1069	2A(14) 3A(9) 2B(36) 3B(24)
1029	1027	1019	2A(30) 3A(10) 4A(10) 2B(22) 3B(75)
		1017	2A(21) 3A(7) 4A(10) 2B(28) 3B(9) 4B(13)
1002	1000	985	2A(6) 4A(7) 2B(42)
		985	2A(41) 4A(38) 2B(7) 4B(6)
		982	7A(94) 8A(22) 7B(41) 5B(10)
		982	7A(40) 8A(9) 7B(95) 8B(21)
		963	7A(110) 10A(10) 7B(16)
		963	7A(16) 7B(110) 10B(10)
980	985	959	7A(7) 18(5) 23(7) 25(59) 2B(13)
927		925	7A(41) 13(7) 8A(8) 16(10) 7B(57) 8B(11) 9B(7)
		910	7A(60) 8A(6) 7B(54) 8B(5)
875		857	7A(12) 18(11) 19(8) 22(12) 23(8) 24(14)
		838	7A(86) 7B(27)
		820	7A(6) 13(5) 8A(9) 18(5) 23(7) 27(10) 16(13) 7B(16) 8B(20)
790	794	785	11(14) 2A(23) 4A(11) 5A(14) 7A(5) 8A(7)

TABLE 5 (continued)

IR	Raman	Calculated	Potential Energy Distribution[+]
750		773	7A(24) 13(17) 8A(33) 21(15) 16(14) 7B(19) 8B(23)
711		698	7A(31) 7B(65) 8B(42)
		695	7A(64) 8A(55) 7B(9) 8B(23)
690		689	7A(9) 20(5) 21(32) 5B(12) 7B(35)
679	680	672	5A(5) 7A(5) 8A(12) 21(11) 23(8) 2B(7) 5B(35) 7B(7) 8B(13)
		629	7A(19) 8A(49) 20(5) 27(13) 6B(7) 7B(12) 8B(36)
		624	6B(72) 8B(7)
616	617	620	6A(80) 6B(6)
577		567	5A(38) 22(16) 23(7) 2B(6) 8B(7)
480		486	5A(13) 7A(5) 13(13) 9A(24) 5B(10) 16(14) 7B(5) 9B(29)
	422	422	5A(6) 7A(7) 13(21) 9A(91) 20(5) 23(6) 5B(5)
		403	16(5) 7B(22) 9B(18) 10B(117)
401		401	7A(28) 10A(157)
		398	12(7) 21(5) 22(5) 5B(5) 16(16) 7B(13) 9B(58) 10B(42)
	307	312	12(21) 9A(15) 23(28) 24(12) 14(5) 15(5) 5B(5)
	262	258	11(8) 12(10) 5A(7) 9A(5) 18(6) 14(11) 15(15) 5B(8) 9B(7)
	200	184	12(9) 7A(6) 13(12) 9A(15) 20(64) 27(21)
	185	176	13(5) 9A(8) 21(10) 22(7) 15(23) 16(10) 7B(7) 9B(19)
	135	147	12(9) 20(14) 22(8) 24(11) 27(12) 15(11) 16(15) 7B(5) 9B(8)
	92	78	13(8) 9A(5) 20(20) 26(33) 27(29) 28(10) 16(9)
	62	65	12(15) 22(16) 24(36) 27(5) 15(7) 16(14)
	50	51	13(15) 20(12) 26(12) 27(34) 28(41)
		32	13(5) 26(47) 27(5) 28(41) 16(5)

TABLE 5 (continued)

[+]Number of the coordinate is followed by the potential energy in percent. Combinations less than 5 percent are not included. The coordinate definitions in the potential energy distributions are:

1. ring C-H stretching
2. ring C-C stretching
3. ring C-H in-plane bending
4. ring trigonal deformation
5. ring asymmetric deformation - type 1
6. ring asymmetric deformation -type 2
7. ring C-H out-of-plane bending
8. ring puckering
9. ring asymmetric torsion - type 1
10. ring asymmetric torsion - type 2
11. C-N stretching
12. C-N in-plane bending
13. C-N out-of-plane bending
14. C'-C stretching
15. C'-C in-plane bending
16. C'-C out-of-plane bending
17. N-H(D) stretching
18. N-C' stretching
19. C'-O stretching
20. N-H(D) out-of-plane bending
21. C'-O out-of-plane bending
22. <NC'C bending
23. C'-O in-plane bending
24. <CNC' bending
25. N-H(D) in-plane bending
26. CN torsion
27. NC' torsion
28. C'C torsion

motion, similar to that observed in the polypeptide studies. The strong

band 1536 cm^{-1} in the infrared spectrum is assigned to the Amide II

mode. The calculated value is in good agreement with the observed

frequency. Its PED shows proper contributions from NH in-plane bending,

NC(O) stretching, and C=O in-plane bending. In addition, there are

considerable contributions from C(O)C stretching, and ring CC

stretchings. After deuteration, a band of medium intensity is found at

1465 cm^{-1}. The calculated frequency of 1460 cm^{-1} is assigned to this

band based on its PED and comparison with polypeptide studies where a

similar shift in amide II frequency upon deuteration has been observed.

Upon deuteration its PED also changed substantially from before. For

instance, the ring CC stretching contribution is replace by the

contributions from the ring CH in-plane bending. Bands around 1260 cm^{-1}

of medium intensity in both infrared and Raman spectra are assigned to

Amide III. This band is generally regarded as the most sensitive

indicator of the conformational change in polypeptides. Its PED is

similar to that of Amide II except there are greater contributions from

ring in-plane deformation mode. For deuterated benzanilide, this band

is calculated to be at 959 cm^{-1}. A new band observed near 980 cm^{-1} is

therefore assigned to Amide III like vibrational mode for this

deuterated molecule.

In many synthetic polypeptides, the amide bands are perturbed by

the transition dipole coupling of the hydrogen bonded C=O groups of the

adjacent chains [91]. However, the molecules in the unit cell of

benzanilide are too far apart for such interactions to occur.

Therefore, unlike the multicomponents seen in the spectra of some polypeptide crystals, we would expect only one nearly degenerate component for amide bands in either the Raman or infrared spectra.

Since the non-redundant local symmetry coordinates are well defined, the assignments of ring vibrations can be easily accomplished by examining the PEDs in conjunction with the previous studies on toluene [92], methyl benzoate [94], and benzaldehyde [95]. In most cases, our calculated and observed frequencies showed good agreement. In the region between 1600 cm^{-1} and 1000 cm^{-1}, the observed bands in both infrared and Raman spectra are mostly due to ring CC stretching and CH in-plane bending. Bands near 1502, 1493, 1449, 1440, and 1076 cm^{-1} are due to ring CC stretching with large contributions from CH in-plane bending. This type of mixing between these two internal coordinates have been observed in both benzene and its monosubstituted derivative. Furthermore, their PEDs indicate additional mixing of vibrational motions between benzene rings. On the other hand, bands near 1329, 1180, and 1166 cm^{-1} are mostly due to ring CH in-plane bending and, finally, bands near 1028 and 1001 cm^{-1} involve ring CCC valence angle deformations, i.e. ring in-plane deformations, in addition to either ring CH in-plane bending or ring CC stretching. The out-of-plane bending vibrations are assigned in a similar manner to the in-plane ones. Again, their frequencies appear to be characteristic of monosubstituted benzene derivatives and independent of the type of substitutes. We were curious how the differences in the environment in the two rings are reflected in the calculated spectra. One of the

largest calculated differences were found for the 1600 cm^{-1} band. The observed band near 1600 cm^{-1} in both infrared and Raman spectra which is associated with ring stretching indicates that two benzene rings in benzanilide apparently have identical frequencies for this vibrational mode. This is not reflected in the calculated spectrum which shows two components at 1606 and 1594 cm^{-1}. This is believed to be directly related to the different interaction force constants between the ring and the CC(O) or CN bond stretchings. This apparently was the case for aromatic polyester as well [94]. In that case, nearly all interaction force constants between the stretching motions were set to zero in order to reduce the difference calculated. One of the main objective of this analysis has been to check the transferability of this force fields to PPTA and other model compounds. Therefore, we did not refine the force fields to reduce the difference between the calculated and experimental frequencies. But even without any refinements, this agreements between them are better than the result obtained with redundant internal coordinates. It should also be pointed out that this difference in the local environments of each ring is predicted rather well in the deuterated molecules. In this case the character of the mode also changes due to the contribution from the deuterated amide group.

II.5   <u>CONCLUSION</u>

In order to calculate the theoretical vibrational spectra of molecules possessing a high number of cyclic or branching redundancies, and to minimize the refinement of the force field needed to describe complicated molecules, the use of non-redundant symmetry coordinates is perhaps the most appropriate answer. The use of such a technique was instrumental in combining separate force fields together which had been refined earlier to observe various derivatives of benzene rings and amide groups in the analysis of benzanilide. Even though several approaches are available, we constructed a set of non-redundant symmetry coordinates by incorporating one set which most clearly described the normal vibrations of the benzene ring and another set which is commonly used to describe the amide group vibrations. Even though this approach is not easily carried out entirely by computer, and it is in fact may not be generally applicable to all molecules, in this particular case when reliable force fields are available from other means, satisfactory results were obtained for benzanilide without any need for force field refinement. In the following chapter, we have carried out similar analysis to understand the vibrational characteristics of poly(p-phenylene terephthalamide).

CHAPTER III

VIBRATIONAL ANALYSIS OF POLY(p-PHENYLENE TEREPHTHALAMIDE)

III.1   INTRODUCTION

As mentioned in the previous chapter, there have been only limited quantitative vibrational spectroscopic studies of PPTA because of the lack of understanding of its vibrational characteristics [43-45]. This is generally due to its complex structures and extremely low molecular symmetry, which makes their complicated infrared and Raman spectra difficult to analyze. So, ever after overcoming the experimental difficulties associated with working with strong acids as solvents, the high temperatures, its small fiber diameters, and etc., the theoretical vibrational analysis remains as a considerable challenge.

Similar to the vibrational analysis of benzanilide that was discussed in Chapter II, PPTA also has a considerable number of branching and cyclic redundancies and the associated problems with the redundant internal coordinates in the normal coordinate analysis. In Chapter II, we have carried out the normal coordinate analysis of benzanilide, a model compound of PPTA, by transfering the non-redundant symmetry coordinates and force constants associated with the benzene and amide group. This was done under the assumption that many of the normal vibrations of a chemical group remain relatively unperturbed by the adjacent chemical groups. The results from this calculation have

satisfactorily accounted for the observed vibrational characteristics of benzanilide. In this chapter, we have extended this technique to analyze the vibrational spectra of PPTA by transfering the non-redundant coordinates and the force fields from Chapter II.

In addition, when the bands are properly assigned and reliable force constants are available for PPTA, it is possible to calculate the theoretical mechanical properties [96-98] and to evaluate the stress-induced structural changes at the molecular level [99-101]. We have used two approaches proposed earlier [43,102-104] to calculate the maximum tensile modulus of PPTA.

In all of these studies, the analysis has been greatly aided by use of deuterated molecules. Because most of the observed vibrational bands of PPTA are unexpectedly broad, two additional model compounds of PPTA have been employed, N,N'-phenylterephthalamide and N,N'-dibenzoyl-p-phenylene diamine, to illustrate the effect of the different local environments associated with the substituted benzene rings and the amide groups within the chemical repeat unit of PPTA. These experimental results, in conjunction with the theoretical normal coordinate analysis, are presented in this chapter.

III.2   <u>EXPERIMENTAL</u>

The two model compounds for PPTA, N,N'-phenylterephthalamide,
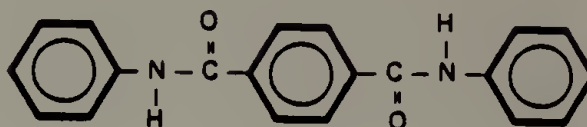
and N,N'-dibenzoyl-p-phenylene diamine,
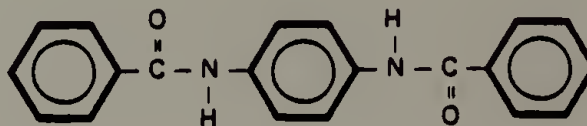
were obtained from Dr. W.W. Adams of the Air Force Materials Laboratory.
The N,N'-phenylterephthalamide was recrystallized from ethylacetoacetate
and the N,N'-dibenzoyl-p-phenylene diamine was recrystallized by
sublimation.   Potassium bromide pellets containing 1-3% of these
recrystallized samples were prepared for the infrared measurements.
Infrared spectra were taken with an International Business Machine model
98 vacuum Fourier transform infrared spectrometer.   Five hundred scans
of 2 cm^{-1} resolution spectra were signal averaged for our analysis.
Typical infrared spectra of these model compounds are shown in Figures 7
and 8.   Raman measurements were taken with a Jobin-Yvon Ramanor HG.2S
spectrometer.   In all cases, bandpass was maintained at 1 cm^{-1} at

Figure 7. Infrared spectra of N,N'-phenylterephthalamide. Resolution 2 cm^{-1}; 500 scans. (a) 700-1800 cm^{-1} region, (b) 2900-3500 cm^{-1} region.

(a)

(b)
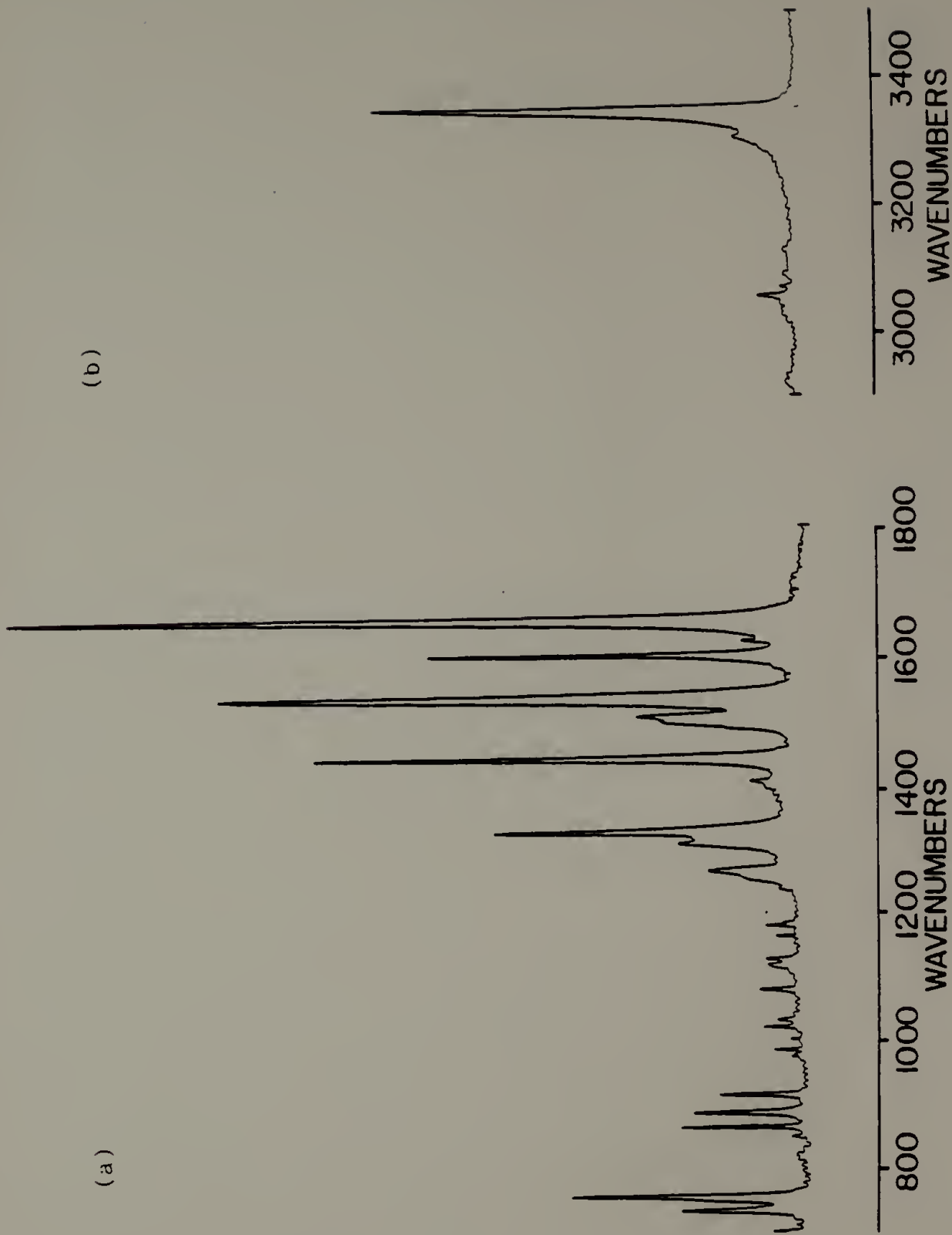
Figures 7.

Figure 8.   Infrared spectra of N,N'-dibenzoyl-p-phenylene diamine.
Resolution 2 cm^{-1}; 500 scans. (a) 700-1800 cm^{-1} region, (b) 2900-
3500 cm^{-1} region.

(a)

(b)
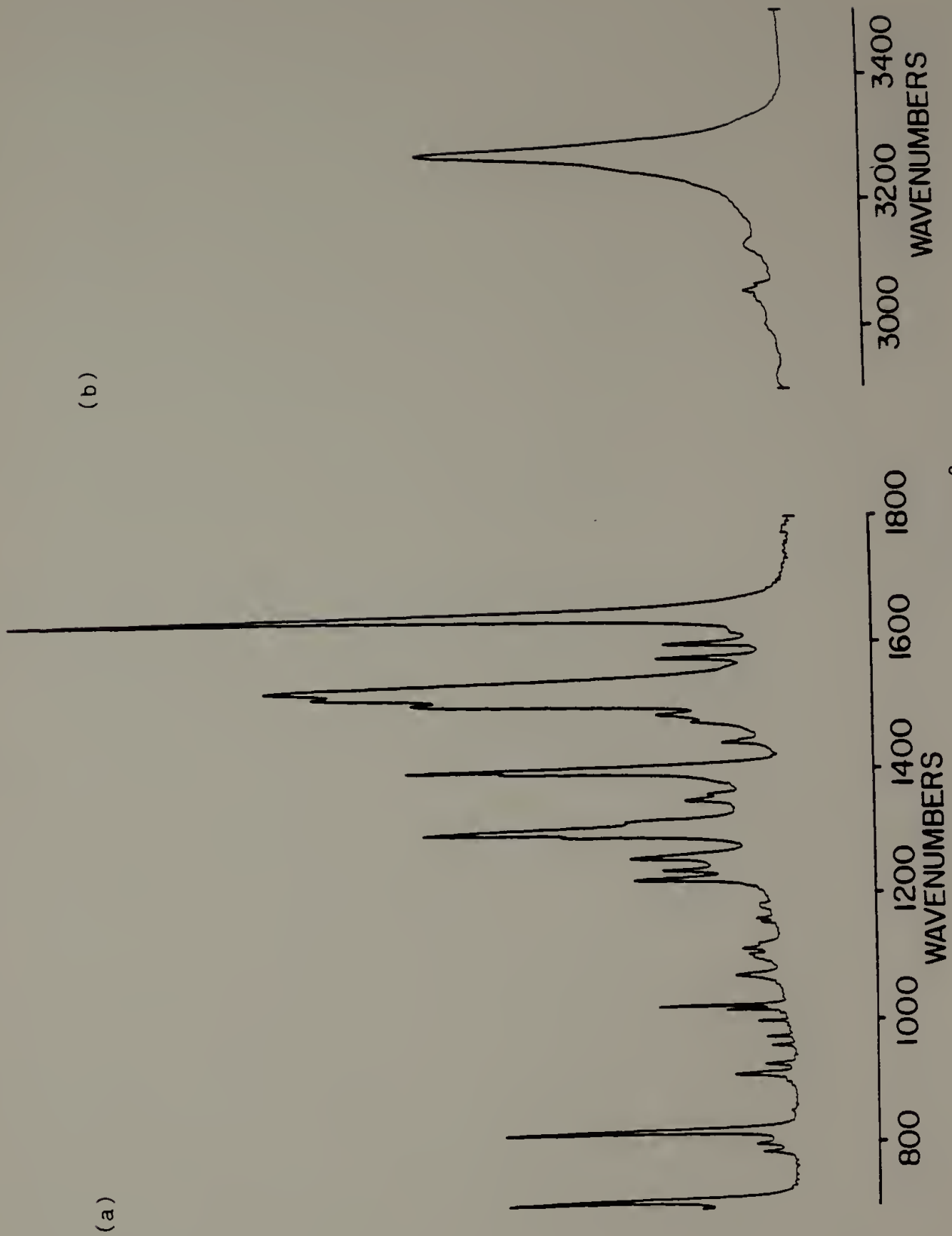
Figure 8.

Figure 9.   Raman spectra of N,N'-phenylterephthalamide.   Incident excitation radiation wavelength 514.5 nm; 1 cm^{-1} bandpass at 500 nm. (a) 0-2000 cm^{-1} region, (b) 2500-3500 cm^{-1} region.
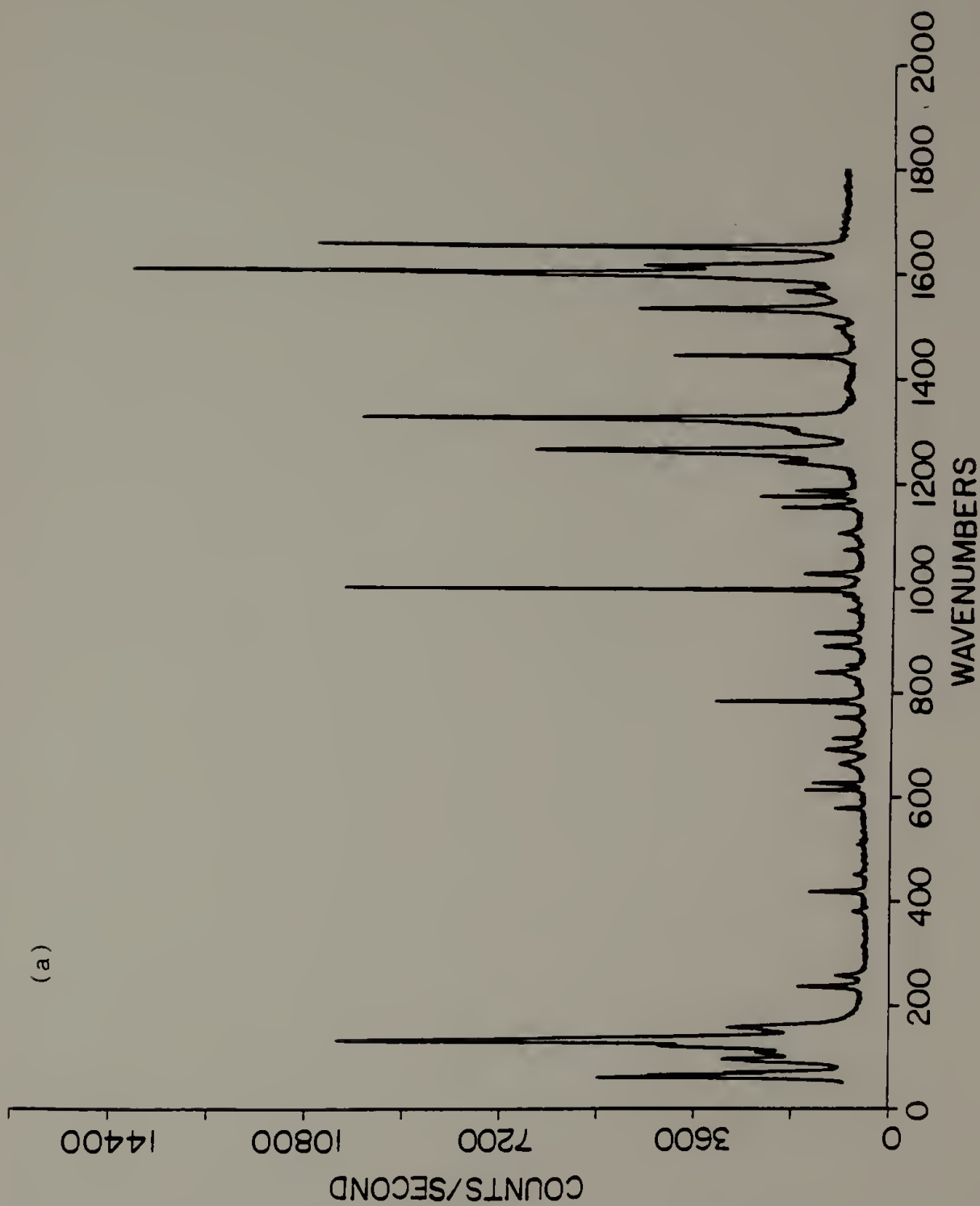
Figure 9.

(b)
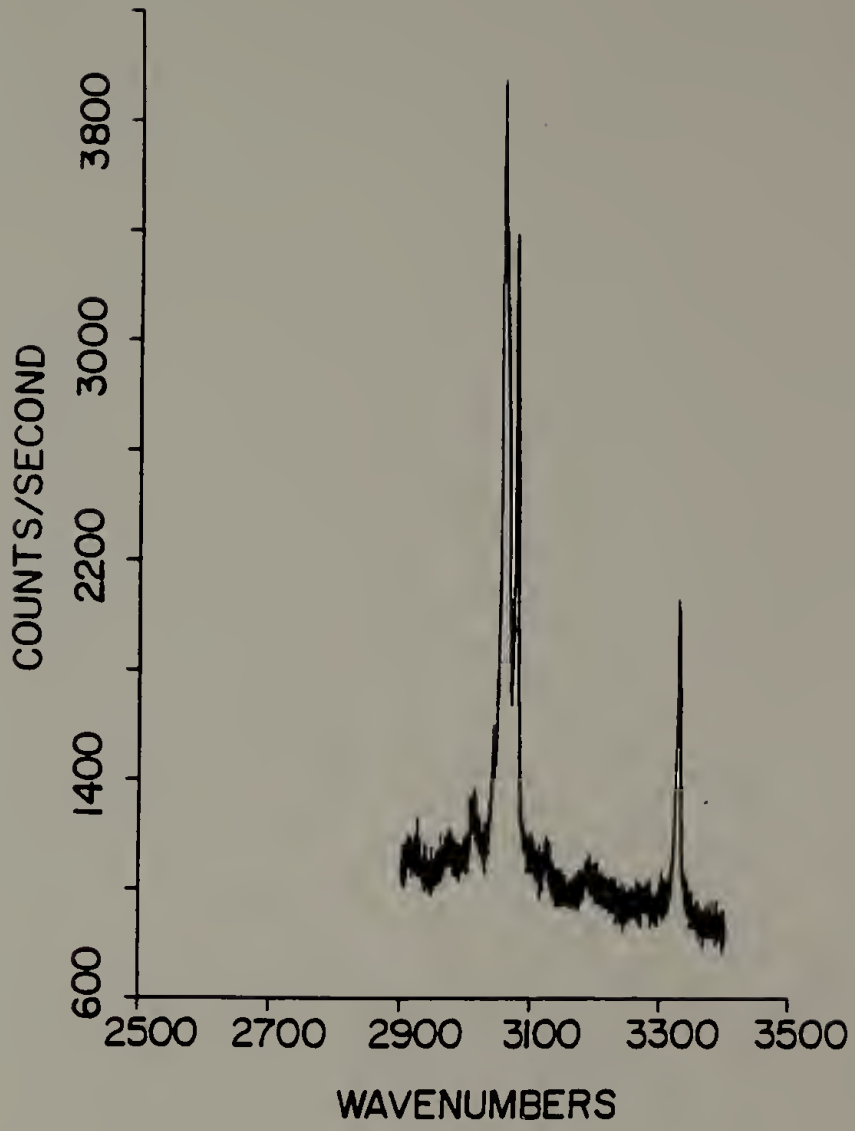
Figure 9.

Figure 10.   Raman spectra of N,N'-dibenzoyl-p-phenylene diamine.
Incident excitation radiation wavelength 514.5 nm; 1 cm^{-1} bandpass at
500 nm.   (a) 0-2000 cm^{-1} region, (b) 2500-3500 cm^{-1} region.

Figure 10.

(b)
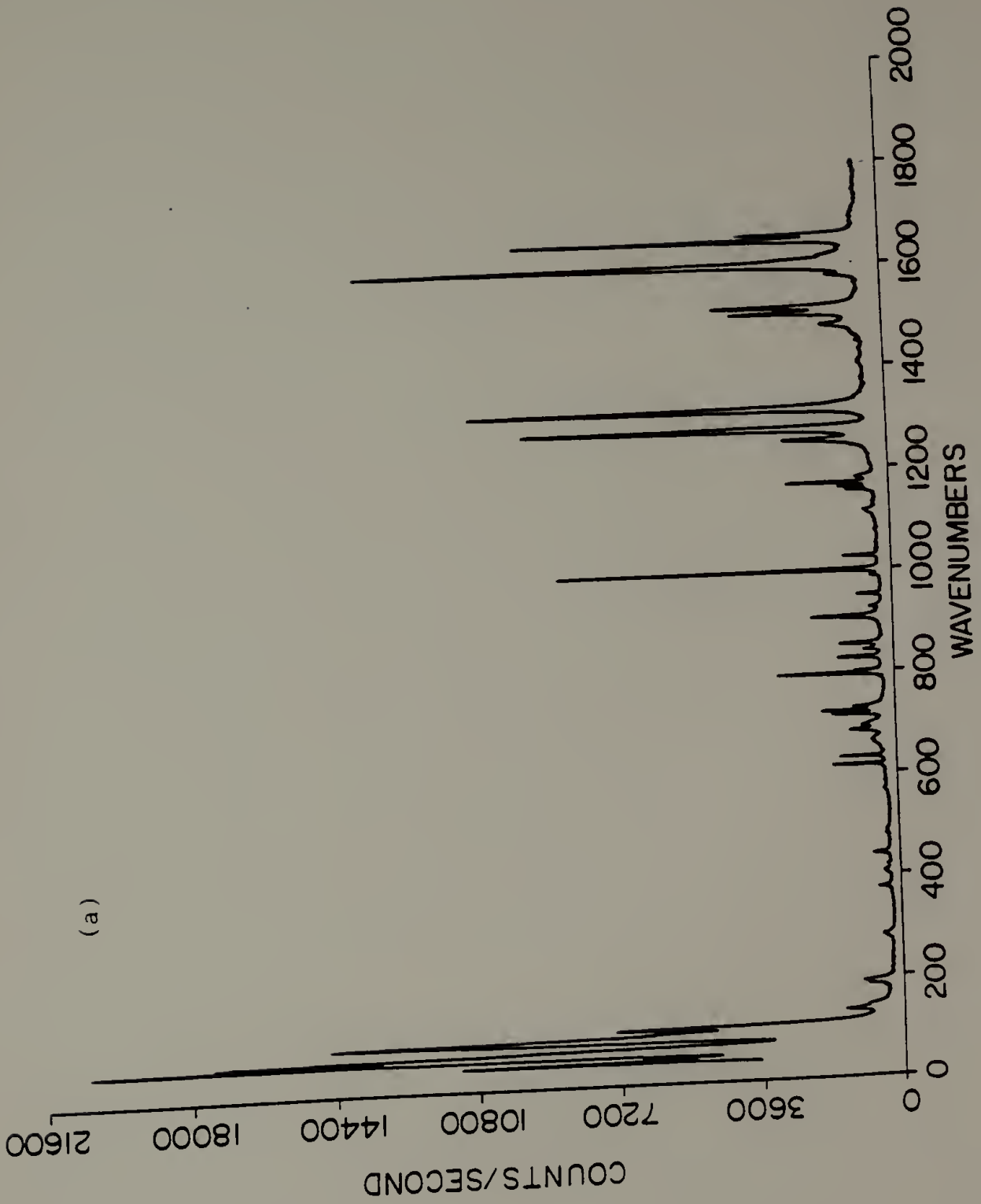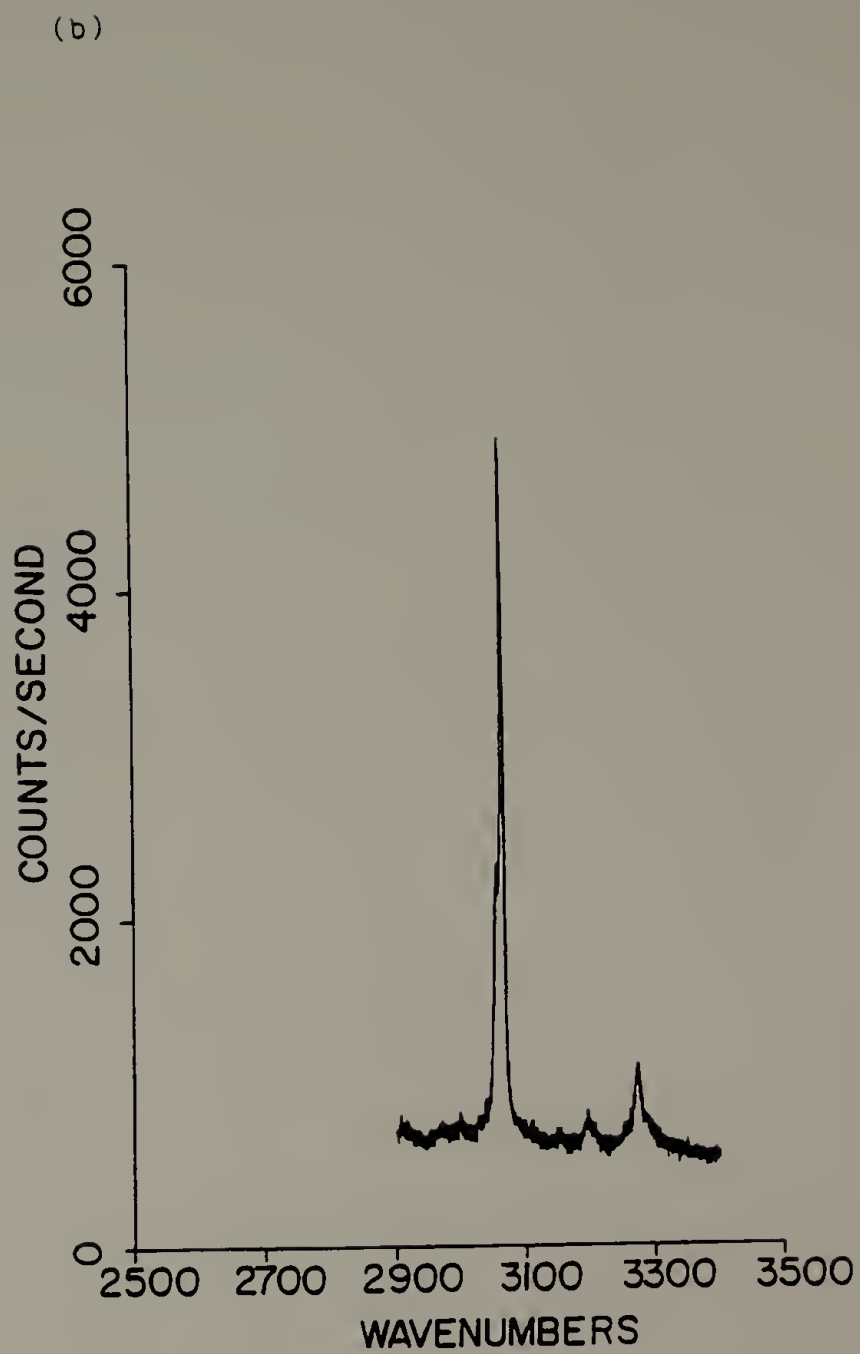
Figure 10.

500 nm. The excitation radiation is the 514.5 nm line provided by a continuous-wave Argon ion laser. No more than 120 mW were used in any of our experiments. Since this Raman spectrometer has very high stray light rejection ratios in the low frequency region, we were able to obtain the entire range (50 cm^{-1} to 3600 cm^{-1}) of a spectrum for structural characterization from these powdery samples. The Raman spectra of the model compounds are shown in Figures 9 and 10. Because of the extremely small fiber diameter (12 μm) of the Kevlar[R] 49 fibers, it was difficult to obtain transmission spectra without having the fibers overlap. Instead, the attenuated total reflectance technique was used. The fibers were wrapped around a germanium crystal with fibers parallel to each other. The entire assembly was dried in a vacuum oven at $100^{\circ}C$ for 24 hours. Polarized infrared radiation was obtained by using a wire grid polarizer. The polarized spectra obtained in this fashion are shown in Figure 11. We encountered a considerable amount of fluorescence background in the Raman measurement of the fibers received and have elected to use the data presented in the literature [44].

In addition, we have prepared PPTA film from the as-received fibers to study the effects of the coagulants, modifiction of the crystalline structure, and to obtain deuterated PPTA. Kevlar[R] 29 fibers were cut into 1-2 cm long segments and dried at $150^{\circ}C$ in vacuum oven for 24 hours before dissolving in 100% sulfuric acid. The polymer concentration is approximately 4-5 wt. %. This films were prepared by smearing the solution onto the glass plates and coagulating in water or methanol. To obtain deuterated films, D_2SO_4 and D_2O were used in place of H_2SO_4 and

Figure 11. Infrared spectra of PPTA fiber (ATR technique). Resolution
2 cm^{-1}; 500 scans. (a) unpolarized, (b) parallel polarized,
(c) perpendicular polarized incident light.
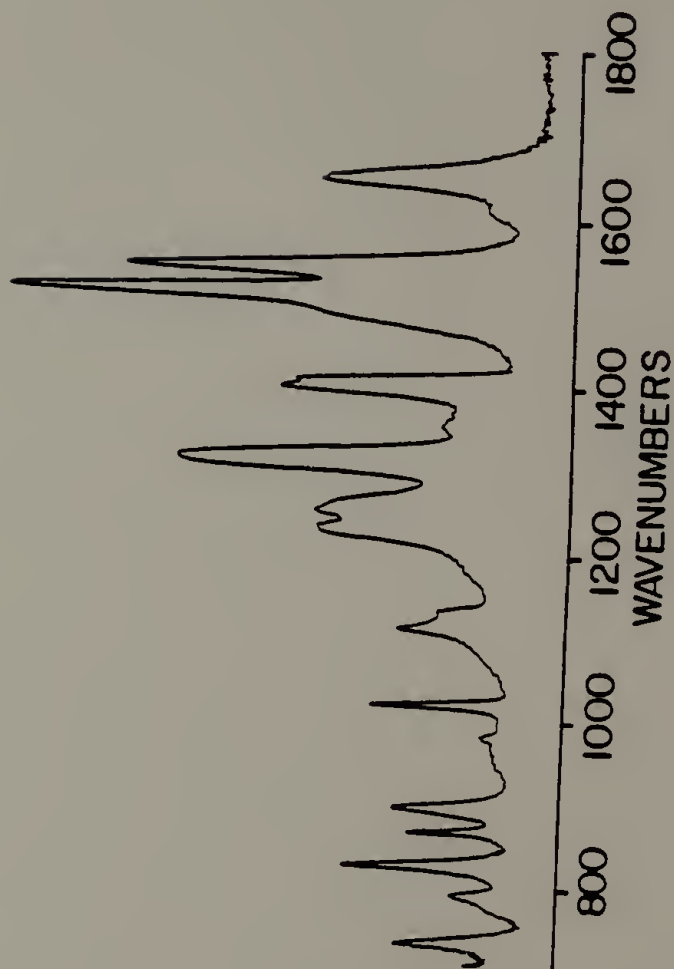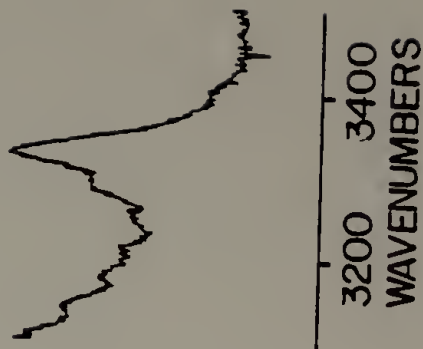
Figure 11.

(b)
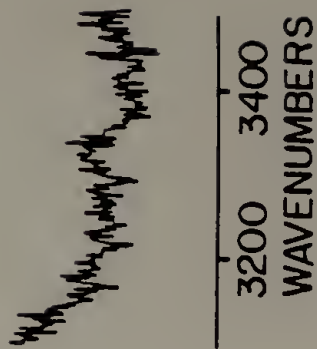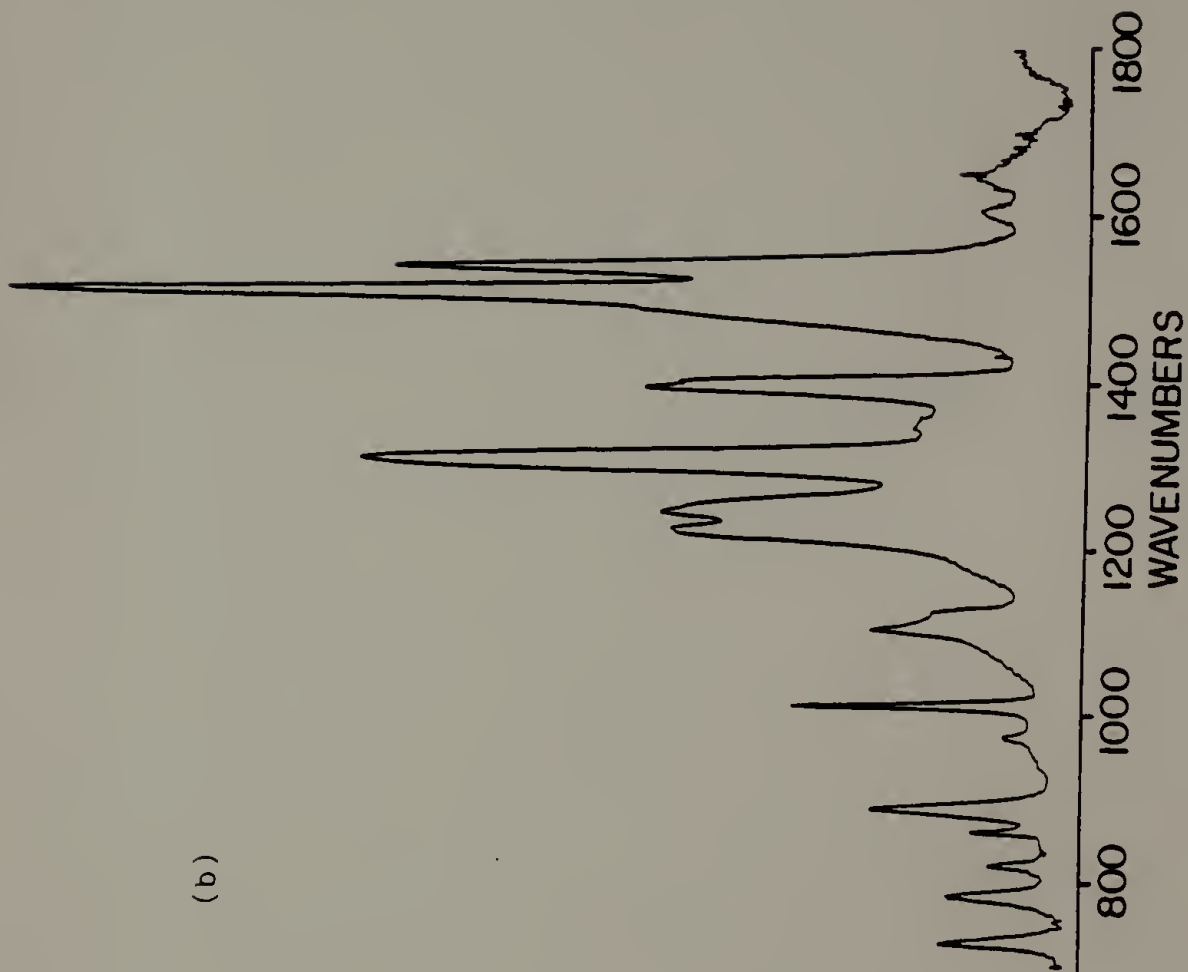
Figure 11.
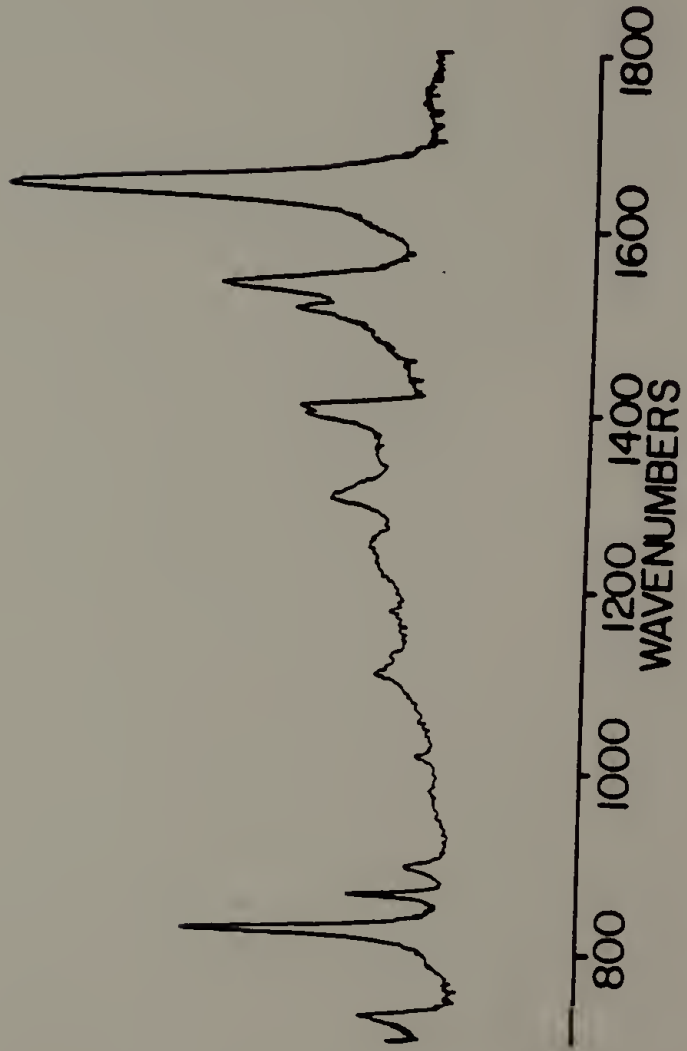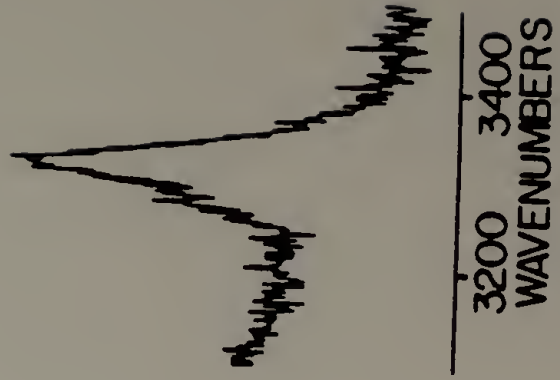
Figure 11.

Figure 12. Infrared spectra of hydrogenated PPTA film, -CONH-.
Resolution 2 cm^{-1}; 500 scans. (a) 400-1800 cm^{-1}, (b) 2000-3600 cm^{-1}
region.

(a)

(b)

2x

WAVENUMBERS

WAVENUMBERS
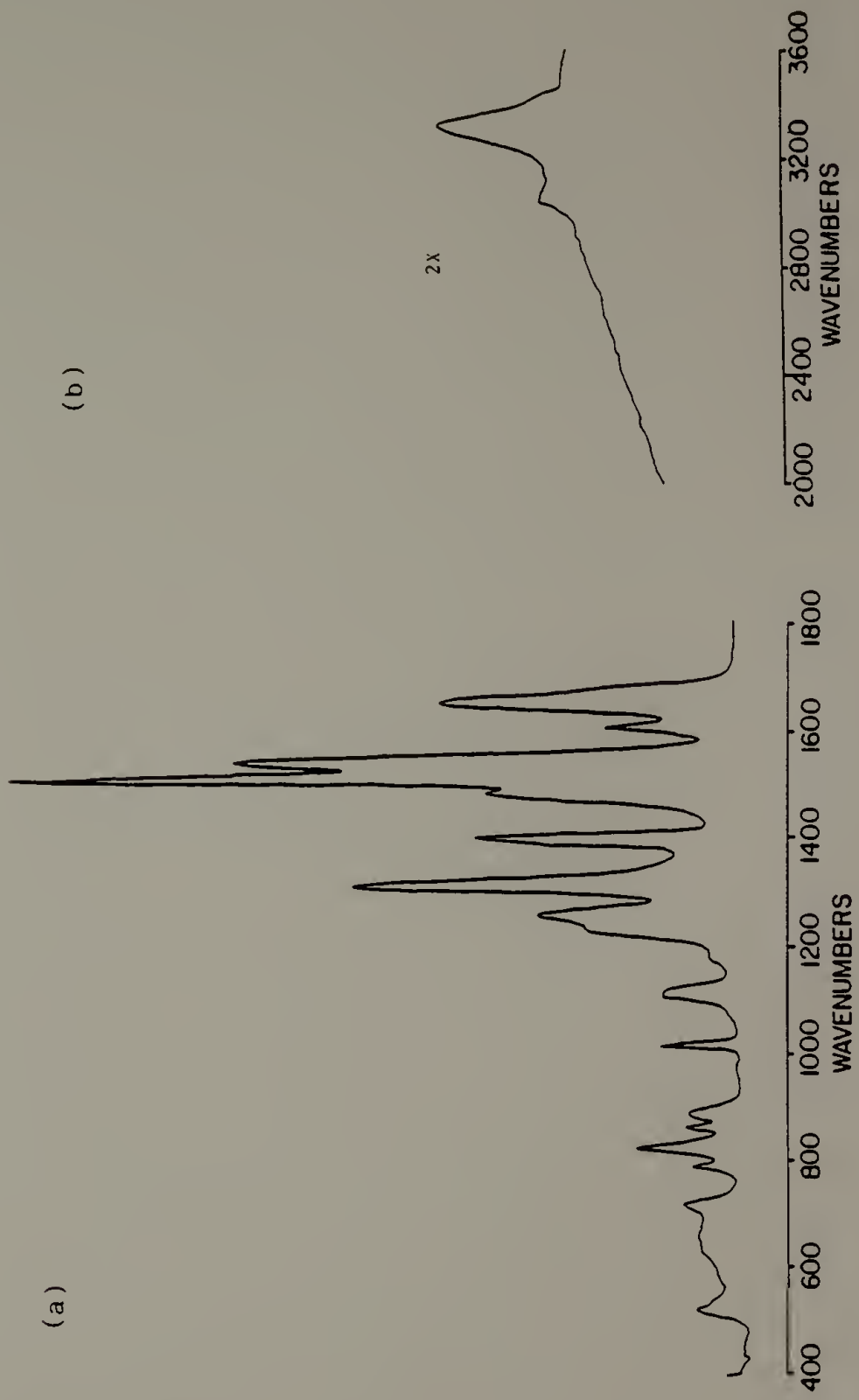
Figure 12.

Figure 13. Infrared spectra of deuterated PPTA film, -COND-.
Resolution 2 cm^{-1}; 500 scans. (a) 400-1800 cm^{-1} region, (b) 2000-
3600 cm^{-1} region.
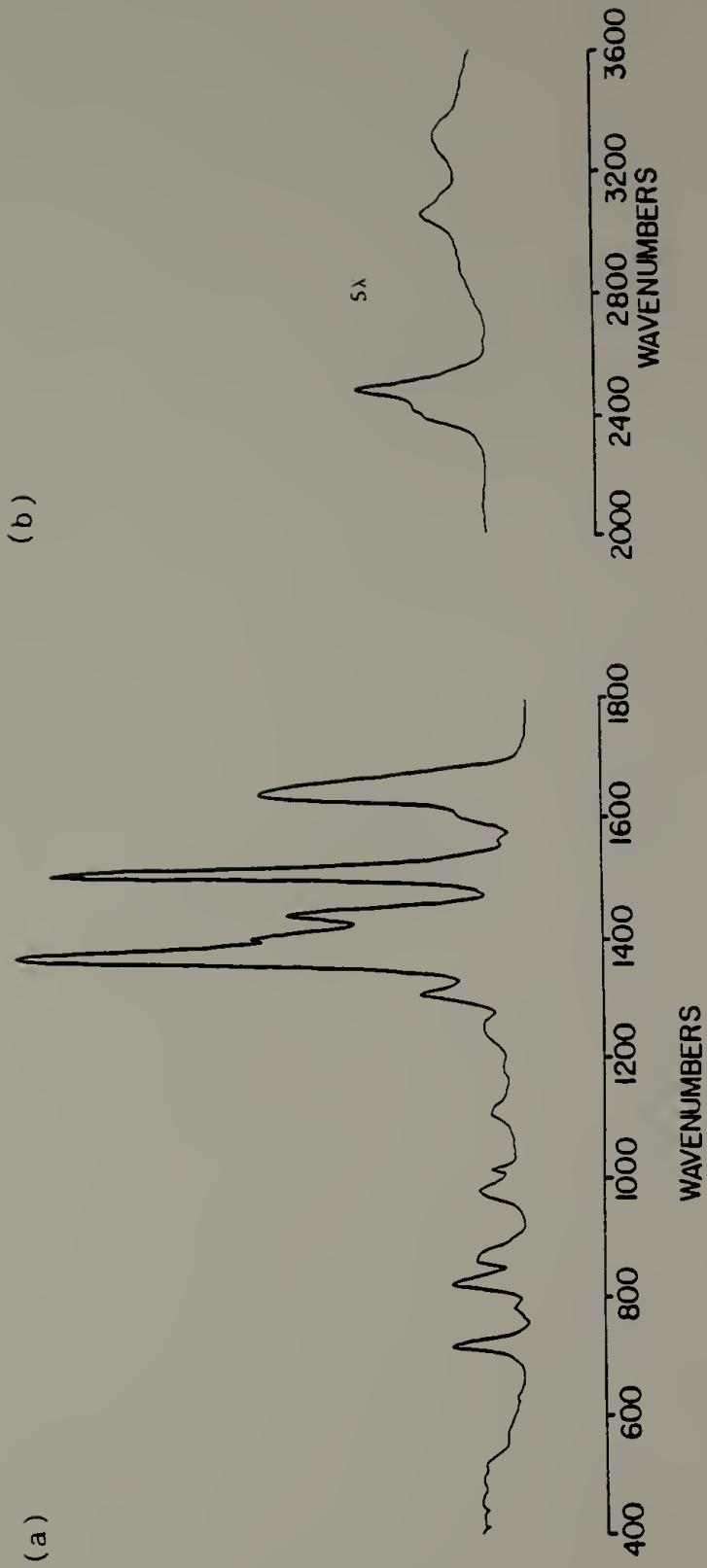
Figure 13.

Figure 14.   Schematic diagram of PPTA structure.
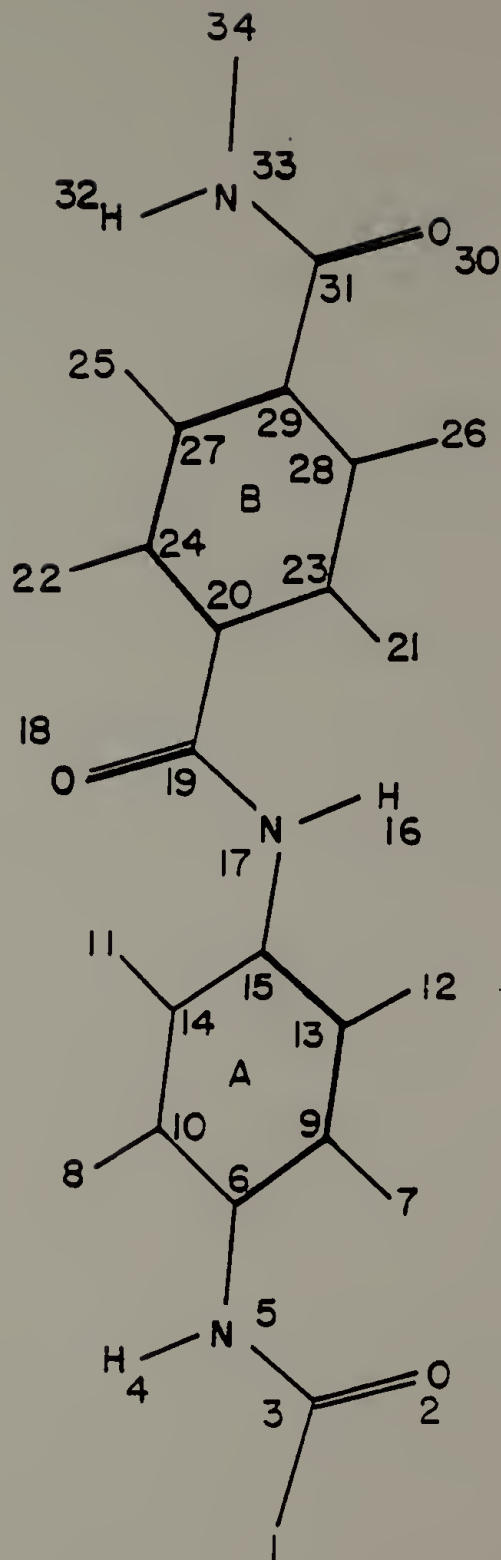
Figure 14.

H_2O. The infrared spectra obtained for these samples are shown in Figures 12 and 13. Although the infrared spectra of the regenerated PPTA films are essentially identical to the fiber spectra, X-ray diffraction studies show no clear spacing, indicating a decrease in orderliness for these films. Low temperature (100 K) infrared spectra were also obtained for these PPTA films using a low temperature cell constructed in our laboratory.

III.3 <u>NORMAL COORDINATE ANALYSIS: STRUCTURE AND FORCE FIELD</u>

The PPTA structure used for our normal coordinate analysis is taken from X-ray diffraction studies without modification [22]. The structure deduced is in agreement with the theoretical conformational analysis of a single chain [43]. The structure is shown schematically in Figure 14. he structural parameters are listed in Table 6. The internal coordinates used in the calculation are listed in Table 7. The definition of the internal coordinates and the construction of non-redundant symmetry coordinates are identical to those in the Chapter II. However, in this polymer calculation, we were not able to remove the four non-vibrational motions (three translation and one rotation) from the set of non-redundant symmetry coordinates listed in Table 8. In our analysis, the force fields are directly transferred from the analysis of benzanilide. The force constant changes needed for PPTA due to the para-substitution of benzene ring were minor. The

entire set of force constants is listed in Table 9. The observed and the calculated frequencies and the associated PEDs for both hydrogenated and deuterated PPTA molecules are listed in Tables 10 and 11.

III.4   RESULTS AND DISCUSSION

III.4.1   Vibrational Analysis

In our analysis, since the non-redundant local symmetry coordinates are well defined, localized ring vibrational bands between 1620 and 1000 cm^{-1} can be assigned by examining their PEDs in conjunction with the results of previous studies on para-substituted benzene ring [92]. The bands in this region all have significant contributions from in-plane ring vibrational motions. Bands calculated near 1605 cm^{-1}, 1595 cm^{-1}, 1295 cm^{-1}, and 1254 cm^{-1} are largely due to ring CC stretching modes, whereas bands calculated near 1516 cm^{-1}, 1332 cm^{-1}, 1312 cm^{-1}, and 1188 cm^{-1} are largely due to ring CH in-plane bending modes. Other calculated bands around 1400 cm^{-1}, 1106 cm^{-1}, and 1095 cm^{-1} have similar magnitudes of contributions from both ring CC stretching and ring CH in-plane bending modes. The band at 1014 cm^{-1} has a large contribution from the ring trigonal deformation involving deformation of the ring CCC angle and similar contributions from ring CC stretching modes. In addition to the mixing among CC stretching, CH in-plane bending, and planar deformation modes of one ring to the other, there are also

TABLE 6

Structural Parameters of a Proposed Geometry of PPTA

Length (Å)		Valence Angle (°)		Dihedral Angle (°)	
C-C	1.397	<(CCC)	120	τ(CCCC)	180
C-H	1.084	<(CCH)	120	τ(CCCH)	360
N-H	1.084	<(CCN)	120	$\tau(C_{23}C_{20}C'O)$	30
C-N	1.420	<(CCC')	120	$\tau(C_{27}C_{29}C'O)$	330
N-C'	1.340	<(CNH)	120	$\tau(C_9C_6NH)$	330
C'-O	1.240	<(CNC')	125	$\tau(C_{10}C_6NH)$	218
C'-C*	1.470	<(CC'O)	120	$\tau(C_{27}C_{29}C'N)$	150
		<(NC'C)	117	$\tau(C_{24}C_{20}C'O)$	210
				$\tau(C_{14}C_{15}NH)$	38
				$\tau(C_{14}C_{15}NC')$	218

* C' = carbonyl carbon

  C = benzene ring carbon

TABLE 7

Definition of Internal Coordinates for PPTA

Stretching

		Atoms
R_1	= r(N-H)	(4,5)
R_2	= r(N-C)	(5,6)
R_3	= r(C-H)	(7,9)
R_4	= r(C-H)	(12,13)
R_5	= r(C-N)	(17,15)
R_6	= r(C-H)	(11,14)
R_7	= r(C-H)	(8,10)
R_8	= r(C-C)	(6,9)
R_9	= r(C-C)	(9,13)
R_{10}	= r(C-C)	(13,15)
R_{11}	= r(C-C)	(15,14)
R_{12}	= r(C-C)	(14,10)
R_{13}	= r(C-C)	(6,10)
R_{14}	= r(N-H)	(16,17)
R_{15}	= r(N-C')	(17,19)
R_{16}	= r(C'-O)	(18,19)
R_{17}	= r(C'-C)	(19,20)
R_{18}	= r(C-H)	(21,23)
R_{19}	= r(C-H)	(26,28)
R_{20}	= r(C-C')	(31,29)
R_{21}	= r(C-H)	(25,27)
R_{22}	= r(C-H)	(22,24)
R_{23}	= r(C-C)	(20,23)
R_{24}	= r(C-C)	(23,28)
R_{25}	= r(C-C)	(28,29)
R_{26}	= r(C-C)	(29,27)
R_{27}	= r(C-C)	(27,24)
R_{28}	= r(C-C)	(24,20)
R_{29}	= r(C'-O)	(30,31)
R_{30}	= r(C'-N)	(31,33)

TABLE 7 (continued)
Angle bending

R_{31}	=	<(HNC')	(4,5,3)
R_{32}	=	<(HNC)	(4,5,6)
R_{33}	=	<(C'NC)	(3,5,6)
R_{34}	=	<(CCN)	(10,6,5)
R_{35}	=	<(NCC)	(5,6,9)
R_{36}	=	<(CCH)	(6,9,7)
R_{37}	=	<(HCC)	(7,9,13)
R_{38}	=	<(CCH)	(9,13,12)
R_{39}	=	<(HCC)	(12,13,15)
R_{40}	=	<(CCN)	(13,15,17)
R_{41}	=	<(NCC)	(17,15,14)
R_{42}	=	<(CCH)	(15,14,11)
R_{43}	=	<(HCC)	(11,14,10)
R_{44}	=	<(CCH)	(14,10,8)
R_{45}	=	<(HCC)	(8,10,6)
R_{46}	=	<(CCC)	(10,6,9)
R_{47}	=	<(CCC)	(6,9,13)
R_{48}	=	<(CCC)	(9,13,15)
R_{49}	=	<(CCC)	(13,15,14)
R_{50}	=	<(CCC)	(15,14,10)
R_{51}	=	<(CCC)	(14,10,6)
R_{52}	=	<(CNH)	(15,17,16)
R_{53}	=	<(HNC')	(16,17,19)
R_{54}	=	<(CNC')	(15,17,19)
R_{55}	=	<(NC'O)	(17,19,18)
R_{56}	=	<(OC'C)	(18,19,20)
R_{57}	=	<(CN'C)	(17,19,20)
R_{58}	=	<(CCC')	(24,20,19)
R_{59}	=	<(C'CC)	(19,20,23)
R_{60}	=	<(CCH)	(20,23,21)
R_{61}	=	<(HCC)	(21,23,28)
R_{62}	=	<(CCH)	(23,28,26)
R_{63}	=	<(HCC)	(26,28,29)
R_{64}	=	<(CCC')	(28,29,31)
R_{65}	=	<(C'CC)	(31,29,27)
R_{66}	=	<(CCH)	(29,27,25)
R_{67}	=	<(HCC)	(25,27,24)
R_{68}	=	<(CCH)	(27,24,22)
R_{69}	=	<(HCC)	(22,24,20)
R_{70}	=	<(CCC)	(24,20,23)
R_{71}	=	<(CCC)	(20,23,28)
R_{72}	=	<(CCC)	(23,28,29)
R_{73}	=	<(CCC)	(28,29,27)
R_{74}	=	<(CCC)	(29,27,24)
R_{75}	=	<(CCC)	(27,24,20)
R_{76}	=	<(CC'O)	(29,31,30)
R_{77}	=	<(OC'N)	(30,31,33)
R_{78}	=	<(CC'N)	(29,31,33)

TABLE 7 (continue)

Out-of-Plane Bending

		Atoms
R_{79} = NH opb		(5,4,3,6)
R_{80} = CN opb		(6,5,10,9)
R_{81} = CH opb		(9,7,6,13)
R_{82} = CH opb		(13,12,9,15)
R_{83} = CN opb		(15,17,13,14)
R_{84} = CH opb		(14,11,15,10)
R_{85} = CH opb		(10,8,14,6)
R_{86} = NH opb		(17,16,19,15)
R_{87} = C'O opb		(19,18,20,17)
R_{88} = CC' opb		(20,19,24,23)
R_{89} = CH opb		(23,21,20,28)
R_{90} = CH opb		(28,26,23,29)
R_{91} = CC' opb		(29,31,28,27)
R_{92} = CH opb		(27,25,29,24)
R_{93} = CH opb		(24,22,27,20)
R_{94} = C'O opb		(31,30,29,33)

Torsion

		Atoms
R_{95} = C-N tor		(6,5)
R_{96} = C-C tor		(6,9)
R_{97} = C-C tor		(9,13)
R_{98} = C-C tor		(13,15)
R_{99} = C-C tor		(15,14)
R_{100} = C-C tor		(14,10)
R_{101} = C-C tor		(10,6)
R_{102} = C-N tor		(15,17)
R_{103} = C'-N tor		(17,19)
R_{104} = C'-C tor		(19,20)
R_{105} = C-C tor		(20,23)
R_{106} = C-C tor		(23,28)
R_{107} = C-C tor		(28,29)
R_{108} = C-C tor		(29,27)
R_{109} = C-C tor		(27,24)
R_{110} = C-C tor		(24,20)
R_{111} = C-C' tor		(29,31)
R_{112} = C'-N tor		(31,33)

TABLE 8
Definition of Local Non-Redundant Symmetry Coordinates for PPTA

	Notation	Ring A
C-N str	r'	$S_1 = R_2$
C-H str	r	$S_2 = R_3$
C-H str		$S_3 = R_4$
C-N str	r'	$S_4 = R_5$
C-H str	r	$S_5 = R_6$
C-H str		$S_6 = R_7$
C-C str	R	$S_7 = R_8$
C-C str		$S_8 = R_9$
C-C str		$S_9 = R_{10}$
C-C str		$S_{10} = R_{11}$
C-C str		$S_{11} = R_{12}$
C-C str		$S_{12} = R_{13}$
CN ipb	β'	$S_{13} = (R_{35}-R_{34})/\sqrt{2}$
CH ipb	β	$S_{14} = (R_{37}-R_{36})/\sqrt{2}$
CH ipb	β	$S_{15} = (R_{39}-R_{38})/\sqrt{2}$
CN ipb	β'	$S_{16} = (R_{41}-R_{40})/\sqrt{2}$
CH ipb	β	$S_{17} = (R_{43}-R_{42})/\sqrt{2}$
CH ipb	β	$S_{18} = (R_{45}-R_{44})/\sqrt{2}$
trigonal def.	q_{19}	$S_{19} = (R_{46}-R_{47}+R_{48}-R_{49}+R_{50}-R_{51})/\sqrt{6}$
asy. def. A	q_{20}	$S_{20} = (2R_{46}-R_{47}-R_{48}+2R_{49}-R_{50}-R_{51})/\sqrt{12}$
asy. def. B	q_{21}	$S_{21} = (R_{47}-R_{48}+R_{50}-R_{51})/2$
CN opb	γ'	$S_{22} = R_{80}$
CH opb	γ	$S_{23} = R_{81}$
CH opb		$S_{24} = R_{82}$
CN opb	γ'	$S_{25} = R_{83}$
CH opb	γ	$S_{26} = R_{84}$
CH opb		$S_{27} = R_{85}$
puckering	q_{28}	$S_{28} = (R_{96}-R_{97}+R_{98}-R_{99}+R_{100}-R_{101})/\sqrt{6}$
asy. tor. A	q_{29}	$S_{29} = (-R_{96}+R_{98}-R_{99}+R_{101})/2$
asy. tor. B	q_{30}	$S_{30} = (-R_{96}+2R_{97}-R_{98}-R_{99}+2R_{100}-R_{101})/\sqrt{12}$

TABLE 8 (continued)

	Notation	Ring B
C-C' str	r''	$S_{43} = R_{17}$
C-H str	r	$S_{44} = R_{18}$
C-H str		$S_{45} = R_{19}$
C-C' str	r''	$S_{46} = R_{20}$
C-H str	r	$S_{47} = R_{21}$
C-H str		$S_{48} = R_{22}$
C-C str	R	$S_{49} = R_{23}$
C-C str		$S_{50} = R_{24}$
C-C str		$S_{51} = R_{25}$
C-C str		$S_{52} = R_{26}$
C-C str		$S_{53} = R_{27}$
C-C str		$S_{54} = R_{28}$
CC' ipb	β''	$S_{55} = (R_{59} - R_{58})/\sqrt{2}$
CH ipb	β	$S_{56} = (R_{61} - R_{60})/\sqrt{2}$
CH ipb	β	$S_{57} = (R_{63} - R_{62})/\sqrt{2}$
CC' ipb	β''	$S_{58} = (R_{65} - R_{64})/\sqrt{2}$
CH ipb	β	$S_{59} = (R_{67} - R_{66})/\sqrt{2}$
CH ipb	β	$S_{60} = (R_{69} - R_{68})/\sqrt{2}$
trigonal def.	q_{19}	$S_{61} = (R_{70} - R_{71} + R_{72} - R_{73} + R_{74} - R_{75})/\sqrt{6}$
asy. def. A	q_{20}	$S_{62} = (2R_{70} - R_{71} - R_{72} + 2R_{73} - R_{74} - R_{75})/\sqrt{12}$
asy. def. B	q_{21}	$S_{63} = (R_{71} - R_{72} + R_{74} - R_{75})/2$
CC' opb	γ''	$S_{64} = R_{88}$
CH opb	γ	$S_{65} = R_{89}$
CH opb		$S_{66} = R_{90}$
CC' opb	γ''	$S_{67} = R_{91}$
CH opb	γ	$S_{68} = R_{92}$
CH opb		$S_{69} = R_{93}$
puckering	q_{28}	$S_{70} = (R_{105} - R_{106} + R_{107} - R_{108} + R_{109} - R_{110})/\sqrt{6}$
asy. tor. A	q_{29}	$S_{71} = (-R_{105} + R_{107} - R_{108} + R_{110})/2$
asy. tor. B	q_{30}	$S_{72} = (-R_{105} + 2R_{106} - R_{107} - R_{108} + 2R_{109} - R_{110})/\sqrt{12}$

TABLE 8 (continued)

Amide Group

Notation		Ring A	Ring B
N–H str	t	$S_{31} = R_{14}$	$S_{73} = R_1$
N–C' str	R'	$S_{32} = R_{15}$	$S_{74} = R_{30}$
C'–O str	S	$S_{33} = R_{16}$	$S_{75} = R_{29}$
NH opb	μ	$S_{34} = R_{86}$	$S_{76} = R_{79}$
C'O opb	μ'	$S_{35} = R_{87}$	$S_{77} = R_{94}$
CC'N def.	δ'	$S_{36} = (2R_{57}-R_{56}-R_{55})/\sqrt{6}$	$S_{78} = (2R_{78}-R_{77}-R_{76})/\sqrt{6}$
Ψ÷↓ ιρβ	θ'	$S_{37} = (R_{56}-R_{55})/\sqrt{2}$	$S_{79} = (R_{76}-R_{77})/\sqrt{2}$
C'NC def.	δ	$S_{38} = (2R_{54}-R_{53}-R_{52})/\sqrt{6}$	$S_{80} = (2R_{33}-R_{32}-R_{31})/\sqrt{6}$
NH ipb	θ	$S_{39} = (R_{53}-R_{52})/\sqrt{2}$	$S_{81} = (R_{31}-R_{32})/\sqrt{2}$
CN tor.	τ_1	$S_{40} = R_{102}$	$S_{82} = R_{95}$
NC' tor.	τ_2	$S_{41} = R_{103}$	$S_{83} = R_{112}$
C'C tor.	τ_3	$S_{42} = R_{104}$	$S_{84} = R_{111}$

TABLE 9

Force Constants for PPTA

Force Constant	Value	Force Constant	Value
(a) phenyl group			
$K(r)$	5.104	$F(R)^o$	0.633
$K(r')$	5.043	$F(R)^m$	-0.442
$K(r'')$	4.409	$F(R)^p$	0.440
$K(R)$	6.500	$F(R_1\beta_1)$	0.167
$H(\beta)$	0.512	$F(R_1\beta_3)$	-0.010
$H(\beta')$	0.8375	$F(R_1\beta_4)$	0.019
$H(\beta'')$	0.8375	$F(R_1 q_{20})$	0.134
$H(q_{19})$	1.236	$F(R_2 q_{20})$	-0.268
$H(q_{20})$	1.236	$F(R_3 q_{20})$	-0.067
$H(q_{21})$	1.236	$F(R_1 q_{21})$	0.2321
$H(\gamma)$	0.5852	$F(R_3 q_{21})$	-0.2321
$H(\gamma')$	0.6581	$F(\beta)^o$	0.009
$H(\gamma'')$	0.6581	$F(\beta)^m$	0.010
$H(q_{28})$	0.3763	$F(\beta)^p$	-0.001
$H(q_{29})$	0.3156	$F(\beta_2 q_{20})$	-0.067
$H(q_{30})$	0.3156	$F(\beta' q_{21})$	0.07736
$F(r)^o$	0.016	$F(\beta'' q_{21})$	0.07736
$F(r)^m$	0.005	$F(\beta_2 q_{21})$	0.03863
$F(r)^p$	0.001	$F(\gamma)^o$	-0.092
$F(r_1 R_1)$	0.079	$F(\gamma)^m$	-0.00004
$F(r_1 R_2)$	-0.002	$F(\gamma)^p$	-0.0235
$F(r_1 R_3)$	-0.022	$F(\gamma_1 q_{28})$	-0.1681
$F(r_1 \beta_2)$	0.005	$F(\gamma_2 q_{28})$	0.1681
$F(r_1 \beta_3)$	-0.007	$F(\gamma' q_{29})$	0.1700
$F(r_1 q_{19})$	-0.105	$F(\gamma'' q_{29})$	0.1700
$F(r_2 q_{19})$	0.105	$F(\gamma_2 q_{29})$	-0.0850

TABLE 9 (continued)

Force Constant	Value	Force Constant	Value
(a) phenyl group (cont.)			
$F(r'q_{19})$	0.015	$F(\gamma_2 q_{30})$	-0.1472
$F(r''q_{19})$	-0.105	$F(\gamma_3 q_{30})$	0.1472
$F(r_2 q_{20})$	0.0495	$F(r'R_1)$	0.3000
$F(r'q_{20})$	-0.099	$F(r''R_1)$	0.2506
$F(r''q_{20})$	-0.099	$F(R_1\beta')$	0.2200
		$F(R_1\beta'')$	0.220
(b) amide group			
$K(t)$	6.168	$F(R'\theta')$	-0.1414
$K(R')$	6.415	$F(R'\delta)$	0.1249
$K(S)$	9.582	$F(R'\delta')$	0.1633
$H(\theta)$	0.6205	$F(S\delta')$	-0.4899
$H(\delta)$	0.6625	$F(r''\theta')$	0.1414
$H(\theta')$	1.246	$F(r''\delta')$	0.1633
$H(\delta')$	1.3487	$F(r'\theta)$	-0.2079
$H(\mu)$	0.129	$F(r'\delta')$	0.1249
$H(\mu')$	0.587	$F(\theta\theta')$	-0.1255
$H(\tau_1)$	0.010	$F(\delta\delta')$	-0.0248
$H(\tau_2)$	0.680	$F(\theta'\delta)$	0.0725
$H(\tau_3)$	0.010	$F(\theta\delta')$	0.043
$F(\gamma'R')$	0.300	$F(\theta\delta)$	0.0231
$F(R'S)$	0.500	$F(\mu\mu')$	0.010
$F(r''R')$	0.300	$F(\mu'\tau_2)$	0.011
$F(r''S)$	0.500	$F(\mu\tau_2)$	-0.1677
$F(R'\theta)$	0.2079		

TABLE 10

Observed and Calculated Frequencies (in cm-1) of PPTA (CONH)

IR*	Raman+	Calculated	Potential Energy Distribution++
3324		3344	17A(92)
		3344	17B(92)
		3062	1A(99)
		3062	1B(99)
		3059	1A(99)
		3059	1B(100)
3041		3040	1A(100)
		3040	1B(99)
		3039	1A(100)
		3039	1B(99)
		1065	19A(44),18A(22),22A(9)
1650	1649	1654	19B(59),18B(16),22B(12),19A(9)
	1615	1615	2A(19),2B(11),19A(10),14B(7)
1610		1605	2B(40),2A(24),5A(6),5B(6)
		1595	2A(52),3A(13),6A(6),25A(5)
		1580	2B(29),25B(11),19B(9),18A(8)
	1570	1567	2B(31),19A(13),25A(11),18B(7),3B(7)
1539		1528	25B(17),18B(14),25A(12),2B(7),14B(6)
1510	1518	1516	3A(42),2A(26),11B(7)
1484		1495	3B(40),25B(15),2B(14)
1406	1409	1400	3A(25),2A(21),3B(5)
1396		1391	3B(31),2B(22)
	1331	1332	3B(29),3A(24),25A(7),2B(6),14B(6)
1308		1318	2A(44),3A(24),25B(9),3B(7),14A(6)
		1312	3B(37),3A(25),2A(5)
		1295	2B(121),3B(6)
	1279	1283	25B(17),25A(13),3A(8),11A(6),2A(5)
1259		1254	2A(92),25B(8),25A(7),4A(6)
		1241	11B(15),2B(12),14A(8),11A(9),14B(7)
1226		1226	11A(19),2A(15),11B(15),14B(10),14A(7)
	1192	1188	3B(76)
1130	1187	1187	3A(74)
1109	1104	1106	3B(27),2B(16),4B(12),18B(5)
		1101	3A(50),2A(36)
		1095	3B(26),2B(22),4B(7),18B(7)
		1074	3B(27),18A(12),18B(7)
1017		1014	4A(35),2A(32)
		1013	4B(43),2A(28)
979		963	7B(124),10B(11)
		963	7A(124),10A(11)

TABLE 10 (continued)

IR[*]	Raman[+]	Calculated	Potential Energy Distribution[++]
		959	7B(65),7A(64),8B(28),8A(27)
		953	7B(68),7A(66),8B(23),8A(22)
894		893	7A(16),13B(10),9A(9),24B(9),22B(7)
		883	24A(11),22A(9),19A(6),23A(5),24B(5)
864		853	7B(64),9B(17),16A(11),16B(11),21A(5)
		843	2A(21),5B(8),9A(7)
		838	7B(112)
		838	7A(112)
823		824	7A(24),8B(16),13B(9),8A(9),27B(6)
		811	7A(48),8B(22),10A(7),16B(7),13B(7)
787	789	773	8A(69),8B(23),13A(17),13B(14),16A(6)
		746	4A(23),11B(12),11A(10)
728	734	725	5B(32),23A(7),23B(6)
	698	694	7B(39),21A(30),21B(16),16A(6)
668[**]		682	8A(32),21B(27),8B(17),20B(10),13A(6)
		661	8B(20),7A(10),13A(8),27B(8),21A(8)
	632	646	6B(67),6A(12)
		637	6A(59),6B(13)
		581	8A(34),27A(18),20A(16),8B(11)
		565	8B(34),5A(25),22B(11),22A(8)
		545	9B(20),9A(15),16B(10),16A(9),13A(10)
445		450	9A(44),13B(15),13A(14),16A(12),16B(9)
420		428	5A(16),5B(13),12A(6),15B(6),12B(6)
		421	9B(49),16A(15),16B(14),5A(10),20A(6)
		401	10B(131),10A(30)
		401	10A(131),10B(30)
346		343	12A(15),12B(13),5A(10),23B(7),23A(7)
		328	9B(21),33B(14),22A(14),11A(6)
		312	20A(46),27A(9),13B(6),13A(6)
		279	20B(24),12B(17),24A(13),13B(11),9A(9)
252		258	15B(22),15A(16),21A(9),13A(7),21B(6)
		242	15A(16),23B(11),16B(10),6B(8),24B(8)
		218	20B(53),27B(33),9A(16),21B(8)
		102	15B(25),15A(22),9A(18)
		93	27A(19),19B(18),12A(18),16A(11),13A(6)
		87	27B(50),20B(22),16B(12),12B(11),9B(9)
		75	24B(23),24A(23),22A(9),22B(8)
		28	28A(25),28B(24),26B(23),26A(22)
		22	26B(24),28A(22),26A(20),28B(16)
		19	26A(28),28A(27),26B(22),28A(22)

* Observed frequencies are from the ATR spectra of Kevlar[R] 49 fiber.
**Observed frequencies below 700 cm-1 are obtained from mid- and far-ir spectra of PPTA films.
+ Raman data is from Ref. 9.

TABLE 10 (continued)

++Number of the coordinate is followed by the potential energy in percent. Contributions less than six percent are not included. The coordinate definitions in potential energy distributions are:

1. ring C-H stretching
2. ring C-C stretching
3. ring C-H in-plane bending
4. ring trigonal deformation
5. ring asymmetric deformation - type 1
6. ring asymmetric deformation - type 2
7. ring C-H out-of-plane bending
8. ring puckering
9. ring asymmetric torsion - type 1
10. ring asymmetric torsion - type 2
11. C-N stretching
12. C-N in-plane bending
13. C-N out-of-plane bending
14. C'-C stretching
15. C'-C in-plane bending
16. C'-C out-of-plane bending
17. N-H(D) stretching
18. N-C' stretching
19. C'-O stretching
20. N-H(D) out-of-plane bending
21. C'-O out-of-plane bending
22. <NC'C bending
23. C'-O in-plane bending
24. <CNC' bending
25. N-H(D) in-plane bending
26. CN torsion
27. NC' torsion
28. C'C torsion

A and B distinguish two amide groups and two benzene rings as shown below:
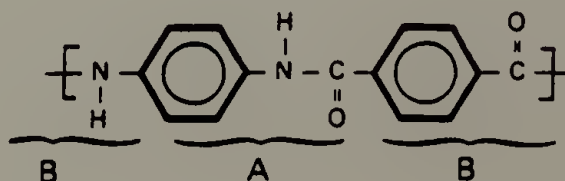
TABLE 11

Observed and Calculated Frequencies (in cm-1) of Deuterated PPTA (NDCO)

IR	Calculated	Potential Energy Distribution[++]
	3062	1A(81)
	3062	1B(80)
	3059	1A(99)
	3059	1B(99)
	3040	1A(94)
	3040	1B(94)
	3039	1B(96)
	3039	1A(96)
	2462	17A(98)
2475	2462	17B(98)
	1672	19A(45),18A(20),22A(9)
1645	1651	19B(56),18B(16),22A(9),19A(11)
	1609	2A(36),2B(14),5A(8)
1605	1606	2B(48),2A(19),5B(7)
	1587	2A(79),6A(10)
1565	1578	2B(57),19B(13)
	1543	14B(17),11A(13),18A(11)
1514	1515	3A(29),3B(18),2A(15)
	1473	18A(30),14B(15),23A(12),25A(8)
1446	1447	3B(16),18A(14),25B(7),23B(6)
1407	1399	3A(36),2A(26)
1379	1389	3B(35),2B(25)
	1321	3B(58),3A(11)
1310	1312	3A(51),3B(34)
	1294	2B(140)
	1287	2A(152)
1254	1240	11B(17),4A(16),11A(11),4B(7),14B(7),14A(6)
	1227	11A(18),11B(17),14A(10),14B(6),2A(15)
1183	1188	3B(54),3A(25)
	1187	3A(52),3B(25)
	1151	4B(18),4A(10),25A(8)
	1125	2B(18),25B(9),25A(7),14B(8)
1109	1101	2A(26),3A(35),3B(10)
	1100	2B(26),3B(34),2A(11)
1017	1014	4B(20),4A(17),2B(11)
	1014	4A(23),4B(19),2A(10)
982	978	25A(42),23A(12),8A(9)
	966	25B(45),8A(15),7A(26)
	963	7B(64),7A(62)
	963	7A(64),7B(62)

TABLE 11 (continued)

IR	Calculated	Potential Energy Distribution[++]
	957	7B(106),8B(42)
	948	7A(80),8A(21),7B(24),25B(12)
	882	7B(22),7A(14),10B(9),13B(8),9A(8),16B(7)
863	869	22A(8),24B(7),24A(7),22B(5)
	844	7B(50),16B(11),10B(11)
	838	7B(88),7A(24)
825	831	8B(11),16A(6)
	816	8B(21),16B(6),8A(6)
	808	7A(50),8B(14),9A(7)
	769	8A(78),8B(21),13A(17),13B(16)
	726	4A(15),11B(10),6B(7),11B(6)
719	719	6B(25),23A(10)
	692	7B(36),21A(29),21B(18)
	676	8B(31),21B(28),8A(21)
	650	6A(15),17B(10),7A(10),13A(9),8B(7)
	645	6B(63),6A(6)
	636	6A(53),6B(13)
	570	8A(34),27A(20),8B(12),20A(11)
	553	8B(26),5A(23),22B(14)
	541	10B(21),9A(14),16B(10),16A(10),13A(9)
	444	9A(32),10B(12),23A(14),23B(10),13A(10) 13B(10)
	425	5A(16),6B(13),12A(6),15A(5)
	413	9B(38),9A(21),16A(11),16B(10)
	401	10A(141),7A(24),10B(19)
	401	10B(142),7B(24),10A(19)
	338	12A(12),12B(12),5A(11),5B(7),23B(8),23A(7)
	326	9B(22),22B(14),22A(14)
	270	9A(20),24A(15),24B(13),20A(8),23A(8),12B(8)
	262	13B(13),13A(11),15B(10),15A(9)
	249	20A(13),15B(12),15A(11),5B(9),23B(8)
	231	20A(34),16B(13),21A(12)
	180	20B(65),27B(26)
	101	15A(24),15B(22),9A(19)
	92	9B(24),12A(18),27A(12),12B(9)
	82	27B(59),29B(34),27A(12),12B(9)
	74	24B(23),24A(23),22A(9),22B(23)
	28	28A(25),28B(24),26A(23),26B(23)
	22	26B(22),26A(21),28B(19),28A(19)
	20	26B(25),26A(25),28A(25),28B(25)

[++] For notation of the coordinates used in potential energy distribution, see footnotes to Table 10.

non-negligible contributions from the amide group vibrational modes in many of the vibrations. For example, the 1495 cm^{-1} band has a large contribution from the NH in-plane bending mode. This kind of mixing from the amide group is greater than that observed for its model compound, benzanilide (see Chapter II). As expected, the difference in structure between the two parts of the chemical repeat of PPTA affects not only the character of the ring vibrations but also their frequencies as well, even though exactly the same force constants were used. Comparing vibrational modes of similar characteristics, the frequencies are generally higher for PPTA than for benzanilide, ranging from less than 5 cm^{-1} for pure modes such as the ring CC stretching and ring CH in-plane bending at 1605 cm^{-1} and 1188 cm^{-1} respectively, to greater than 15 cm^{-1} for mixed modes at 1516 cm^{-1} and 1095 cm^{-1}. The band at 1449 cm^{-1} calculated for benzanilide disappears totally and a new band at 1400 cm^{-1} was calculated for PPTA. This is due to the presence of para-substitution of the benzene ring, and in fact, similar results are observed in comparing the normal coordinate analysis of toluene and p-xylene [92].

Out-of-plane ring deformation modes are similarly assigned by examining PEDs and comparing them with the normal coordinate analysis results of benzanilide and p-xylene [92]. Bands in the region between 1000 cm^{-1} and 800 cm^{-1}, for example 963 cm^{-1}, 959 cm^{-1}, 838 cm^{-1}, and 824 cm^{-1} are pure enough to be positively assigned to ring CH out-of-plane deformation bands. But again, these bands are not completely pure. The PEDs of thesebands show mixing of primarily ring

out-of-plane deformations between two rings and also with amide group in-plane and out-of-plane deformation modes.

In the region below 900 cm^{-1}, most of the vibrational modes are mainly due to skeletal modes and are difficult to assign with any degree of certainty. The complexity and the lack of dominating features make the characterization of these bands almost impossible without additional data. For example, bands at 893 cm^{-1}, 843 cm^{-1}, and 773 cm^{-1} all contain a considerable amount of coupling between the in-plane deformation modes of the ring and the out-of-plane deformation modes of both the ring and the amide group.

The assignments for the amide bands are greatly assisted by the deuteration experiment. By following the disappearance of the NH stretching and the appearance of the ND bands in the 3300 cm^{-1} and 2400 cm^{-1}, respectively, the extent of deuteration can be followed. It is interesting to note, however, that the NH band will re-emerge as a function of time when the film is simply exposed to air. The spectroscopic changes as a function of time are shown in Figure 15. It has been suggested that one of the deficiencies associated with PPTA is its propensity to absorb water [45]. We found that this is certainly the case and, in fact, occured readily for the films we prepared. Since the decrease in the intensity of the NH stretching vibration is proportional to the number of NH units around, the diffusion of the H_2O molecules can be followed by measuring the relative intensity of the two bands in the 3300 cm^{-1} and 2400 cm^{-1} regions. We recognize that this type of measurement is only an approximation since the absolute

Figure 15.   Infrared spectra of (a) N-H and (b) N-D stretching regions for deuterated PPTA film as a function of time (see Table 12).
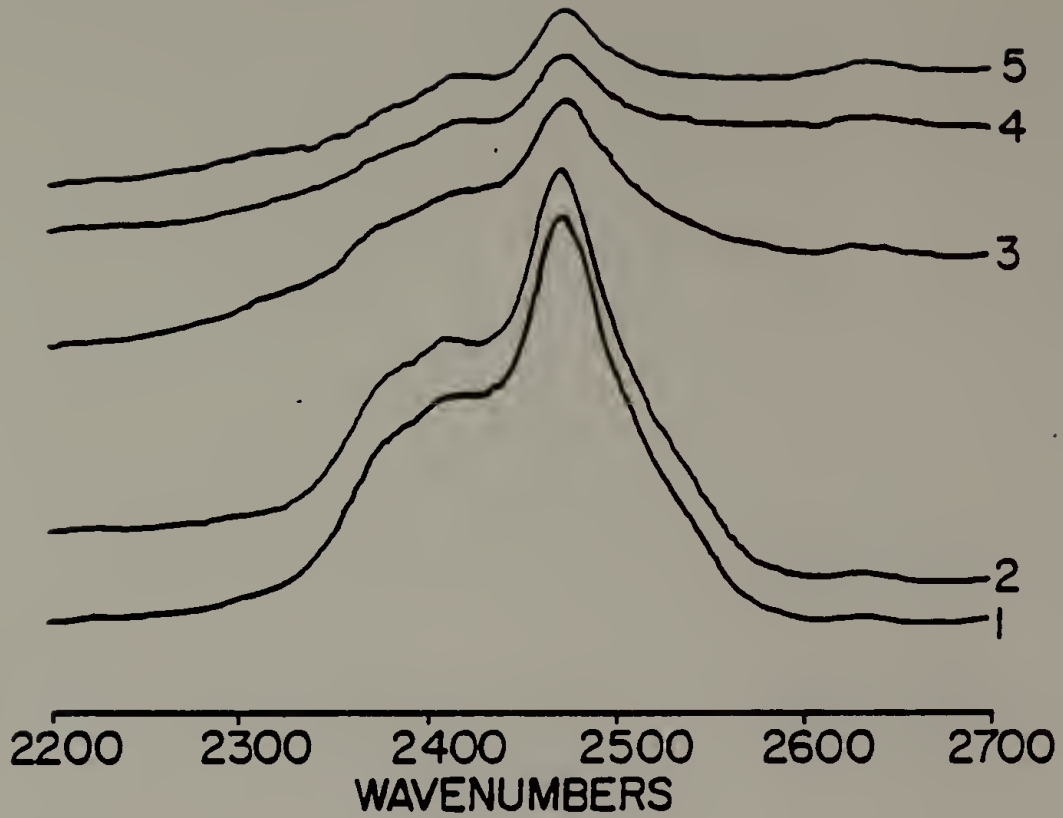
Figure 15.
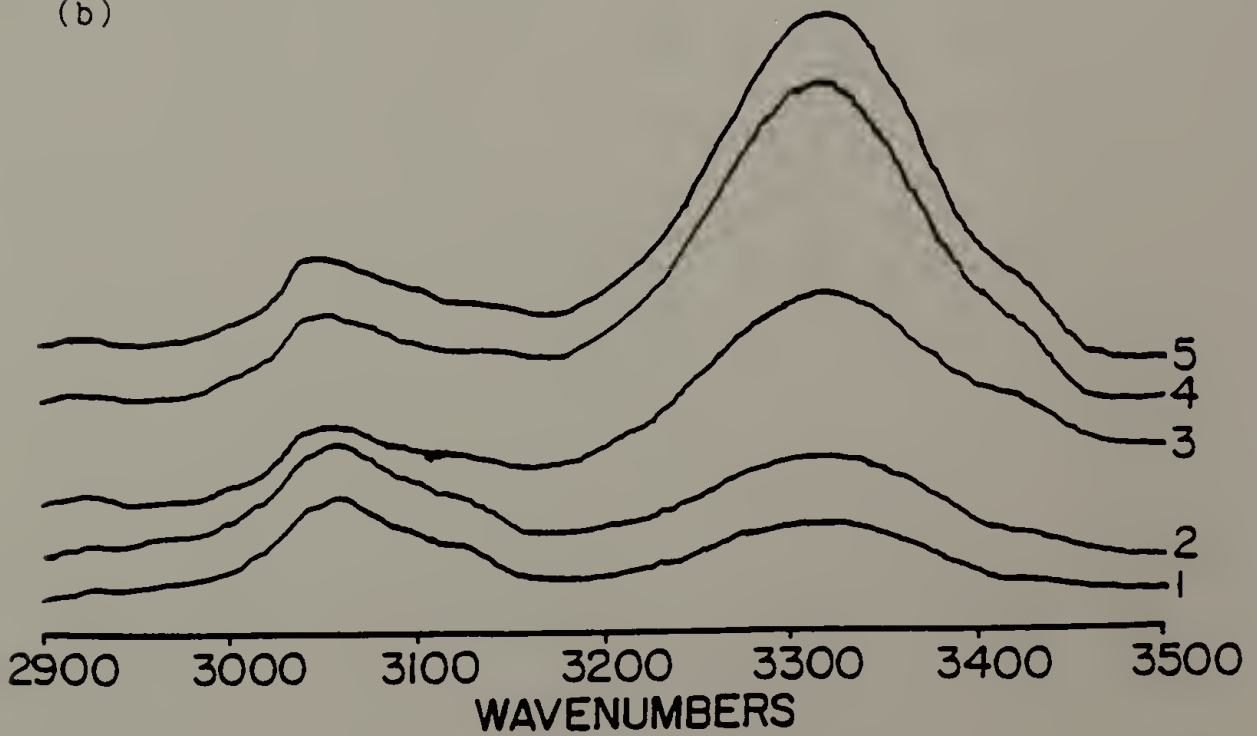
TABLE 12

Changes of NH and ND Stretching Band Intensities
of a Deuterated PPTA Film

Spectrum	Drying Conditions		Ratioed Band Intensity	
	Time (day)	Temp. (°C)	NH	ND
1	0.5	22	1	1
2	1.5	22	1.45	0.95
3	4	22	3.53	0.44
4	4	22	5.83	0.30
	1	90		
5	4	22	6.26	0.22
	2	90		

intensity of these vibrations do differ depending on the strength of the hydrogen bonds formed [105]. For the 8 μm thick film used in this study, there was an increase in the N-H content by a factor of three after four days at room temperature. The rate of change is shown in Table 12.

The amide bands, especially those in the higher frequency range, have been easily assigned by following the deuteration experiment. Because of the chemically different environments between the two amide groups and benzene rings within the chemical repeat unit of PPTA, we expected the degeneracy of the amide and ring vibrations to be lifted. Two bands at 1675 cm^{-1} and 1654 cm^{-1} have been calculated as the two Amide I bands associated with the two amide groups in the chemical repeat unit of PPTA. These two bands were calculated to be at 1672 cm^{-1} and 1651 cm^{-1} in the deuterated molecules, essentially unshifted from the original positions. This is to be expected since Amide I vibration does not involve significant NH contributions. The Amide I bands observed in hydrogenated and deuterated PPTA are at 1650 cm^{-1} and 1645 cm^{-1} respectively. These two bands are fairly broad, approximately 20 cm^{-1} in width. Even in the spectrum obtained at liquid nitrogen temperature, no evidence of the splitting was observed. However, at lower temperatures, the asymmetry of this Amide I band is enhanced.

Calculated Amide II bands at 1567 cm^{-1} and 1528 cm^{-1} are shifted considerably to 1473 cm^{-1} and 1447 cm^{-1}, respectively, upon deuteration. Therefore, the band observed at 1539 cm^{-1} is assigned to the Amide II vibration. Because of the significant NH in-plane bending contribution,

it shifted to 1446 cm^{-1} upon deuteration, close to the calculated value.
Similarly, the band observed at 1259 cm^{-1} is assigned to the Amide III
vibration, since it shifted to 982 cm^{-1} in the deuterated PPTA and its
PED shows typical contributions for Amide III vibration. The calculated
Amide III bands are at 1283 cm^{-1} and 1254 cm^{-1} for PPTA and 978 cm^{-1} and
966 cm^{-1} for deuterated PPTA. These assignments are consistent with the
polarization measurements of Kevlar^R 49 fiber, since Amide I is expected
to be perpendicularly polarized and Amide II and III are polarized in
the parallel direction with respect to the chain direction as seen in
Figure 5.

Perhaps one of the most fascinating aspects of the Kevlar^R fiber
spectrum is the considerable width observed for the infrared and Raman
bands. All the bandwidths observed for the model compounds are
approximately half of the values observed for the polymer. Several
factors attribute to the increase in the width of a vibrational band,
including the conformational distribution of the chain and the lack of
interchain order. The diffraction studies led to the conclusion that
PPTA fibers are of essentially 100% crystallinity, containing few
conformational or packing disorders [20]. Undoubtedly, because of
differences in the chemical structures and environments, we expected
different frequencies to exist for both amide groups and benzene rings,
and especially for vibrational modes coupled to the backbone. In a
similar case, we have already seen the calculated and observed
differences for the two rings in benzanilide. Therefore, guided by the

Figure 16. Infrared spectra of the sum of spectra of two model compounds for PPTA. (///) N,N'-dibenzoyl-p-phynylene diamine, (///) N,N'-phenylterephthalamide. (a) 700-1200 cm^{-1} region, (b) 1200-1800 cm^{-1} region, (c) 3000-3600 cm^{-1} region.

Figure 16.

(a)

700   800   900   1000   1100   1200   1300
WAVENUMBERS

(b)

1200   1300   1400   1500   1600   1700   1800
WAVENUMBERS

(c)

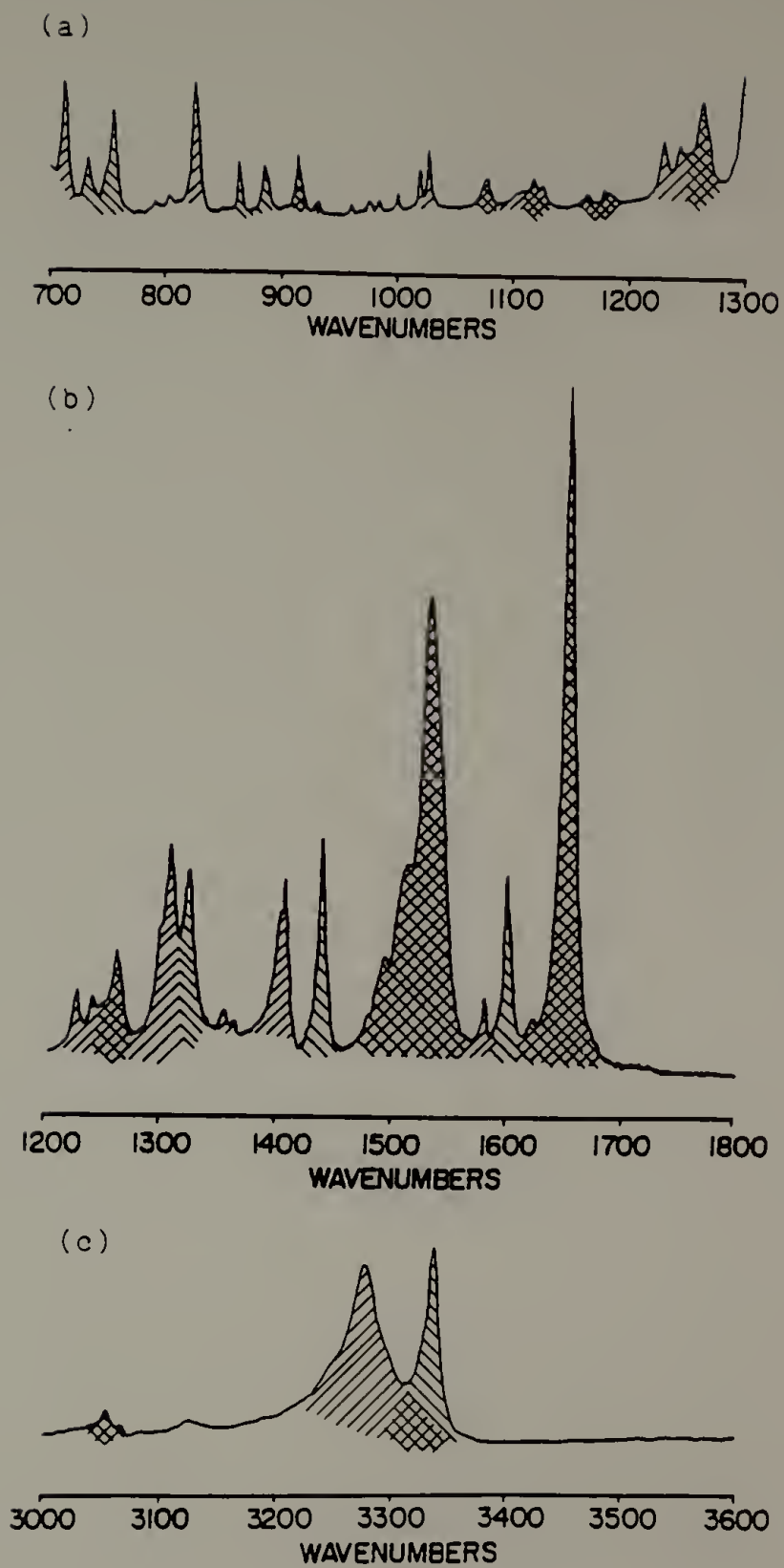3000   3100   3200   3300   3400   3500   3600
WAVENUMBERS

Figure 16.

vibrational analysis, we began to examine whether the vibrational spectrum of Kevlar[R] fiber is actually a sum of the spectra of two model compounds described in the experimental section. We paid particular attention to the regions near bands at 3320 cm^{-1}, 1400 cm^{-1}, 1310 cm^{-1}, 1260 cm^{-1}, and 1230 cm^{-1}. Excluding the obvious bands which arise from the mono-substituted benzene rings, such as the bands near 1441 cm^{-1}, 1076 cm^{-1}, and 1000 cm^{-1}, the broad bands observed for Kevlar[R] fiber can be constructed from the spectra obtained for the two model compounds as shown in Figure 16.

It is particularly fascinating to note the rather large difference between the NH stretching vibration for the two model compounds, one at 3279 cm^{-1} and the other at 3340 cm^{-1}. This vibrational mode is very localized in nature. Therefore, the difference is really due to the difference in the physical environment, i.e. the magnitude and the specificity of the hydrogen bonds formed. We have assigned the broad NH stretching vibration (halfwidth of 100 cm^{-1}) found in Kevlar[R] fiber to be associated mainly with the two different units in the repeat unit rather than assigning the broad bandshape strictly to poorly defined hydrogen bonds formed in association with ill defined structure.

The generally broad features of bands assigned to the amide group vibrations (1650 cm^{-1}, 1539 cm^{-1}, and 1259 cm^{-1}), or likewise those assigned to the ring vibrations (1610 cm^{-1}, 1510 cm^{-1}, 1360-1420 cm^{-1}, and 1308 cm^{-1}) can be confidently attributed to the influence of different sections of the repeat unit of PPTA as shown below:

This conclusion can be demonstrated most clearly by adding the spectra of the two model compounds, as shown in Figure 16. Although the absolute intensities of this composite spectrum and Kevlar[R] spectrum are different, there is no doubt that the overall contour and width of the bands observed in Kevlar[R] fiber are well reproduced by the sum of the two spectra.

III.4.2 Modulus Calculation

As mentioned earlier, the significant interest shown in PPTA is due to its extremely high modulus and strength. However, because of the complexity of its morphology, the macroscopic tensile modulus may be lower than the ultimate modulus. Therefore, a reliable estimate will be quite important. Several attempts have been made using various force fields suitable for the individual components of the PPTA structures [102,103]. The ultimate elastic modulus of PPTA in the direction of the chain axis is first calculated by a method described by Treloar [102] using the force constants associated with our analysis. In this calculation, the PPTA chain is assumed to lie in a plane so that there will be no contribution from torsional deformation of the chain to the

elastic modulus, although PPTA actually exists in a non-planar configuration with a dihedral angle of $\pm30^{\circ}$ between the phenyl ring and the amide group. For simplicity, the calculation of the overall strain of a polymer chain was carried out in three parts: bond and valence angle deformation of the repeat unit excluding the benzene ring, and the overall deformation of the benzene ring itself. Therefore, the combined length of increment, ΔL, per unit applied force, F, $\frac{\Delta L}{F}$, is

$$\frac{\Delta L}{F} = \frac{\Delta L_{BS}}{F} + \frac{\Delta L_{VA}}{F} + \frac{\Delta L_{BR}}{F}$$

where ΔL_{BS}, ΔL_{VA}, and ΔL_{BR} are the length increments due to the bond deformation, valence angle deformation, and benzene ring deformation of a repeat unit, respectively. The modulus, E, is then calculated from the following equation:

$$E = \frac{(F/A)}{(\Delta L/L)}$$

where A is the cross-sectional area and L is the repeat unit length of a chain. A cross-sectional area of 20.38 $\mathring{A}^2$ and repeat unit length of 12.89 $\mathring{A}$ have been taken from the X-ray diffraction studies [22]. The ultimate tensile modulus of PPTA is calculated to be 184 GPa.

Of the total deformation of a repeat unit, 28% and 38% are due to bond stretching and valence angle deformation excluding benzene rings, and 34% is due to the benzene ring deformation. Although this modulus

value is higher than the observed macroscopic modulus of PPTA of 128 GPa [106], it is still less than the elastic modulus in the crystalline region, which was found to be 200 GPa [107]. This low value of the calculated tensile modulus is probably due to the intrinsic discrepancies in this calculation method, including the planarity assumption and the complete neglect of cross terms of force constants ,interaction force constants).

In order to overcome this difficulty in incorporating cross interaction terms, the modulus of a polymer chain can be also obtained from the frequency of the longitudinal acoustic mode (LAM) through the following relation:

$$\nu = \frac{1}{2cL}\sqrt{\frac{E}{\rho}}$$

where ν is the LAM frequency, L is the chain length, c is the speed of light, and ρ is the density of the polymer. For a real polymer, L is too long for normal coordinate analysis to calculate the LAM frequency directly. Therefore, we have to utilize the symmetry of an infinite polymer chain to get the dispersion curve of this LAM vibration. The slope of this dispersion curve at the zone center (k = 0) is proportional to the modulus. In this way, we can fully use our force constants deduced from the spectra and at the same time take the non-planar chain conformation into consideration.

TABLE 13

Results of LAM Calculation for PPTA

Vibrations with Phase Difference ϕ	Frequencies of LAM
4	3.6
5	4.6
10	9.1

The dispersion curve is obtained by calculating the LAM frequency of an infinitely long PPTA chain at various phase angles. The result is given in Table 13. Using the density of 1.50 g/cm^{-3} [108], we then obtained the modulus of 241 GPa. This value is higher than those obtained by Tashiro et al. [43] and by Fielding-Russell [103]. In their calculation, force constants that have been transferred from similar chemical structures were used. However, these values were refined using a set of coordinates containing redundancies, making them less reliable. Our force constants are transferred from the model compounds and refined for non-redundant coordinates and should be more reliable. However, this modulus calculation is only applicable for an isolated polymer chain. In a real polymer, the chain would form strong hydrogen bonds with adjacent chains in the crystal. In general, these intermolecular interactions would increase the modulus even further.

III.5   CONCLUSION

The vibrational spectra of poly(p-phenyleneterephthalamide) has been analyzed using normal coordinate analysis. The structure used is identical to the one obtained by the X-ray diffraction method and all the internal coordinates have been defined as was done previously in the analysis of the model compound, benzanilide. In order to take advantage of the well-defined force field developed for the benzene ring, the amide group and benzanilide, a specific set of non-redundant symmetry

coordinates was used in our normal coordinate analysis. Even though no refinement was carried out in the present analysis, satisfactory assignments were made for the observed bands in the regions above 900 cm-1. The mostly delocalized vibrations observed in the lower frequency regions were not analyzed. Because of the chemical and physical differences of the two benzene rings and amide groups within each translational repeat of PPTA, we expected and calculated two nearly degenerated vibrations of the mostly delocalized vibrations in the region studied. Since two model compounds representative of each unit are available, it was extremely interesting to compare the individual spectra and their sum to the infrared spectrum obtained for PPTA. Initially we were very suprised by the poorly defined spectroscopic features found for PPTA, considering that all previous analysis have suggested that the fiber sample is essentially 100% crystalline. Guided by our calculations and the comparison between the spectra found for the two model compounds to PPTA, virtually all the broad features found for the polymer were satisfactorily explained. Our present analysis shows it would be misleading to simply use the change in frequency of a broad contour to deduce conformational changes due to the application of external stresses, or, in fact, for other microstructural characterization purposes.

Given the satisfactory calculated results obtained, we have estimated the ultimate tensile modulus by two particular techniques. In the first estimate, we have taken only the diagonal force constants used in this analysis and simplified polymer geometry, and obtained a value

of 184 GPa using Treloar's method. However, a much more satisfactory

analysis is available by using the dispersion curve associated with the

longitudinal vibration of PPTA. The modulus obtained by this method is

241 GPa. This value is based on a well characterized structure and the

complete set of force constants developed independently in this chapter.

C H A P T E R   IV

SPECTROSCOPIC-MECHANICAL ANALYSIS OF THE STRAIN DISTRIBUTION
IN A MODEL COMPOSITE

IV.1   <u>INTRODUCTION</u>

It has been established that the incorporation of fibers of high modulus and strength such as PPTA and carbon fibers in a polymer matrix can significantly improve the overall mechanical properties of composites [46,47]. A cross-section of a basic unit of composite is shown schematically in Figure 17. For a given fiber and matrix, the overall enhancement of the mechanical properties is particularly sensitive to the interface/interphase properties. There have been many studies, both experimental and theoretical, to better understand the composite properties. However, the theoretical analysis of the stress distribution in short fiber reinforced composites is difficult because of the discontinuities at the fiber ends, non-uniform fiber distributions, lack of understanding of the interface, and most importantly due to the limited experimental data available to verify these theories.

Many experimental studies have been carried out to test some of the predictions of these theories. The experimental techniques used are either a photoelastic technique [62,63,109] that measures the stress distributions only in the matrix or macroscopic mechanical testing that

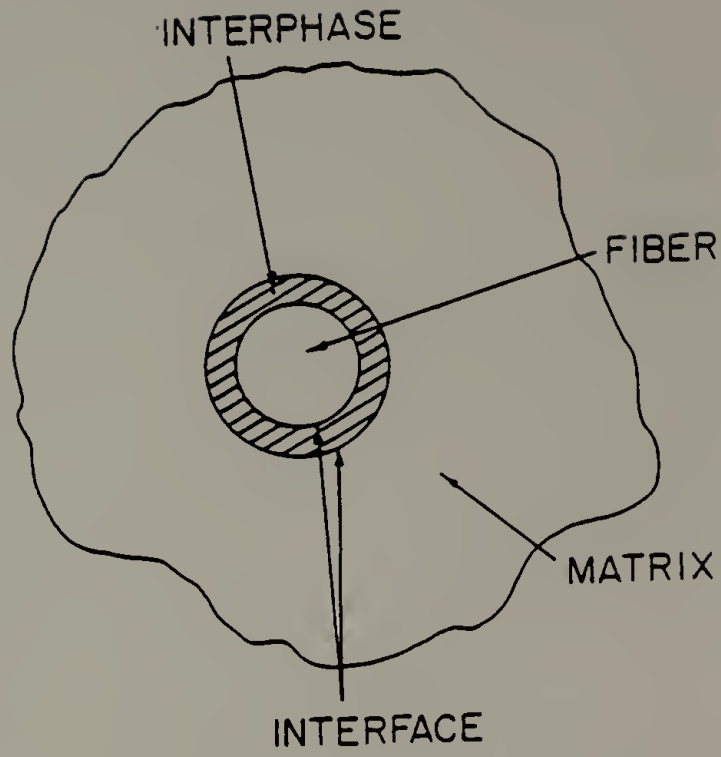Figure 17.   Schematic diagram of a cross-section of a model composite.

Figure 17.

measures macroscopic composite properties, particularly at the failure [110]. However, these techniques are indirect ways of evaluating the interfacial bonding strength or the stress transfer efficiency. In order to determine the stress level in the fiber from these techniques, relationships formulated from the theories which contain many assumptions must be used. Although these experimental techniques have provided useful information, there are still many fundamental disagreements with the theoretical results, in particular near the fiber ends where large stress concentrations exist. By measuring the stress level along the fiber axis as a function of the external load, the stress transfer efficiency of the interphase and the matrix can be evaluated directly and quantitatively. However, a technique with sufficient spacial resolution and sensitivity has not been available to directly analyze the changes of fibers in a composite. This type of technique would be ideal for future studies of composites since it would provide currently unavailable information which would be a perfect complement to a photoelastic technique. These two techniques could then determine the stress distributions of the whole composite.

Based on the unique experiment carried out by Galiotis et al. [111], we designed a series of spectroscopic-mechanical experiments to study the fiber deformation in a composite. This technique can explicitly determine the axial surface strain distribution in the reinforcement fiber, in this case polydiacetylene fiber, as a function of the applied composite strain.

At first, PPTA was chosen as a reinforcement fiber, since it is used commercially and its vibrational charateristics have been completely analyzed in Chapter III. But, because of the complexity of the spectrum, the presence of the amorphose phase [20] and the small stress induced spectroscopic changes (see Figure 18), the experiment was very difficult to do. Since we were interested not in the numerical values associated with the specific composite but in the fundamental understanding of the reinforcement mechanism of the anisotropic fiber in composites, we decided to use polydiacetylene fibers as a model for the fiber.

Although this polydiacetylene single crystal fiber cannot be considered as a commercially feasible reinforcement fiber due to its low modulus, its geometry and well-defined microstructure make it useful in the study of model composites. Since Raman spectra can be obtained easily from the embedded polydiacetylene fibers through a transparent matrix due to the resonance Raman effect of the fiber and because the backbone vibrations are extremely sensitive to the strain applied to the chain axis, each of the fiber acts as a strain gauge. Therefore, the surface strain distribution in the fiber can be directly measured from the strain induced frequency changes of this fiber with a Raman spectrometer. The development of this technique and its application to the study of the deformation behavior of an anisotropic fiber in composite under tension is presented in this chapter.

Figure 18. Raman spectra of PPTA fiber as a function of axial
deformation. (a) unstrained, (b) 2% axial tensile strain.
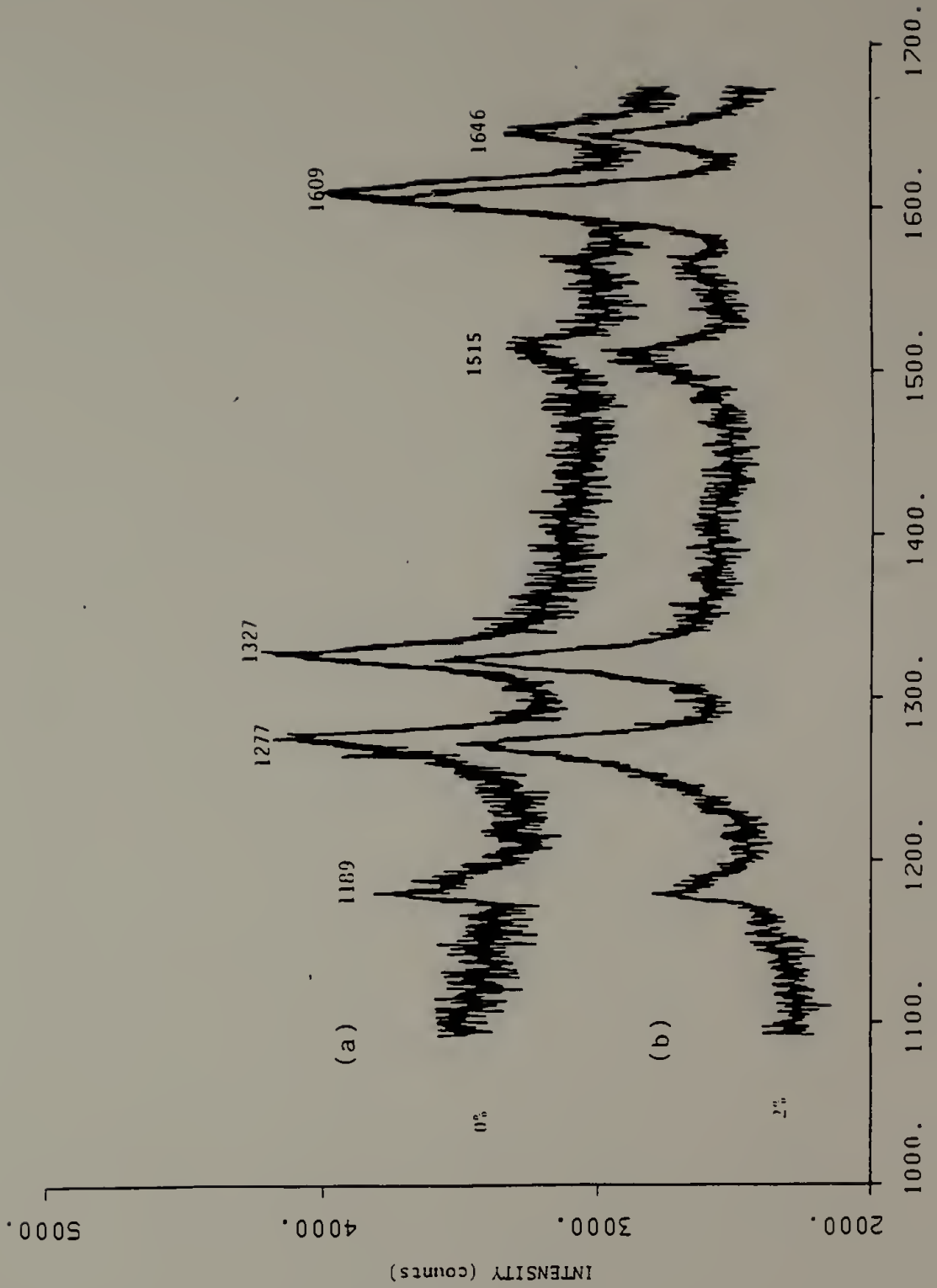(from C. Chang and S.L. Hsu, ref. 38)

Figure 18.

IV.2   <u>EXPERIMENTAL</u>

This section contains a development of the technique for directly probing the deformation behavior of the fiber embedded in a polymer matrix. The technique must have fine spacial resolution in order to examine these fibers, whose effective diameters are typically in the range of ~10-50 μm. Also, the technique must be sensitive selectively to the fiber alone so that the interference of the matrix in the data can be minimized. Finally, the stress induced changes must be as large as possible to determine the stress distributions in detail. In this experiment, polydiacetylene single crystal fiber embedded in a clear epoxy matrix was chosen as a model composite. The unique properties of polydiacetylene and the epoxy matrix and the construction of the mechanical stretcher are described in this section.

IV.2.1   Polydiacetylene

The structure of polydiacetylene is shown in Figure 19(a). It is presently available with a number of side chains, labelled R in this figure [112]. This polymer has extended π-electron delocalization along the backbone. Our sample, poly(2,4-hexadiyne-1,6-diol bisphenylurethane) (P-HDU) has $-(CH_2OCONHC_6H_5)$ as both side chains in a repeat unit. P-HDU, like many other polydiacetylene fibers with different side groups, has unique spectroscopic and mechanical

properties which allow it to be used as a strain gauge that can be readily measured with Raman spectroscopy.

Although the reactions of diacetylene were originally reported over a century ago [113], Wegner [114-116] was the first to prepare a macroscopic single crystal of polydiacetylene. The synthesis of P-HDU involves growing of a diacetylene monomer single crystal in the form of a needle from a dilute solution of dioxane and water mixture. This monomer crystal is directly polymerized topochemically in the solid-state into a polymer crystal of the same shape. This solid-state polymerization can be initiated by either heat or UV radiation. Within the lattice of the monomer crystal, the individual molecules are aligned in a ladder-like fashion by either hydrogen bonds or van der Waals interactions between the substituents of adjacent molecules. These monomers are polymerized by successive tilting and subsequent 1,4-addition reaction at the conjugated triple bond, resulting in a fully conjugated backbone. The general reaction scheme for the solid-state polymerization of diacetylene is shown in Figure 19(b). The X-ray diffraction study of P-HDU indicated that one-half of the dioxane molecule per repeat unit is incorporated into the lattice during the crystal growth [115]. P-HDU can be grown to form perfectly oriented, defect-free macroscopic single crystals of 1-2 cm long with a rectangular cross-section whose effective diameter is about 30-60 μm. Thus its aspect ratio ranges from 170 to 700. The chain axis is oriented parallel to the the fiber axis.

Figure 19. (a) Schematic structure of polydiacetylene;
(b) General reaction scheme of solid-state topochemical
polymerization of diacetylene.
(from H. Bassler, ref. 112)

(a)

(b)

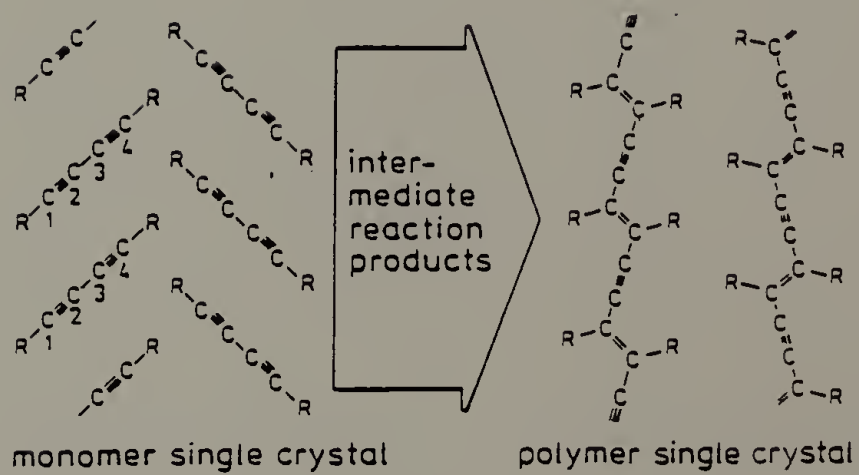monomer single crystal → intermediate reaction products → polymer single crystal
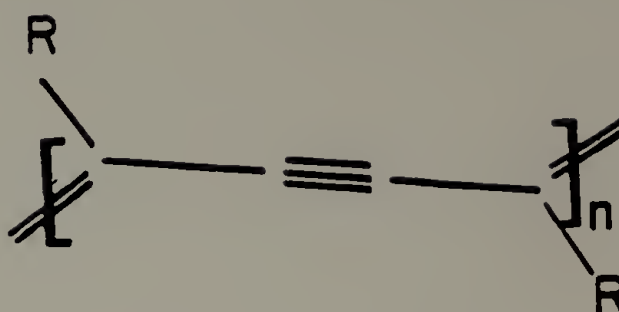
Figure 19.

Baughman et al. [117] characterized the mechanical and spectroscopic properties of P-HDU single crystal fibers. They found that these P-HDU fibers have a high degree of perfection with an average modulus of 45 GPa and a maximum observed ultimate tensile strength of 1.7 GPa. Low values of modulus for P-HDU, despite being a defect-free, highly oriented single crystal fiber, are attributed to the large side group which increases the cross-sectional area of the fiber. For example, the cross-sectional area of P-HDU chain is 97.2 Å^2 compared to 18.4 Å^2 for polyethylene.

They also showed that Raman active vibrational bands of P-HDU associated with its backbone are sensitive to the applied axial strain [118]. As shown in Figure 20, the double and triple bond stretching vibration frequencies shift by 8 cm^{-1} and 21 cm^{-1} respectively per percent axial strain. Similar behavior is found in other polydiacetylene single crystal fibers [112,119,120]. Both they and others explained this behavior in terms of the anharmonicity of the force constants for the bonds in the chain backbone [118,119]. Being a single crystal fiber, the externally applied stress or strain should be transmitted uniformly to each individual chains unlike the two phase, crystalline and amorphous, systems. Therefore, with P-HDU, the direct comparisons between molecular and macroscopic deformations should be possible from frequency shifts measurements as a function of the external load.

A resonance Raman scattering experiment is any Raman scattering experiment which employs incident radiation frequency near the

electronic absorption of the material. The Raman scattering process involves the inelastic scattering of photons. This process involves a change of the vibrational states of the material with an accompanying exchange of energy with the incident radiation field. The frequency shift for the scattered light is known as the Raman frequency and is independent of the incident frequency in the normal Raman process. Raman intensity is proportional to the polarizability, P_{nm}, where

$$P_{nm} = \frac{1}{h} \sum \left(\frac{M_{nr} M_{rm}}{\nu_{rn} - \nu_o + i\delta_r} + \frac{M_{nr} M_{rm}}{\nu_{rm} + \nu_o + i\delta_r} \right) E$$

where h is Planck's constant, r denotes any intermediate state of the complete set belonging to the unperturbed molecules, ν_{rn} and ν_{rm} are the frequencies corresponding to the differences between the states denoted by the subscripts, M_{rn} and M_{rm} are the corresponding transition moments, δ_r is the damping constant of r, and ν_o and E are the frequency and the electric vector of the incident radiation [121]. The resonance Raman scattering process is one in which the incident photon has a frequency ν_o, near the electronic absorption maximum of the matter, so that $n_o = \nu_{rm}$. This results in the denominator of the first term in the right hand side of eq(1) to be near zero so that the intensity increases drastically up to 10^5 -10^6 times the normal Raman intensity resulting in extremely high signal to noise ratio. Also, frequency shifts in the resonance Raman process depend strongly on the incident frequency.

Figure 20. Strain induced frequency change of C=C and C≡C stretching vibrations (V.K. Mitra, W.M. Risen, and R.H. Baughman, ref. 118)
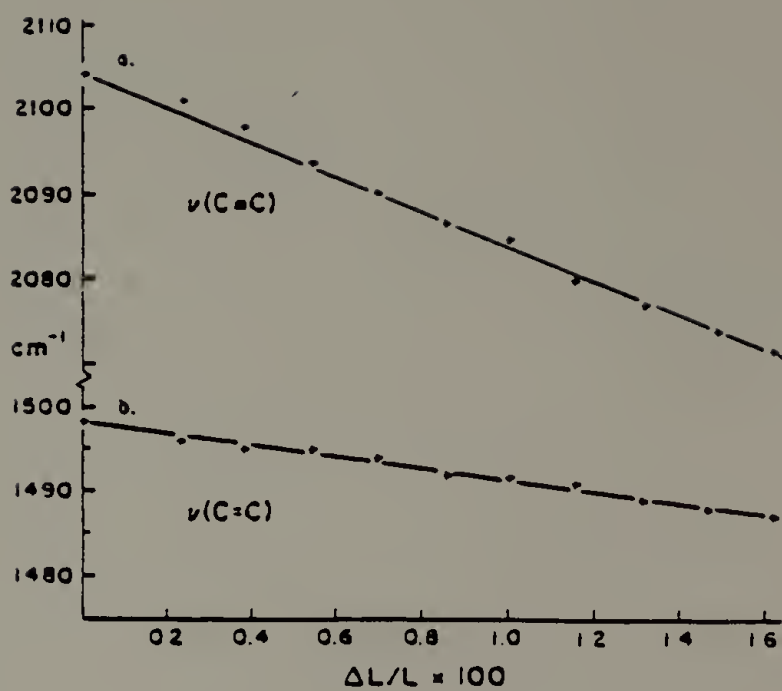
Figure 20.

The absorption spectrum of polydiacetylene seems to be dominated by a strong absorption at approximately 4020 cm^{-1} (2eV) [122]. This absorption is the result of an electronic excitation of the polymer backbone and, in particular, the π-electron system of the conjugated polymer backbone. Therefore, only chain vibrational modes closely coupled to the π-electron system of the polymer backbone will be resonance enhanced. Thus, despite the presence of complex side groups and the epoxy resin, the Raman spectrometer is capable of probing only the structure of the backbone of polydiacetylene without any interference from other vibrations due to side groups and epoxy resin. This is demonstrated by the simplicity of the resonance Raman spectra of P-HDU fiber alone and P-HDU fiber embedded in a clear epoxy resin as shown in Figure 21. The vibrational analysis of isolated polydiacetylene chain has been reported by Lewis and Batchelder [123] using a simple point mass model.

These Raman spectra were obtained with a Jobin-Yvon HG.2S Raman spectrometer using a slit setting of 4 by 200 µm giving 2 cm^{-1} linewidth at 500 nm. Incident radiation with wavelengths of both 514.5 nm from Argon ion laser and 632.8 nm from Helium-Neon laser were used. Neutral density filters were used to reduce the source power to minimize thermal degradation of polydiacetylene.

Figure 21. Raman spectra of solid-state polymerized P-HDU single crystal fiber. (a) fiber alone, (b) fiber embedded in EPON828 cured with DTA. Incident radiation 632.8 nm; 2 cm^{-1} bandpass at 500 nm; laser power, 7 mW.
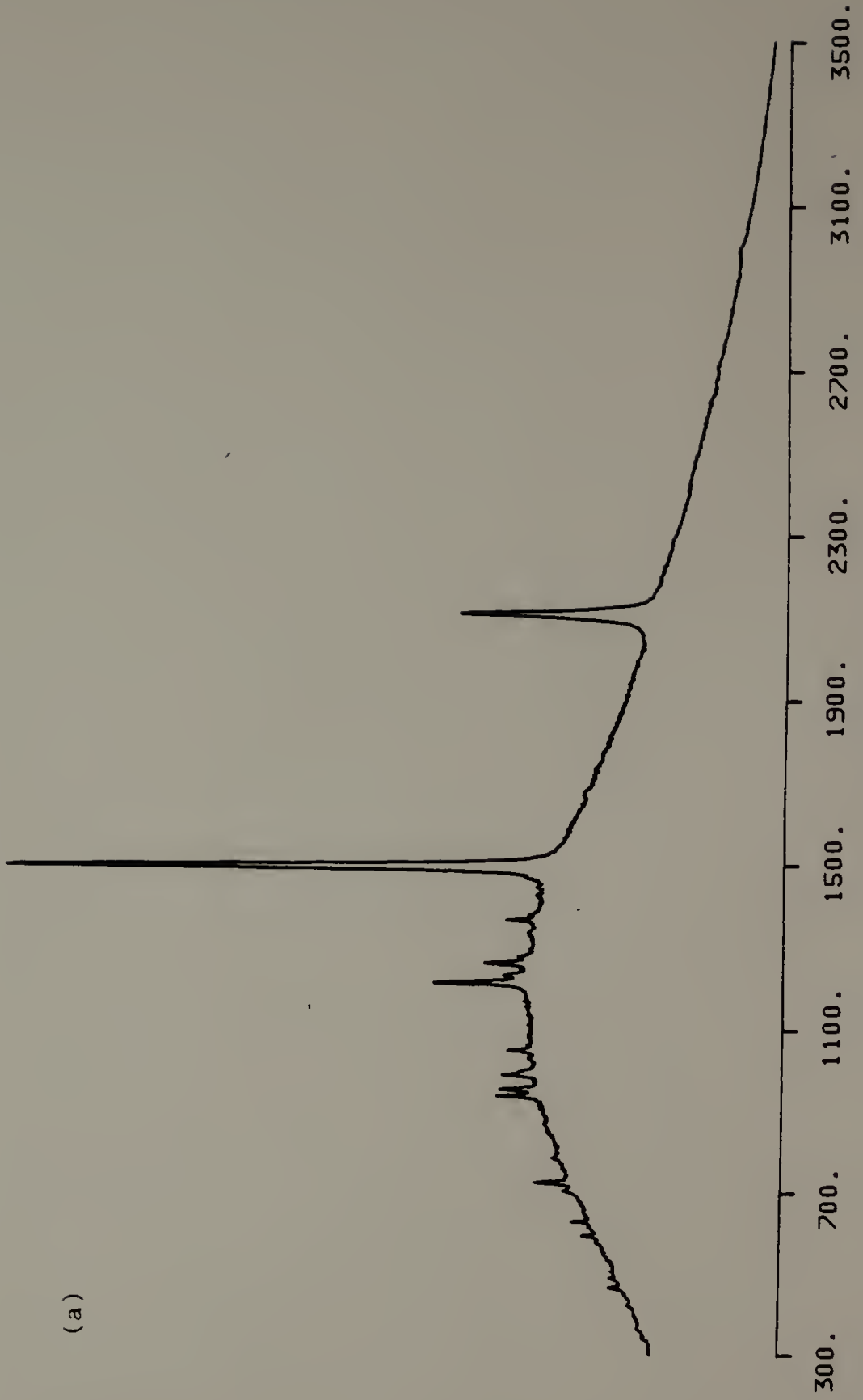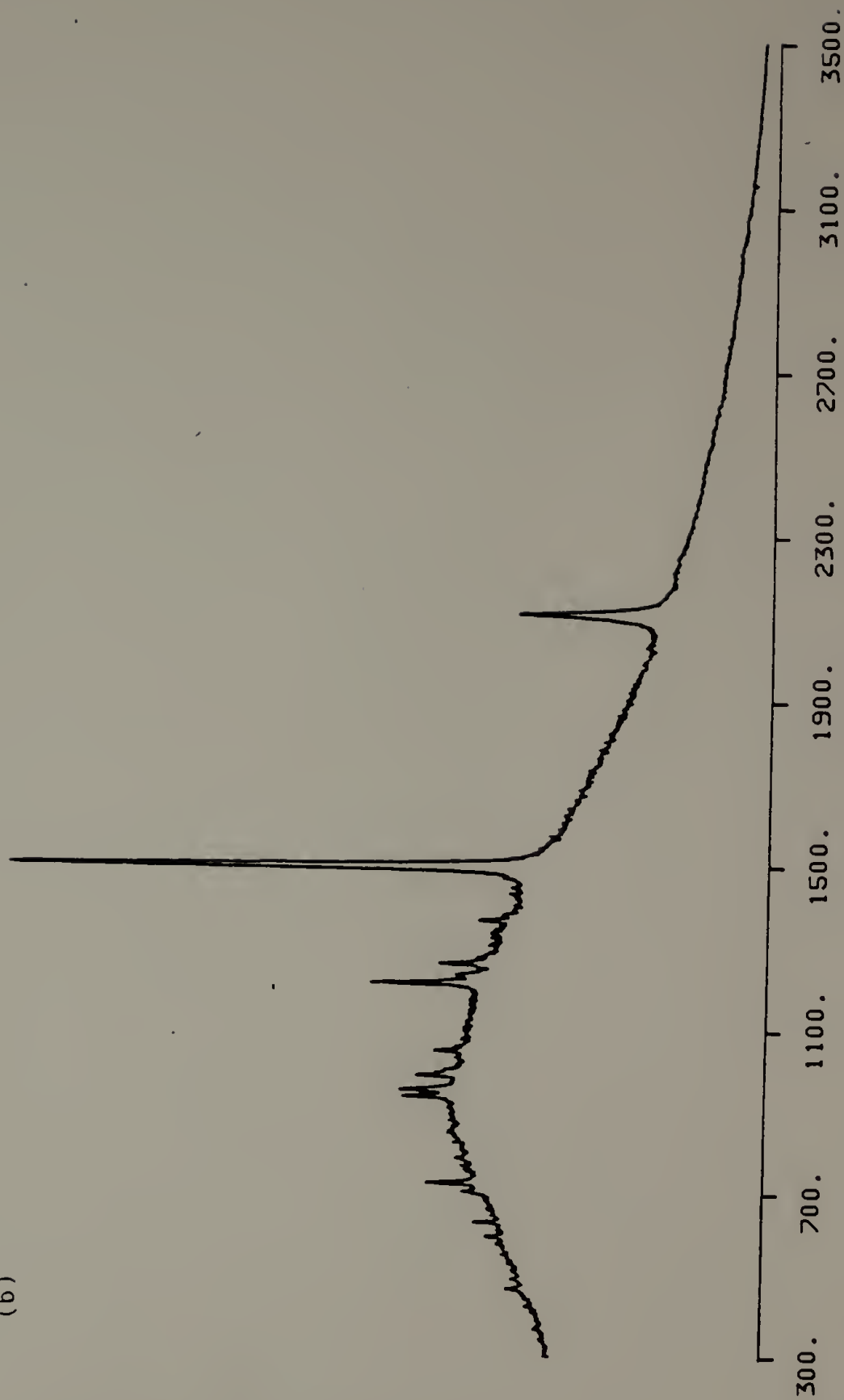
(a)

WAVENUMBERS (cm-1)

Figure 21.

(b)

WAVENUMBERS (cm-1)

Figure 21.

IV.2.2   Epoxy Resin

A dog-bone shaped model composite of single P-HDU fiber embedded in epoxy is made according to ASTM D-638 [124]. The epoxy resin is first degassed in a vacuum oven in order to remove all the air bubbles trapped in the resin. Sometimes, it is heated to facilitate degassing. Then, the hardner is added and mixed carefully in order to minimize the bubble formation. The mixture is degassed again before pouring into the mold. This dog-bone tensile specimen is made in two steps. First, one-half of the mold, which is made of Teflon^R, is filled with the epoxy and partially cured so that P-HDU fiber can be positioned in the middle of the sample. After the mold is completely filled and covered with a Mylar sheet, the composite is cured at specified conditions.

One of the most critical aspects of this model composite study using Raman spectroscopy was the determination of the matrix to be used. In order to minimize absorptions of incident laser beam and scattered Raman light by the matrix, the matrix must be transparent. Furthermore, since most of the structural changes are interpreted from the changes observed in the backbone vibrations of resonance enhanced Raman spectra of the fiber, fluorescent background must be minimized, if not totally eliminated. Epoxy, unsaturated polyester, and polyurethane are possible candidates as a matrix material. After a number of experiments, epoxy was chosen because, in addition to meeting the above requirements, it is one of the most widely used resin for high performance composites. Also, a wide range of matrix mechanical properties can be readily

obtained by mixing two epoxies of different properties or by changing the curing agents or conditions. For example, epoxy properties are strong functions of the epoxy/curing agent ratio and curing conditions such as temperature and time [125-128].

In this experiment, Dow's DER 736 and Shell's EPON 825 and EPON 828 are used with diethylenetriamine (DTA) as a curing agent. All samples have been cured with stoichiometric amounts of curing agent, i.e. two moles of DTA to five moles of epoxy resin. DER 736 is a clear resin with a relatively flexible aliphatic carbon backbone that is based on diglycidyl ether of polypropylene glycol [129]. Both EPON 825 and EPON 828 are difunctional epoxies that are based on diglycidyl ether of bisphenol-A [130]. They usually have greater thermal stabilities and higher mechanical properties than aliphatic based epoxy. For curing agents, two-component curing agents such as anhydrides and accelerators tend to have strong fluorescent backgrounds so that it is difficult to obtain a good Raman spectra of P-HDU with 514.5 nm incident radiation. After a number of studies, DTA is chosen because of its clarity, low fluorescence, low viscosity at room temperature, and high reactivity for curing at low temperature. The last condition is an important factor for P-HDU because this fiber starts to degrade near 165°C [131]. So it is important that the curing agent be reactive enough at low temperature so that the exothermic reactions of curing does not raise the resin temperature above 165°C near the fiber, yet still allows the curing to be completed in a reasonable time. The chemical structures of epoxy resins and the curing agent are shown in Figure 22.
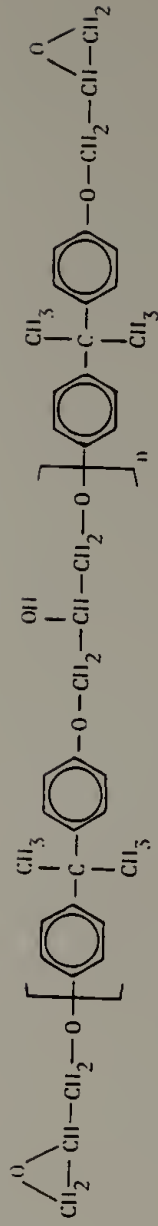
Figure 22. Chemical structures of epoxy resins and hardner.
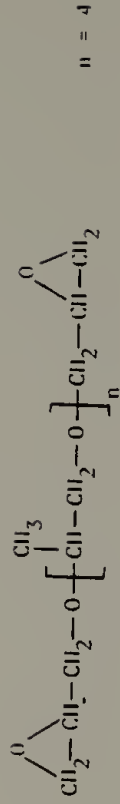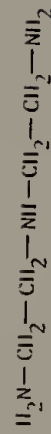
Figure 22.

IV.2.3   Mechanical Stretcher and Electronics

The mechanical stretcher, shown schematically in Figure 23, is built for the deformation studies of model composites in conjunction with the Raman spectroscopic experiment. This stretcher is built to fit into the sample chamber of a Jobin-Yvon HG.2S spectrometer for 90° scattering geometry. It is also small enough to fit into the purge box sampling chamber of IBM FTIR Model 98. The stretcher is vertically placed on the x,y,z translation state to aid sample alignment and to allow studies of the deformation as a function of position in the fiber. Both tensile and compressive deformation of samples are possible. For tensile deformation experiments, a tensile specimen is placed between sample mounts equipped with a guide pin to prevent the sample from slipping. Both sample mounts are attached to a pair of stabilization rods to eliminate rotation.

The deformation is done by the stepping motor connected to the sample mount with a lead screw. A Superior Electric (200 steps per revolution) DC stepping motor (model MO63) is used with a ten pitch-per-inch lead screw. Therefore, each step of the stepping motor corresponds to 0.0005 inch displacement. The deformation can be accurately measured by counting the number of steps the stepping motor moves. It is also equipped with the standard Lanchester damper tuned to its natural frequency in order to eliminate any torsional vibrations or resonance vibrations when operating at its natural frequencies. The stepping motor is controlled with the stepping motor controller with a self

contained microprocessor (Advanced Micro Systems Inc. Model SM-2) [132].
This controller has the ability to perform over 50 different
pre-programmed commands. It also has a speed range from five steps per
minutes to over 13,000 steps per second. Initial velocity, ramp slope,
and ramp length are all programmable so that it is easy to perform
various types of deformations.

The other sample mount is connected to the load cell (Data
Instruments JP200, rated at 200 pounds) in order to measure the load
values. The analog output from the load cell is first conditioned with
a signal conditioning module (Analog Devices Model 2B31J) in order to
amplify the small load cell signal to a ± 10V range and to remove any
noise. This conditioned signal is then digitized with a 12-bit analog-
to-digital converter (Analog Devices Model AD572). The schematic
diagram of the control electronics is shown in Figure 24. This
digitized load cell value is accessible through the parallel I/O ports
of California Computer Systems' (CCS) Model 2200 computer. This
computer also controls the stepping motor controller. We have written a
Pascal program on the CCS computer to control the deformation of the
sample and to collect corresponding load values as a function of time
simultaneously. This allows the measurement of stress-strain behavior
of the sample. The source code of this program is listed in Appendix B.

Figure 23.   Schematic diagram of the mechanical stretcher.

Figure 23.

SCATTERED
RADIATION

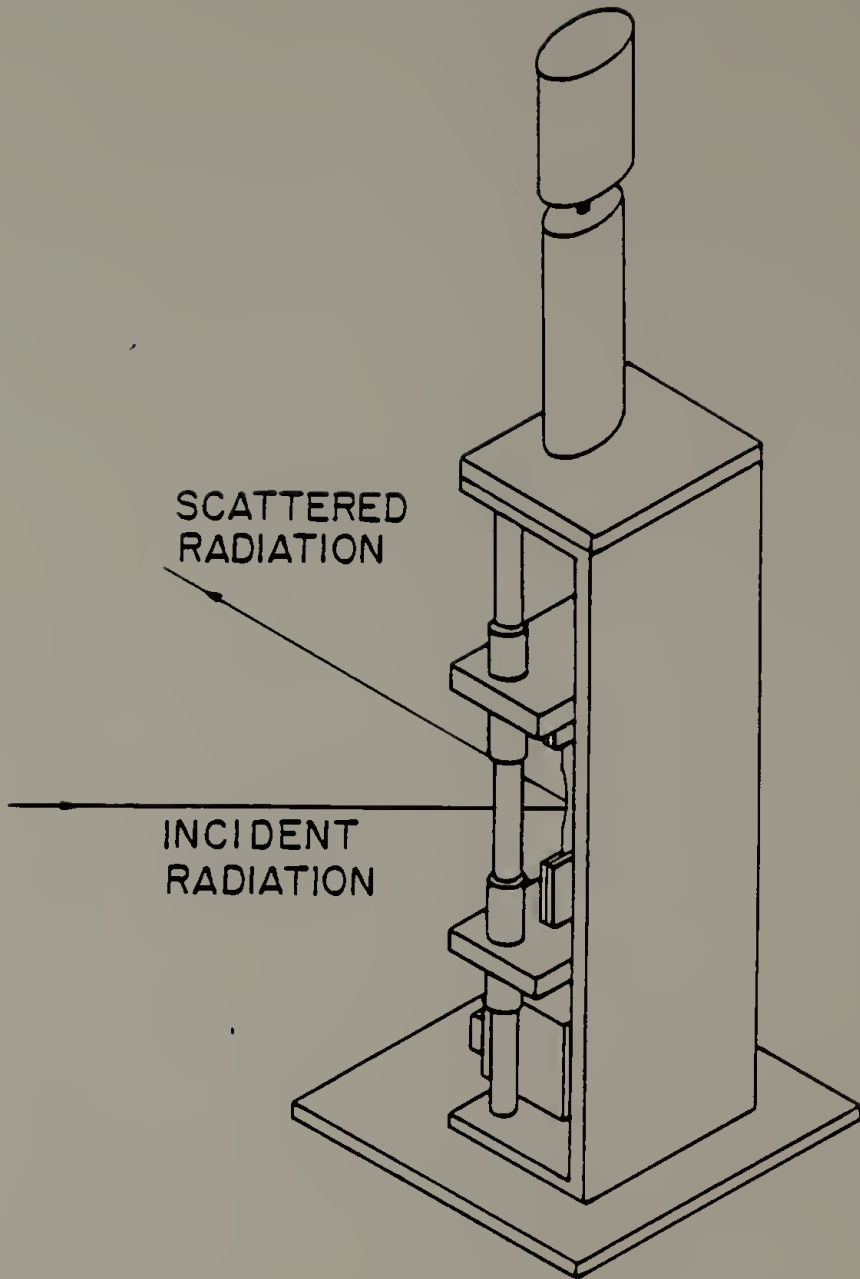INCIDENT
RADIATION

Figure 23.

Figure 24.   Schematic diagram of the mechanical stretcher control electronics and the interface to CCS computer.
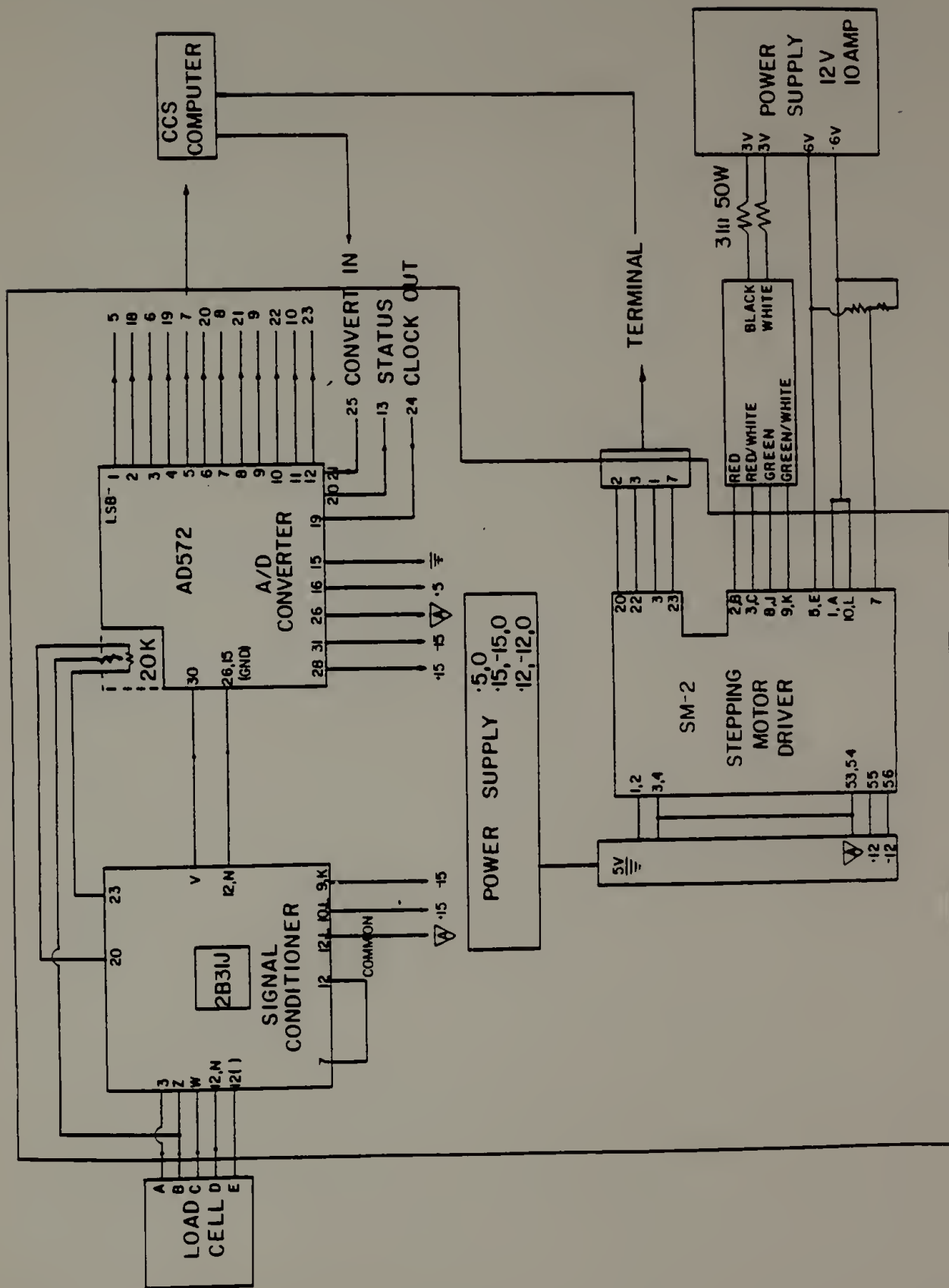
Figure 24.

IV.3   <u>RESULTS AND DISCUSSION</u>

Figure 25 shows the changes in the frequency of the C≡C stretching vibration along the fiber when the model composite is subjected to tensile deformation parallel to the fiber direction. The frequency decreases significantly from 2106 cm^{-1} near the fiber end to 2100 cm^{-1} in the middle of the fiber for 2% axial deformation of the sample. The C≡C stretching frequency of P-HDU fiber alone is 2106 cm^{-1}. By using the established linear relationship of 21 cm^{-1}/% axial strain of P-HDU [118], we can interpret the axial strain of the embedded fiber from the vibrational frequency of the C≡C stretching vibration. Since the penetration depth of the Raman scattering is about 10 nm [133], it is only the surface strain that is being measured. The measured equivalent axial surface strain of the fiber is very small near the fiber end and increases away from the fiber ends until the plateau value is reached, as assumed and predicted by earlier analysis [53-56]. Because of highly anisotropic nature of fiber and its low shear modulus, the axial deformation will not be constant across the cross-section of fiber. Additional information, such as shear modulus and Poissons ratio, is needed for the analysis of strain distribution in transverse direction. The length over which the fiber strain increases is equivalent to half the critical length. The fiber length must be greater than this critical length in order for its superior mechanical properties to be fully utilized. This asymptotic value of the fiber strain or the critical length is a direct measure of the stress transfer efficiency of

Figure 25. Frequency variation of the C≡C stretching vibration observed
for the model composite as a function of position along the fiber.
Left: the various Raman spectra obtained, Right: frequency variation
(calculated effective axial strain) as a function of distance away from
the fiber end. Laser excitation, 514.5 nm; laser power, 7 mW; bandpass
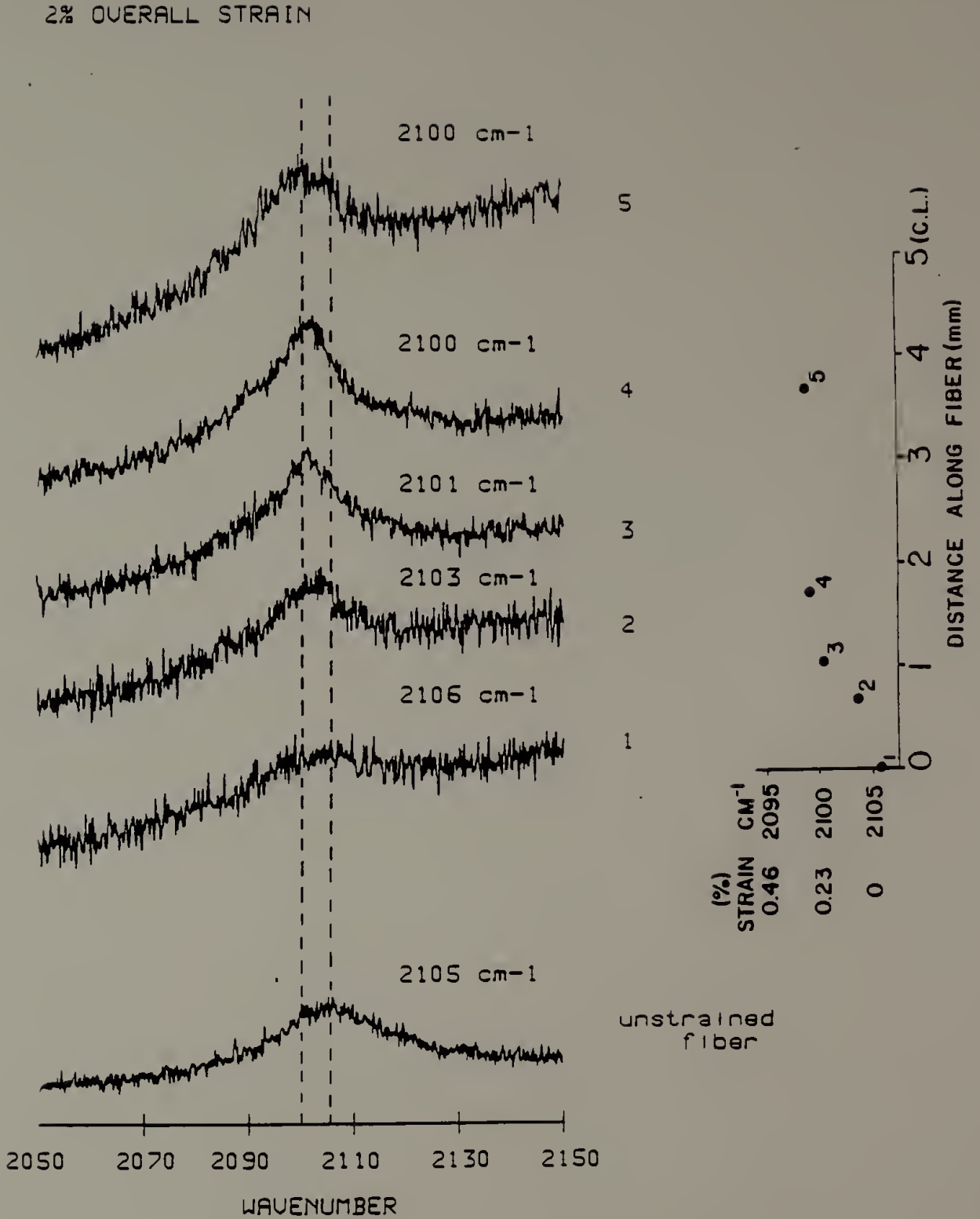2 cm^{-1} at 500 nm; matrix is EPON825 cured with DTA.

Figure 25.

Figure 26. Frequency variation of the C≡C stretching vibration along the fiber embedded in epoxy subjected to different tensile strains. (o) 1.0% composite strain; (●) 2.5% composite strain; 514.5 nm excitation wavelength; bandpass 2 cm at 500 nm.
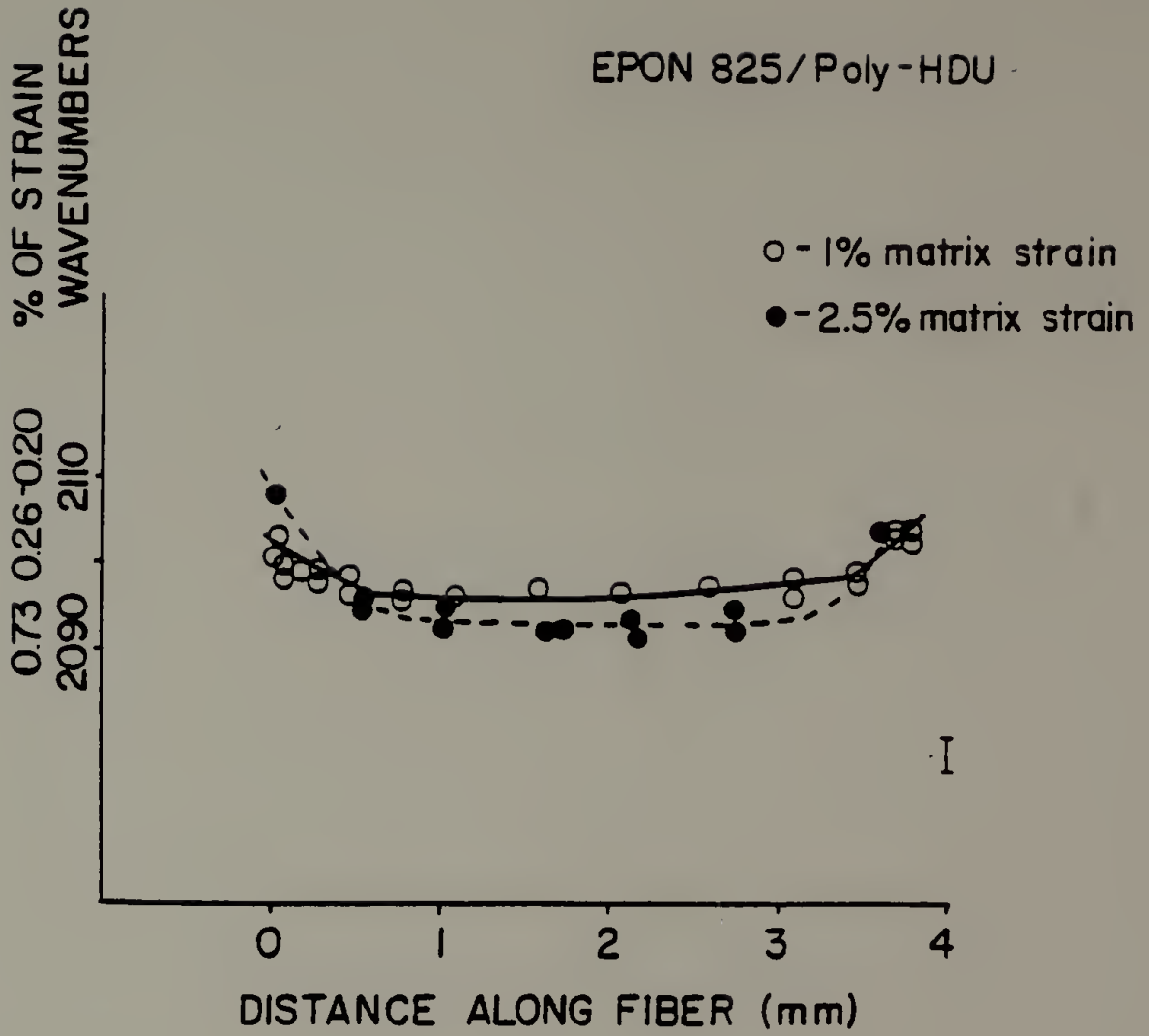
Figure 26.

the matrix and the interphase. The difference between the applied macroscopic strain and the measured fiber strain is maybe caused by the mechanical stretcher system compliance.

The vibrational frequency measured is an average value from the sample scattering cross-section of about 50 μm diameter. Thus, this type of data, as shown in Figure 25, qualitatively supports the hypothesis that the load at the fiber ends is zero or nearly zero. In order to study the strain distribution near the fiber ends, a smaller scattering cross-section is needed. This can be achieved by either changing the collection optics or, more easily, by using a Raman spectrometer equipped with a micro-sampling capability. Also, Figure 26 shows that as the applied axial strain of the composite is increased from 1% to 2.5%, the axial strain of the embedded fiber increases as well but not the same magnitude. Although details differ, the overall stress on the fiber sample is consistent with theoretical expectations, illustrating that this essentially microscopic technique can be used to understand what is actually a macroscopic problem and to provide additional data for further theoretical analysis.

Since this epoxy matrix is a glassy material at room temperature and Raman spectroscopy is a slow technique, we were concerned with the stress relaxation during the tensile deformation. The time resolution available for this experiment, i.e. time to obtain a spectrum of the C≡C stretching frequency region, is about five minutes. The model composite was strained to 2% and held at the constant strain for 24 hours to study the effect of stress relaxation in the measurements. The result is

Figure 27. Frequency variation of the C≡C stretching vibration as a function of time at a constant composite tensile strain of 2.5% (●) fiber end, (○) middle of the fiber.
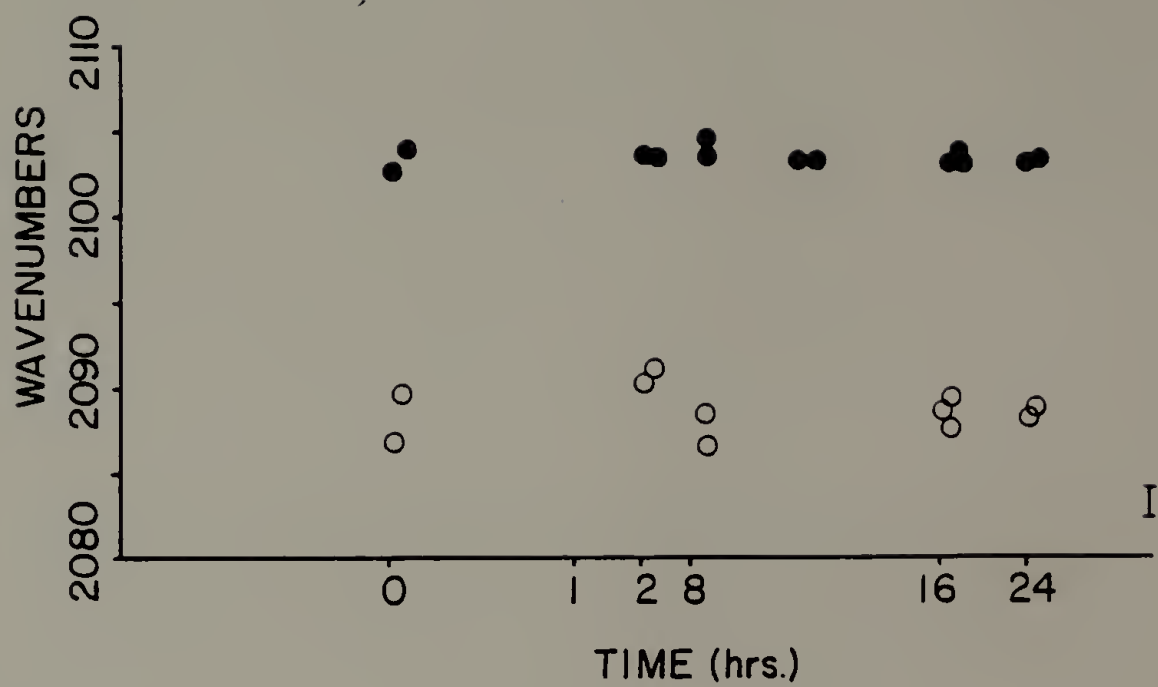
Figure 27.

shown in Figure 27. The data is obtained from both near the fiber end (dark circles) and the middle of the fiber (open circles) as a function of time. Although some scatter in the data exists, there seems to be no dependence of the measured fiber axial strain on time. This is probably because the majority of the stress relaxation occurs immediately after the load is removed since the fiber volume fraction is so low, and since it is too fast for a Raman spectrometer to measure.

The factor which limits the precision in the determination of fiber strain is associated with the uncertainty involved in measuring the position of the vibrational band. In our case, the uncertainty is approximately ± 1 cm^{-1}, which corresponds to an uncertainty of $\pm 0.05\%$ in the fiber strain. It cannot be overemphasized that, unlike most previously available techniques, this spectroscopic-mechanical technique can provide a strain distribution of the anisotropic fiber embedded in a matrix with greater spatial resolution and precision. Since both the applied external strain and the actual strain present on the fiber are measurable, the stress-transfer efficiency of the interphase can be evaluated quantitatively.

IV.4   CONCLUSION

A combination of spectroscopic-mechanical technique was developed to study the deformation behavior of a reinforcement fiber embedded in a polymer matrix directly. This was possible because of the high

frequency-strain coefficient and the resonance Raman scattering effect of a polydiacetylene single crystal fiber. The axial strain distribution in the P-HDU fiber embedded in a transparent epoxy shows that the strain near the fiber ends is nearly zero, as assumed in many composite theories. However, the assumption of perfect bonding, i.e. continuity of axial strain at the interface, does not seem to be valid in this system. Any possible stress relaxation occurs too quickly for this technique to detect so that the measured frequencies are independent of time within experimental error.

CHAPTER V

SPECTROSCOPIC ANALYSIS OF RESIDUAL STRAIN IN A MODEL COMPOSITE

V.1   INTRODUCTION

The residual stress distribution in an unstressed sample may

originate from the disparity in thermal expansion coefficients of the

matrix and the fiber when the composite is prepared at high temperature

and then allowed to cool. In addition, if composites are required to

perform over a wide temperature range, there may be stress build-up and

fatigue failures due to residual stresses as well. These residual

stresses are due to the differences in thermal expansion and

moduli between the fiber and the matrix and the volume shrinkage during

the crosslinking reactions during curing of thermoset resins or

crystallization of semicrystalline thermoplastic resins [134-136]. The

main reason for residual stress accumulation on fiber and matrix is that

each component constrains each other's thermal expansion resulting in

longitudinal, transverse, and shear residual stresses. Although

importance of these residual stresses has been realized for a long time,

understanding of the residual stresses in composite is limited. This is

because there have been only limited experimental data available, in

particular the residual stress in the embedded fiber as discussed in the

previous chapter. Most of the studies that have been reported are

usually photoelastic studies that evaluate the residual stress

distributions only in the matrix [62,63]. One of the main reason for this is the lack of the adequate techniques that can directly measure the stress distribution on the reinforcements embedded in the matrix.

In Chapter IV, we have presented a combination of resonance Raman spectroscopic-mechanical technique that has been developed in our laboratory to study the deformation behavior of a fiber embedded in epoxy subjected to tensile deformation directly using polydiacetylene fiber. It is then possible to measure the residual strain level on the embedded fiber directly as a function of temperature, curing, and many other causes utilizing polydiacetylene fiber as the reinforcement fiber and Raman spectroscopy. It is also possible to evaluate the effect of these residual stresses on the stress-transfer efficiency of the composite by subsequent deformation studies with the technique described in Chapter IV. These experimental results are then compared with the results of thermoelastic analysis to evaluate the changes in the nature of the fiber/matrix interface, such as interfacial bonding, and to determine the important structural parameters of constituents that affect the overall residual strains on composite.

In most of composites, reinforcement fibers are coated with coupling agents or sizing materials for various purposes. The coating on fibers can protect the fibers during processing, promote bonding between fiber and matrix, and improve specific properties such as electric conductivity and fatigue properties of a composite [137-140]. The interphase layer also forms naturally because the properties of the resin adjacent to the fiber is altered by the presence of the fiber.

Recently there has been studies on the possible use of the interphase layer to reduce the residual thermal stress build-up [117]. This is possible if the interphase layer has a different glass transition temperature and modulus from the matrix [83]. However, these differences in properties can cause the interphase layer to become the stress-concentration regions resulting in formation of microcracks at the interface prematurely and consequently reduced the overall composite strength [61].

This chapter contains the experimental results of curing residual strain due to volume shrinkage during crosslinking reaction and thermal residual strain due to differential thermal contractions between the fiber and the matrix on temperature changes in the polydiacetylene fiber as a function of curing and temperature since they seem to be the most common and significant causes in all composites. In addition, the effect of an interphase layer on residual strain in the fiber will be discussed.

V.2   EXPERIMENTAL

The same polydiacetylene fibers, poly(2,4-hexadiyne-1,6-diol bisphenylurethane) (P-HDU), as that used in the previous chapter are used for the residual stress experiments. They are generally 5 to 10 mm long and have a rectangular cross-section with a effective diameter of around 30 μm. Their unique properties are discussed in the section

IV.2.1. These fibers were first examined under an optical microscope to discard the damaged fibers. The same epoxy resins and the matrix preparation procedures as in chapter IV are used again here. In addition to epoxy resin, Solithane 113 and its curing agent, C113-300, from Morton Thiokol, Inc. are also used both as a matrix and as a soft-phase layer in the two-layer matrix with epoxy resins. Solithane 113 is a trade name for a polyurethane elastomer that is the product of a reaction between Castor Oil and toluenediisocyanate [141].

For residual stress experiments, rectangular bars of model composite consisted of single P-HDU fiber embedded near the middle of the epoxy matrix are used. These samples are cured at specified conditions to study the effects of curing and temperature changes separately. Generally, the model composite is pre-cured at room temperature for 6 to 12 hours so that its surface is no longer sticky. This pre-cured composite is then post-cured at various temperatures ranging from 60°C to 100°C and cooled slowly to room temperature to study the effect of post-curing on the residual stress distribution. In order to study the thermal residual stress, the sample is completely cured at 100°C for six hours. This will minimize the effect of curing strain due to post-curing during the temperature changes between 20°C to 100°C.

The post-curing temperature is limited to around 100°C due to the exothermic nature of the crosslinking reaction, since P-HDU fiber starts degrading near 165°C. The X-ray diffraction study of P-HDU indicated that one-half of dioxane molecule per repeat unit is incorporated in the

lattice [131]. This interstitial dioxane can be volatilized readily near 165°C without any chemical degradation of the polymer. However, removal of the dioxane results in a substantially different crystal structure and consequently different vibrational behavior. In order to determine the temperature limits where no irreversible changes in the crystal would take place during curing and heating experiments, P-HDU fiber was annealed at 135°C and 165°C for two hours under vacuum. The effect of annealing in the vibrational spectra is shown in Figure 28. The room temperature Raman spectra of the fiber before and after annealing at 135°C shows little change whereas the changes were considerable after annealing at 165°C. The spectroscopic features found after the removal of dioxane are represented by additional bands in the double and triple bond stretching vibrational regions.

For in situ post-curing and temperature experiment in the Raman sample chamber, Harney-Miller cell modified with heating coil around the outer jacket is used (see Figure 29) [142]. The model composite is placed in the center of an evacuated annular jacket, and cold nitrogen gas is passed through the center of the jacket. Using cold nitrogen gas and heating coil, temperature range of -150°C to 100°C can be easily achieved. The temperature is measured with a copper-constantine thermocouple placed near the sample. The temperature is accurate to ±1°C. This Harney-Miller cell is placed on the x,y,z translation stage for easy alignment.

The extent of the crosslinking reaction was studied with an IBM Model 32 FTIR spectrometer. The thin layer of the mixture of EPON 828

Figure 28.   (a) Raman spect$_\mathrm{g}$a of C=C and C≡C stretching regions of
                  P-HDU at 22 C.   Top: before annealing, Bottom: after
                  annealing at 165 C for two hours in vacuum.
             (b) Raman spect$_\mathrm{g}$a of C=C and C≡C stretching regions of
                  P-HDU at 22 C.   Top: before annealing, Bottom: after
                  annealing at 135 C for two hours in vacuum.

WAVENUMBERS (cm-1)

(a)
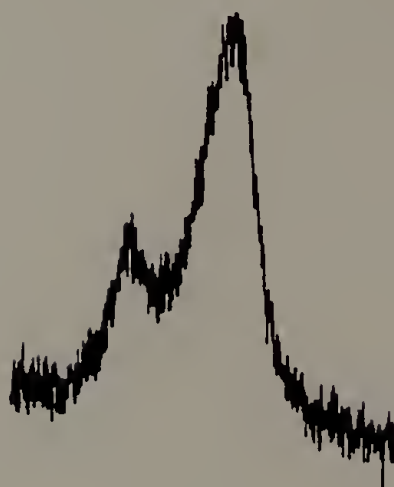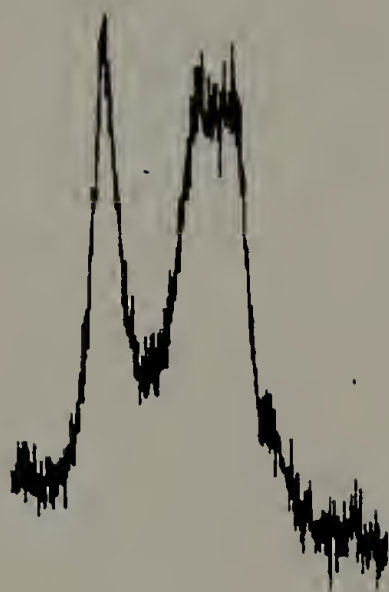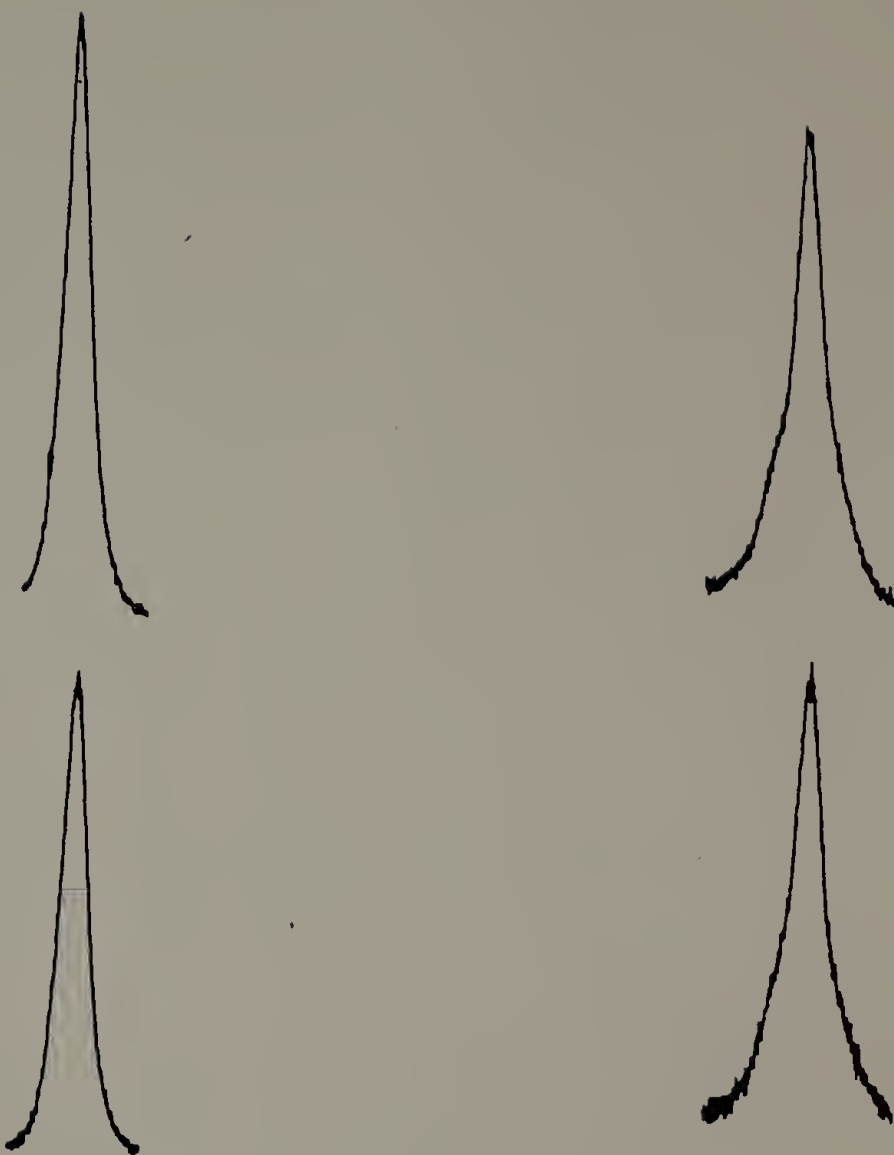

1400. 1450. 1500. 1550. 1600.
WAVENUMBERS (cm-1)

2000. 2050. 2100. 2150. 2200.
WAVENUMBERS (cm-1)

Figure 28.

(b)

1400.   1450.   1500.   1550.   1600.   2000.   2050.   2100.   2150.   2200.

WAVENUMBERS (cm-1)   WAVENUMBERS (cm-1)

Figure 28.

Figure 29.   Schematic diagram of Harney-Miller cell.
             (F.A. Miller and B.M. Harney, ref.142)
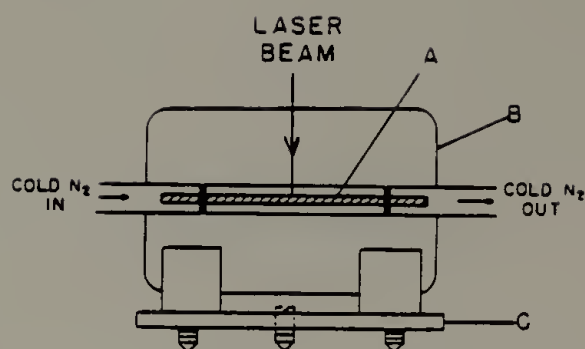
Figure 29.

and DTA is coated onto a potassium bromide disk immediately after mixing. The disk is placed in the heating cell made for the spectrometer. The temperature is controlled within $\pm 2 ^{\circ}$C. 32 scans of 2 cm^{-1} resolution spectra were signal averaged for our analysis. The spectra were taken at every five minutes for first 30 minutes and at every 10 minutes for the remaining time. Dynamic mechanical properties of the epoxy and Solithane resins were obtained using a DMTA from Polymer Laboratory Co., Inc. The flexural modulus is measured in the single beam double cantilever mode at the frequency of 1 Hertz.

The Raman spectrometer used is Jobin Yvon HG.2S spectrometer with HeNe laser (6328 A excitation wavelength). Neutral density filters were used to reduce the laser power to about 5 to 8 mW at the sample. Slit width of 200 μm was used for all spectra. This corresponds to 2 cm^{-1} bandpass at 5000 Å wavelength. The sampling cross-sectional area at the fiber is about 50 μm in diameter.

V.3   RESULTS AND DISCUSSION

V.3.1   Residual Curing Strain

Figure 30 shows the general behavior of $C \equiv C$ stretching frequency of P-HDU embedded in epoxy as a function of curing temperature. The $C \equiv C$ stretching vibrational band is used exclusively in this experiments since its frequency is the most sensitive to the applied strain. The

epoxy resin used is EPON 828 cured with DTA. At room temperature, the frequency of the fiber embedded in the epoxy is considerably higher, about 5 cm^{-1}, than that of the fiber alone. When the temperature is increased to 60°C, its curing temperature, the difference in frequency seems to disappear. The disappearance of residual strain near the curing temperature is because the matrix becomes soft so that the fiberbehaves as though there is no matrix around it. In other words, thematrix does not have enough solid-like characteristics to influence the thermal behavior of embedded fiber [143]. Since the inherent glass transition temperature of EPON 828 cured with equivalent amount of DTA is near 130°C, the glass transition temperature of incompletely cured epoxy is near its curing temperature.. The residual strains observed at room temperature are the result of two processes that occurs simultaneously, as discussed in the introduction. They are the volume changes due to the crosslinking and the difference in thermal shrinkage between the fiber and the matrix. In order to separate these two effect, it is necessary to study the change in frequency as a function of time at constant temperature. During isothermal curing, once the matrix gels enough to become solid-like, the volume shrinkage due to the additional crosslinking reactions can be converted into the residual strain on the fiber.

The result of the isothermal curing of the same sample is shown in Figure 31. The data points above 60°C shown in Figure 30 is the average value of the data points at the constant temperature in Figure 31. The post-curing schedule, i.e. temperature and time, is also shown in

Figure 30.   Frequency variation of the C≡C stretching vibration as a function of temperature.   (■) P-HDU fiber alone, (+) P-HDU fiber embedded in EPON 828 cured with DTA.
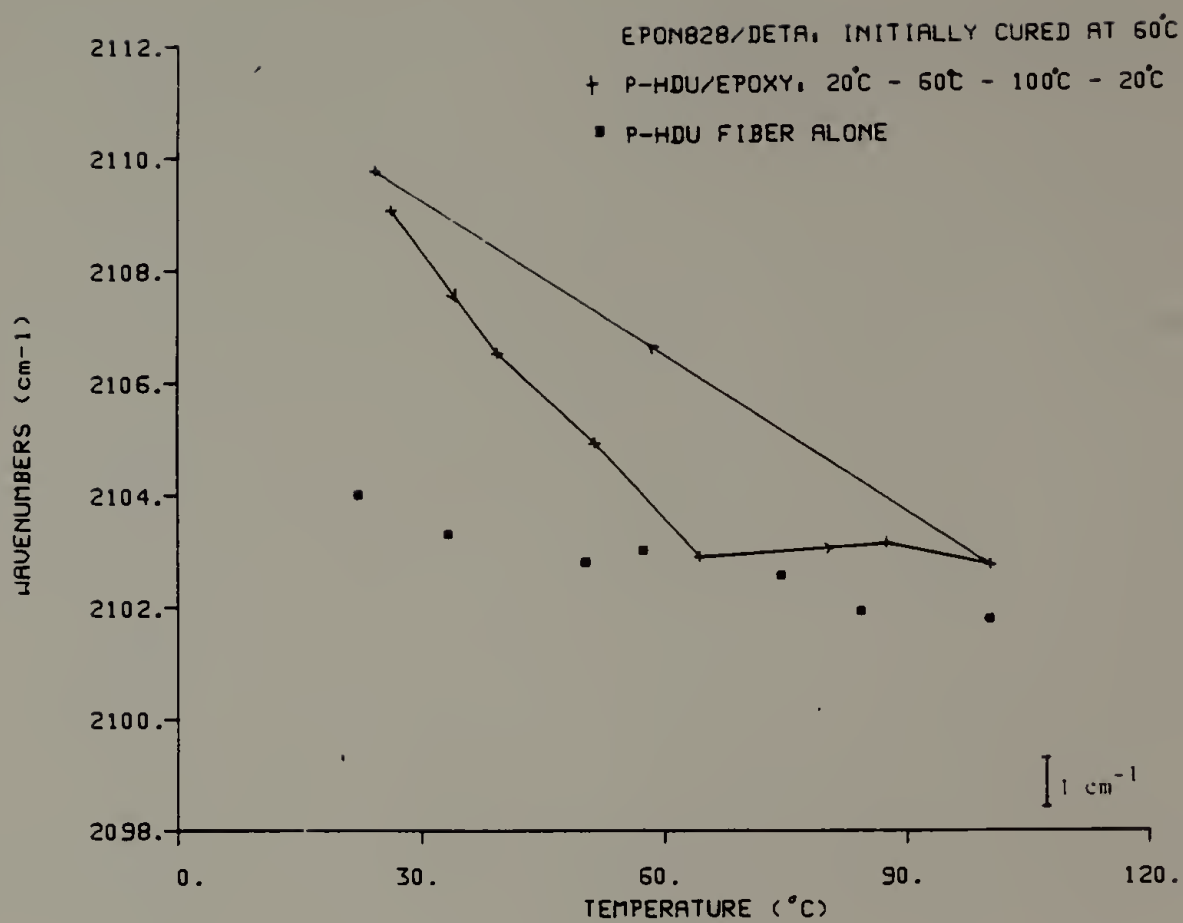
Figure 30.

Figure 31. Frequency variation of the C≡C stretching vibration as a function of time at various temperature. P-HDU is embeded in EPON 828 cured with DTA initailly at 60 C for 12 hours.
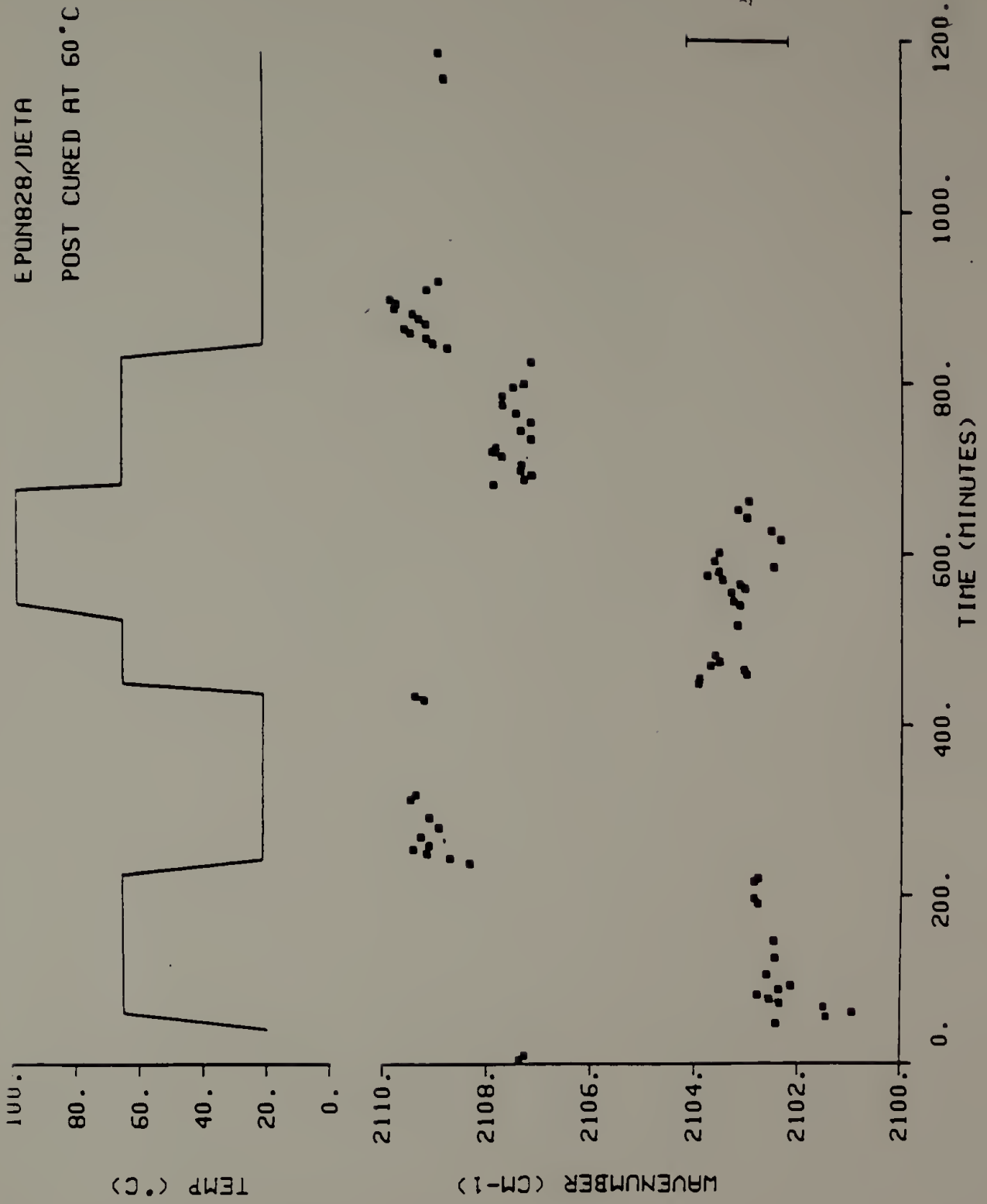
Figure 31.

Figure 31. When the temperature is first increased from 20°C to 60°C, the frequency sharply decreases to 2101 cm^{-1} before stablizing near 2102.5 cm^{-1}. This sharp drop in frequency suggests alight tensile deformation of the fiber. But no additional changes in frequency is observed for two hours at this temperature. Additional post-curing at 100°C shows that although the frequency fluctuates more, its average frequency at 100°C is near that of 60°C. Since the frequency of P-HDU fiber alone decreases during the samé temperature range (see Figure 30), this difference in frequency between them, about 1 cm^{-1} at 100°C, represents the effect of residual strain exclusively due to the volume shrinkage during the crosslinking reaction. The small magnitude of the difference from increasing the temperature from 60°C to 100°C indicates that the residual strain due to the crosslinking reactions is small. When the temperature is decreased back to 60°C, the C≡C stretching frequency is higher than the frequency before the post-curing at 100°C. This is expected since the glass transition temperature, i.e. onset of the residual thermal strain, and the modulus of the matrix increased after post-curing. Additional increase is observed when the temperature is lowered from 60°C to 20°C.

In order to determine the quantitative relationship between the curing strain and the extent of curing reactions, we have followed the extent of crosslinking reaction of EPON 828/DTA with infrared spectroscopy. Figure 32 shows the vibrational spectra of epoxy as a function of temperature and time. The vibrational band at 918 cm^{-1} is a characteristic band for uncured epoxy ring. The bottom spectrum is

Figure 32. Infrared spectra of EPON 828 cured with DTA as a function of temperature. Resolution 2 cm^{-1}; 32 scans.
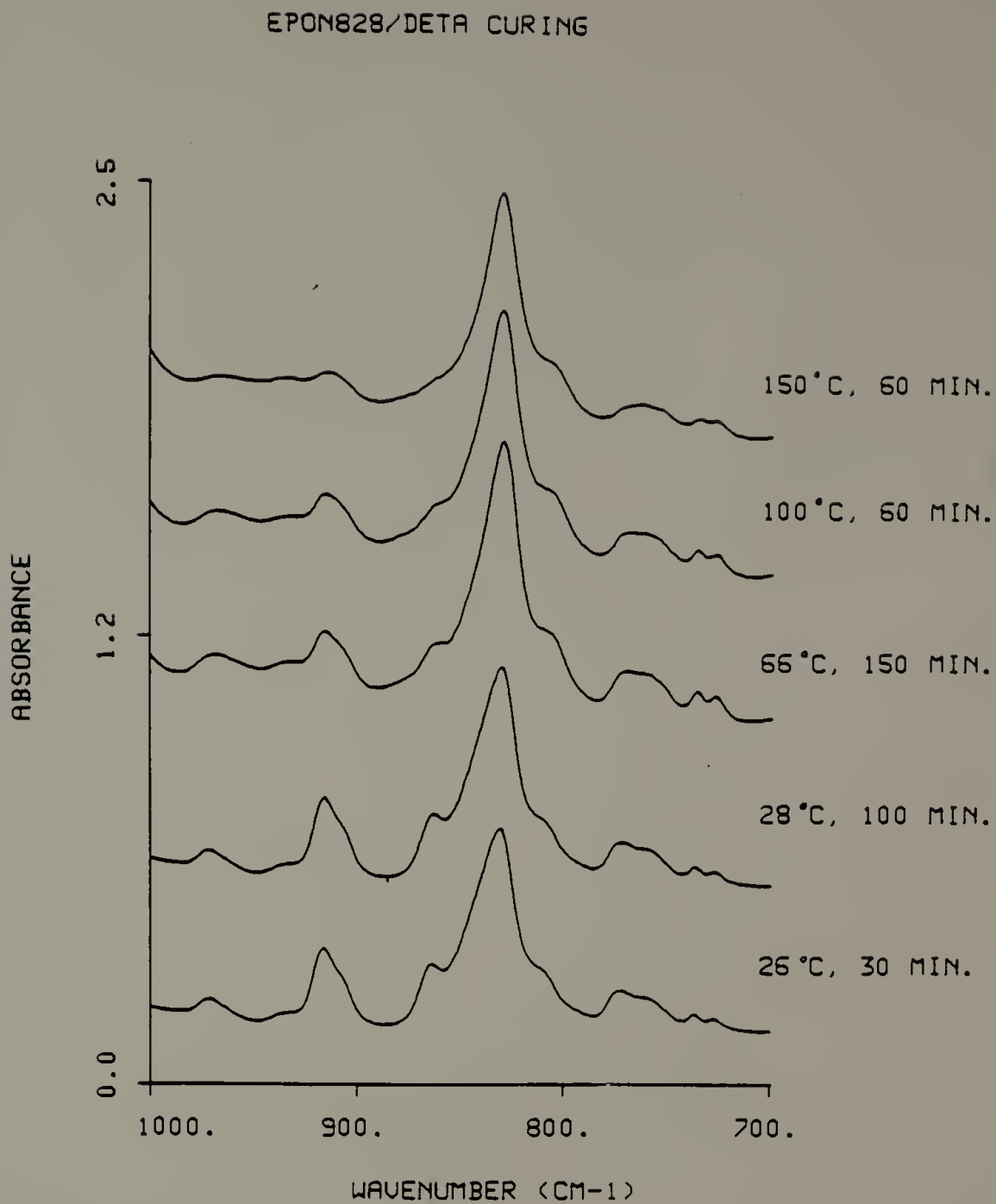
Figure 32.

obtained in 30 minutes after mixing. Since the intensity of 918 cm^{-1} band did not change after additional 70 minutes at this temperature, we decided to use this spectrum as a reference for the uncured epoxy. The intensity of this band after 2.5 hours at 60 $^\circ$C decreased, but still there are about 60% of epoxy groups remained unreacted. Additional curing at 100 $^\circ$C for an hour reduced the uncured epoxy content by only 10%. Therefore, 1 cm^{-1} changes in frequency observed in Figure 32 represents the effect of the volume change for about 10% crosslinking reaction. There seem to be very little change in intensity as a function of time beyond about 30 minutes after each temperature changes indicating that the most of the additional crosslinking reactions take place immediately after the temperature increase and decreases drastically with time due to the increase in viscosity.

The residual strain is very sensitive to the glass transition temperature, thermal expansion coefficient, and modulus. Post-curing also affects all these properties of epoxy. Figure 33 shows the result of dynamic mechanical study of post-curing of this matrix using DMTA. Post-curing up to 150 $^\circ$C shows increase in both the elastic modulus and glass transition temperature as expected. The temperature was increased at 4 $^\circ$C/minute. Since thermal strain due to thermal expansion mismatch is proportional to matrix modulus and glass transitional temperature, one would expect to see higher frequency at room temperature after post-curing at 100 $^\circ$C. But the frequency is only slightly higher compared to 60 $^\circ$C cured epoxy. This could be explained by the possible reduction in the thermal expansion coefficient of the epoxy after additional

Figure 33.   Dynamic mechanical spectrum of EPON 828 cured with DTA at 60 C.
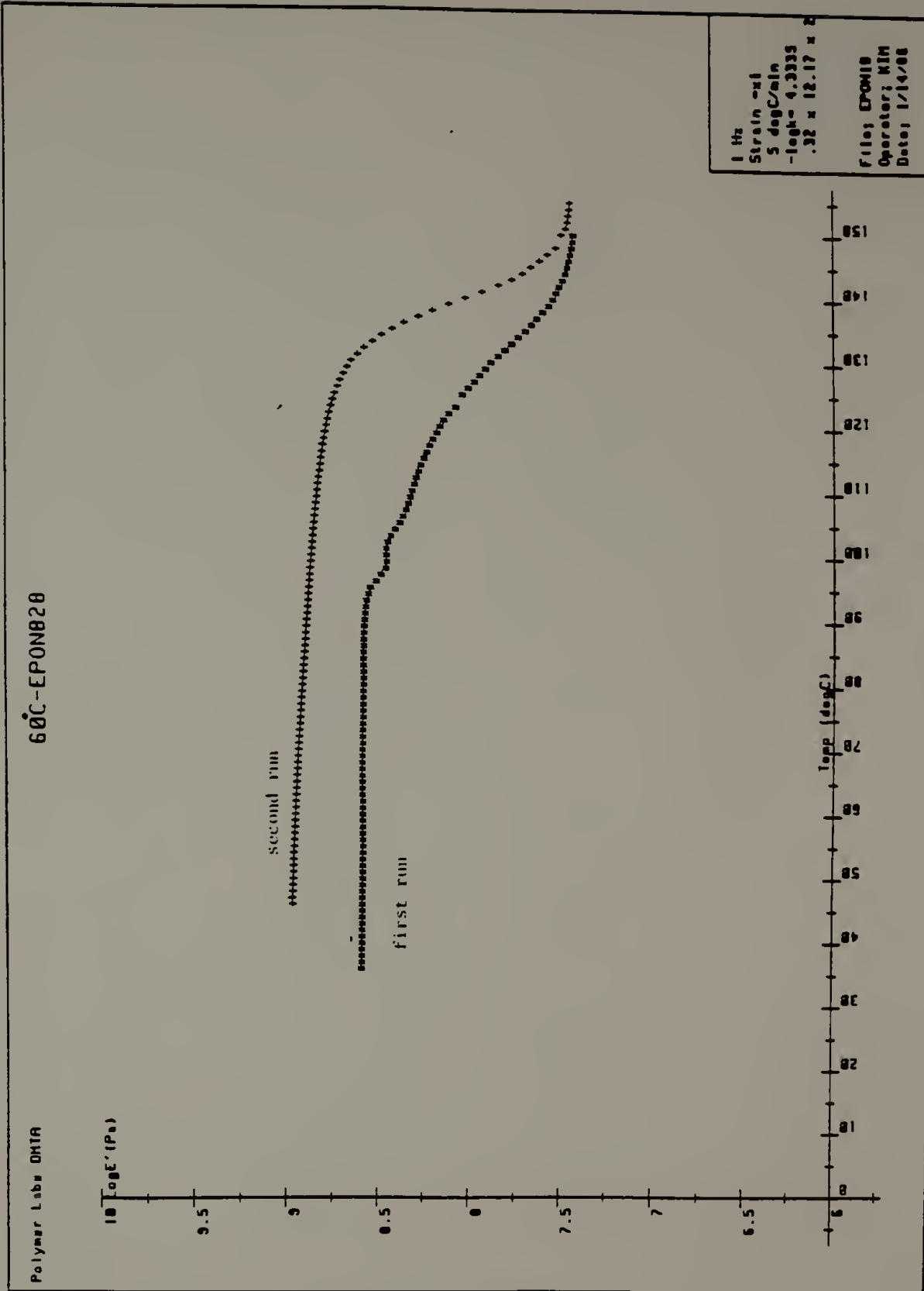
Figure 33.

crosslinking. This would reduce the magnitude of the slope between the frequency and the temperature so that the difference in frequency at 20°C would be less as well.

Additional curing study was carried out in order to examine the curing residual strain during the early stage of curing. For this experiment, the epoxy resin is initially cured at 22°C for two hours. The extent of crosslinking reaction is minimal during this time as shown in Figure 32. The result is shown in Figure 34. During the isothermal curing at 60°C for four hours, the frequency decreased initially similar to that of the fiber alone and then stabilized. This suggests that the residual strain due to volume shrinkage at the beginning of the curing during 40% of epoxy reacted is small. Most of the curing strain is dissipated since the volume change occurs while the resin still does not have enough solid-like characteristics at this early stage of curing.

V.3.2   Residual Thermal Strain: Magnitude

Unlike the small residual strain observed due to the crosslinking reactions during curing, it is generally agreed that the volume shrinkage caused by this difference in the thermal expansion behaviors is the major contributing factor to the observed large residual strain on the reinforcement and the composite. In this second part of this research, we were interested in studying the development of the residual strain as a function of temperature and its effect on the integrity of the interface and the composite properties.

Figure 34.   Frequency variation of C≡C stretching vbration as
during isothermal curing at various temperature.   P-HDU is embedded in
EPON 828 initially cured with DTA at 20 C.

EPON828 CURING STUDY
resin is pre-cured at room temperature for 2 hrs

Figure 34.

178
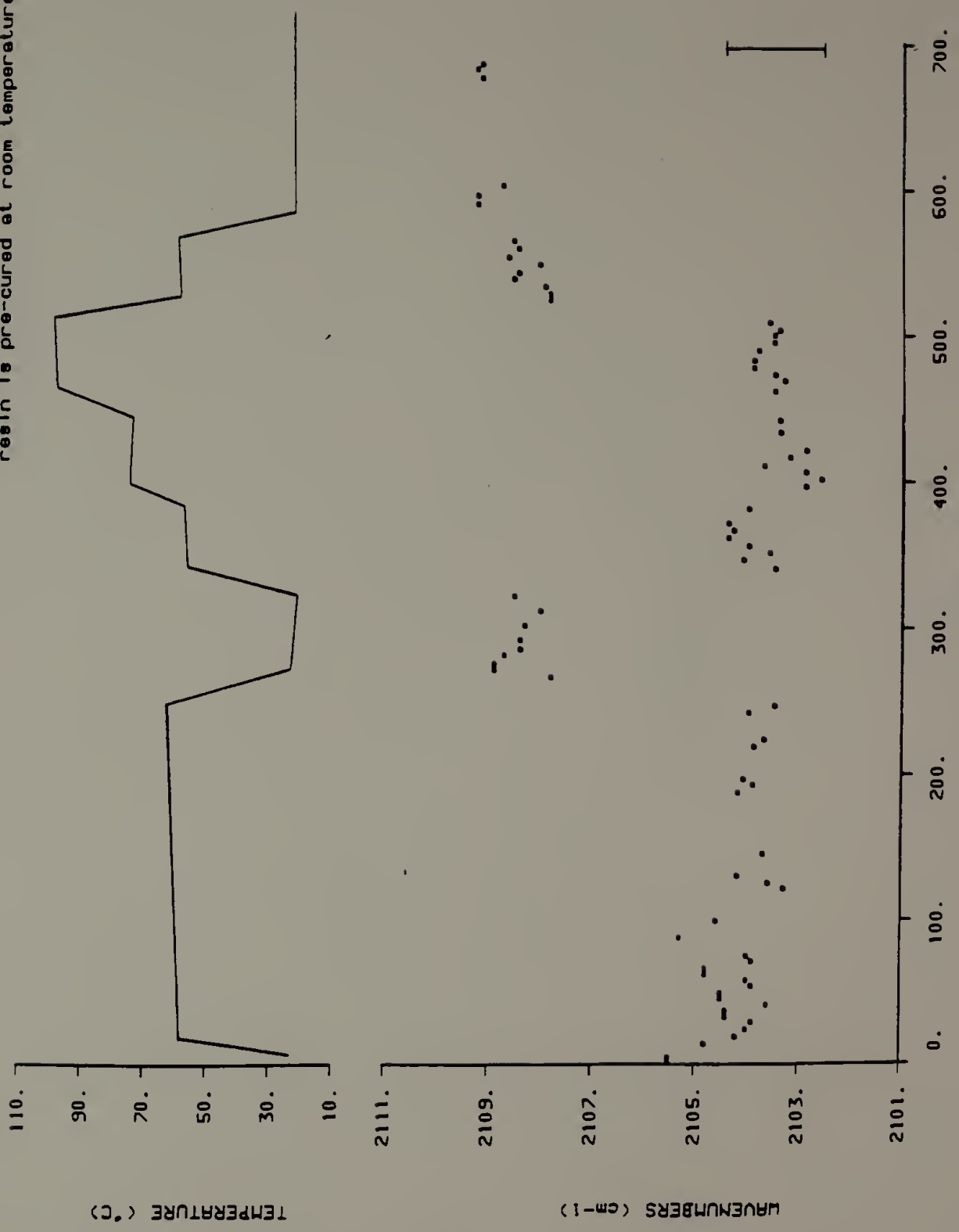
The frequency of the C≡C stretching vibrational mode increases by 6 cm^{-1} when the temperature is varied from 20°C to -130°C. This change may be interpreted as being simply due to increasing perfection in the intermolecular interaction. However, when the same fiber is incorporated in the polymer matrix, this change in the triple bond vibrational frequency shown in figure 35 is much more significant than that for the fiber alone. The matrix used is 60% EPON 825/40% DER 736 by weight cured with the stoichiometric amount of DTA at 60°C. As can be seen in these figures, when this fiber is embedded in the epoxy matrix, there are additional changes in band position as a function of temperature. When the temperature is lowered from 20°C to -130°C, the C≡C stretching frequency increased as much as 18 cm^{-1}; 12 cm^{-1} greater than the increase for the fiber alone. Because the epoxy is a glassy matrix, the absolute magnitude of these frequencies are strongly dependent on the sample preparation and the sample thermal history. This additional increase in frequency is presumable due to the thermal strain caused by the differences in the thermal expansion coefficient between the fiber and the matrix. The associated problem of residual thermal strain is also quite complicated for the composites made with high modulus and strength fibers because of this difference in thermal expansion coefficients between the matrix and the fiber and the anisotropy of the fiber properties.

In order to determine the type and the magnitude of the residual strain, both the geometry of the composite and the mechanical and thermal properties of the fiber and the matrix must be known. The

Figure 35. Temperature dependance of the Raman spectra in the
C≡C stretching region of P-HDU fiber. (●) fiber alone, (▲) fiber
embedded in 60% EPON 825/40% DER 736 by weight epoxy cured with DTA
at 60 C.

MATRIX, 60% EPON825, 40% DER736

sample, BE.THR

$V_{fiber} = 0.22$%

WAVENUMBER

TEMPERATURE (°C)
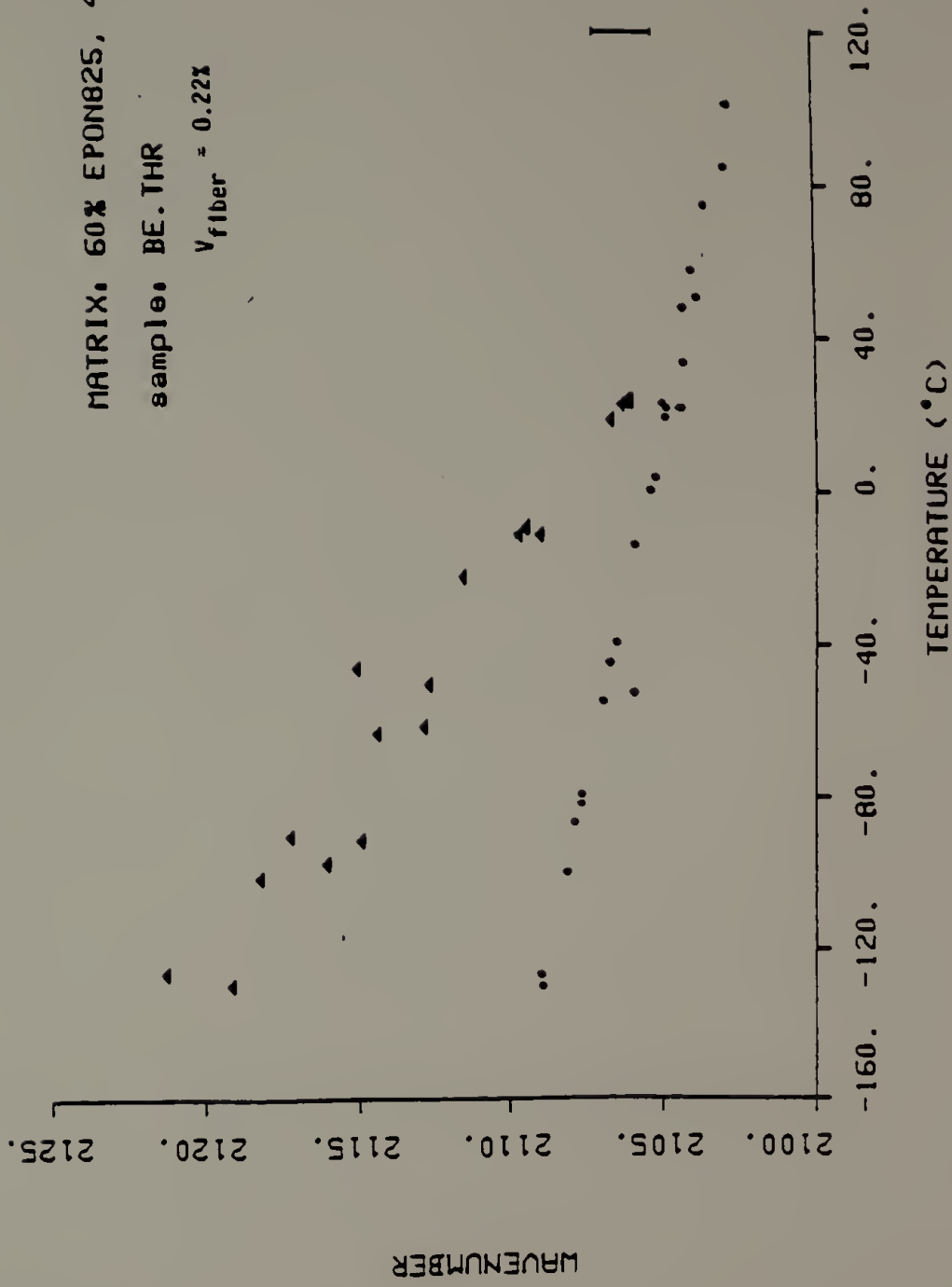
Figure 35.

theoretical thermoelastic analysis of residual stresses in the unidirectional composite with anisotropic fibers has been carried out [83]. But, in general, a complete description of the mechanical and thermal properties of these very small and highly anisotropic fibers used as reinforcements are not available. Therefore, our interpretation of the data obtained is done under various assumptions to estimate the relative magnitude of the thermal stresses that develop in this P-HDU/epoxy model composite during the temperature change from 20°C to -130°C.

Generally speaking [83], for high performance fibers such as graphite or Kevlar^R fiber have negative thermal expansion coefficient in the chain direction, and the longitudinal thermal stresses in the matrix will be tensile whereas they will be compressive in the fiber as temperature decreases. Radial stresses will be compressive in both the fiber and the matrix as temperature decreases, providing that the matrix thermal expansion coefficient is larger than that of the fiber. The magnitude of these thermal stresses are strongly dependent on the fiber volume fraction, V_f, in particular at low V_f, because the relative contribution of the fiber to the overall composite modulus increases rapidly at low V_f.

Using Nairn's thermoelastic analysis, the upper limit for longitudinal thermal stresses in the matrix is $\Delta\alpha E_m/(1-\nu_m)$ and the lower limit is $\Delta\alpha E_m F$ where $F = (E_L V_f)/(E_m V_m + E_L V_f)$, ν_m is the Poissons ratio for the matrix, $\Delta\alpha = \alpha_m - \alpha_L$ (the difference in the longitudinal thermal expansion coefficient), V_m is the volume fraction of the matrix, and E_L

For the temperature range from $20°C$ to $-130°C$, changes in the fractional length in the longitudinal direction is estimated to be 18×10^{-4} (using Figure 4 of Ref. 21) and the average thermal expansion coefficient in this temperature range is then to be approximately $-1.20 \times 10^{-5}/°C$.

Since the tensile modulus of P-HDU is approximately 45 GPa [117], and the tensile modulus of this epoxy is about 4 GPa, then, using $\nu_m = 0.34$, $\alpha_m = 4 \times 10^{-5}$, and $V_f = 0.001$, the changes in the stretching frequency expected for upper and lower limits for temperature decrease of $150°C$ are listed in Table 14. The lower limit of the frequency change due to the thermal stress is close to the measured value of 14 cm^{-1}. At very low volume fraction of fibers, the difference in the lower limit of the longitudinal thermal stress and the calculated one is very small since the matrix property dominates the thermal stresses as shown in Figure 3 of Ref. 83.

We have shown earlier that when the polydiacetylene fiber is under tensile deformation, the backbone vibrations such as the $C=C$ or $C\equiv C$ stretching modes decrease significantly. However, the increase in the frequency need not directly reflect the contraction along the fiber direction. Similar movements in the positions of the $C=C$ or $C\equiv C$ stretching vibrations of the polydiacetylene fiber alone with decreasing temperature have been reported [144]. The polydiacetylene fiber used in that study has a positive thermal expansion coefficient [145]. Therefore, it was not suprising to observe the increasing frequency when

TABLE 14

Calculated Results of Limits of Longitudinal Residual
Thermal Stress in P-HDU Embedded in Epoxy Matrix

<div align="center">

Upper Limit   **Lower Limit**

</div>

$$\sigma_{Zf} = \left(\frac{\Delta\alpha E_m}{1-\nu_m} \right)\left(1-\frac{1}{V_f} \right) \qquad \sigma_{Zf} = \Delta\alpha E_m \frac{V_f E_L}{E_m V_m + E_L V_f} \left(1-\frac{1}{V_f} \right)$$

σ_{Zf}:	-47.2 Gpa	-0.35 GPa
ε_{Zf}:	-1.05	-0.007
$\Delta\nu_m$:	$2100\ cm^{-1}$	$14\ cm^{-1}$

the chain repeat shortens at low temperature for the fiber alone.
However, P-HDU single crystal fiber has a negative thermal expansion
coefficient [131], making the increasing frequency of the fiber itself
as temperature decreases more difficult to explain. Using the expansion
coefficient measured earlier, we would expect a total increase of
approximately 9 cm^{-1} in the C≡C stretching frequency during temperature
change from -140°C to 100°C. Instead, we observed an increase in
frequency of the fiber alone when temperature decreased. This
unexpected frequency/temperature relationship demonstrates that the
longitudinal stress cannot be the only factor in perturbing the
frequency of the polymer backbone vibrations. The effects in the
changes in the intermolecular interaction cannot be ignored. A clean
separation between these two contributing factors will be difficult to
carry out.

It is then extremely interesting to speculate whether the frequency
change of the fiber embedded in a matrix during temperature change is
due to an effective reduction in the fiber length due to the
longitudinal compressive stress and shear stress at the interface in a
composite, thus raising the frequency, or due to much tighter packing
arising from the effective radial stress of epoxy "squeezing" on the
fiber, which would enhance the intermolecular interactions in addition
to the temperature effects. Without the Poissons ratio, transverse
thermal expansion coefficient and moduli of P-HDU, it would be difficult
to explain quantitatively the changes observed. Nevertheless, the
hypothesis that changes in intermolecular interaction cannot be ignored

is supported by two previous observations. It has been found that the delocalization of the electrons along the backbone can depend on the perfection of the chain packing [146]. Vibrational frequencies in resonance Raman scattering process depends upon either the energy of the absorption maximum or the incident radiation frequency [147]. In addition, the Raman spectra can be altered by hydrostatic pressure [144]. Therefore, the vibrational frequencies measured for P-HDU as a function of temperature may not entirely represent the effects induced by residual stress.

V.3.3   Residual Thermal Strain: Effects on the Interface

The C≡C stretching frequency of the fiber embedded in the resin consisted of 60% EPON 825 and 40% DER 736 as a function of temperature in Figure 35 increased linearly with a decrease in temperature up to -130° C. For the single fiber model composite of P-HDU embedded in 100% EPON 828 with the same curing agent, this was not the case. The epoxy resin was first cured at 100° C so that its glass transition temperature will be greater than the experimental temperature range. This sample was subjected to the temperature cycles as shown in the Figure 36. During the first cooling cycle from 100° C to -130° C, the frequency increased as expected. But, there seems to be a sharp change in the slope near 0° C as indicated by the arrow. If the integrity of the interface between the fiber and the matrix remains the same, then the slope should not change since both the fiber and the matrix have almost

Figure 36. The C≡C stretching frequency versus temperature for P-HDU fiber. (■/x) fiber embedded in EPON 828 cured with DTA at 100 C for 6 hours, (o) fiber alone.

EPON828/DTA. INITIALLY CURED AT 100 °C
— FIRST TRY: 20°C – 100°C – 20°C – -130°C – 20°C
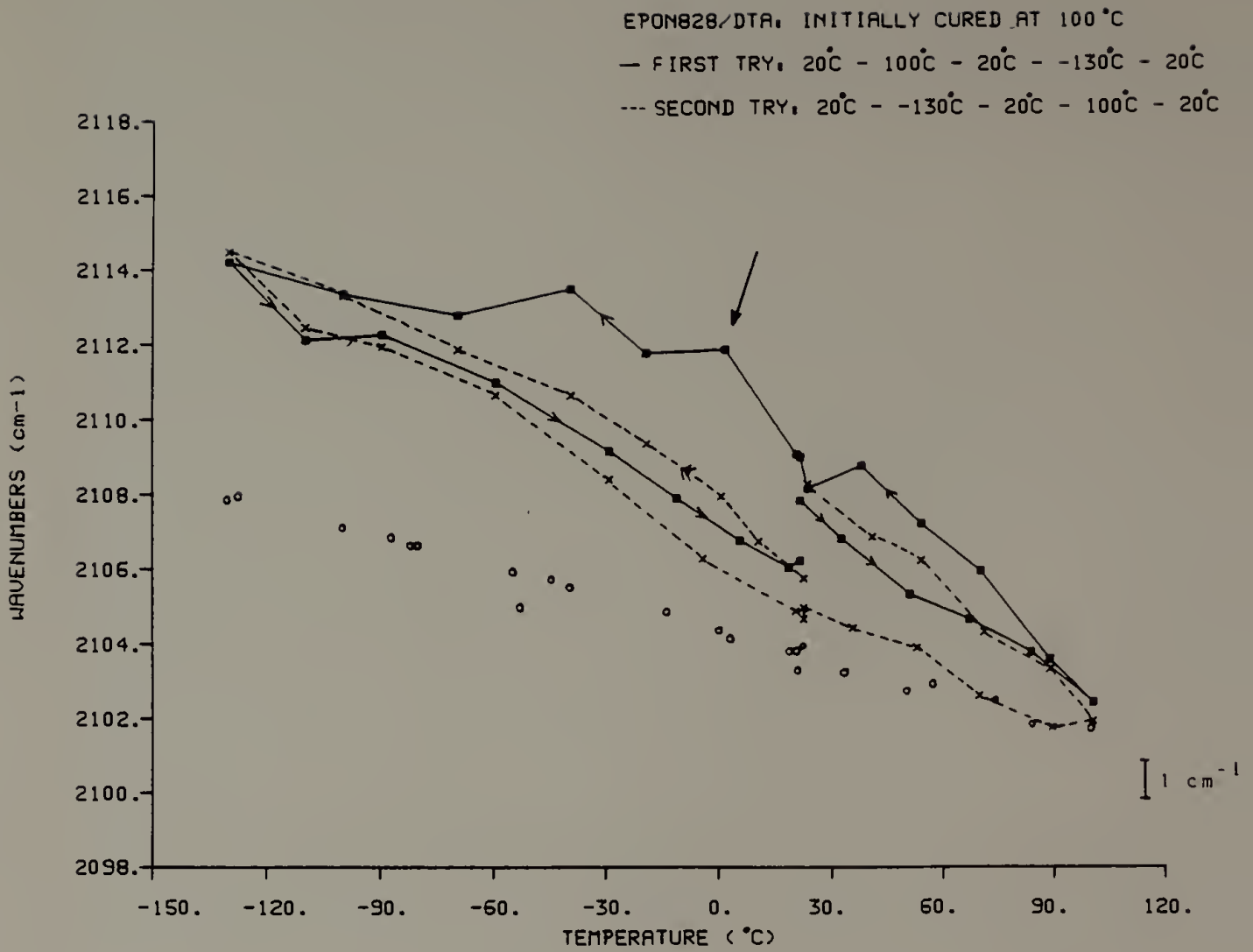--- SECOND TRY: 20°C – -130°C – 20°C – 100°C – 20°C

Figure 36.

Figure 37.   The plot of the difference in frequency between P-HDU fiber alone and P-HDU fiber embedded in epoxy as shown in Figure 36. (a) first temperature cycle, (b) second temperature cycle.

EPON828/DETA, POST-CURED AT 100°C
first try
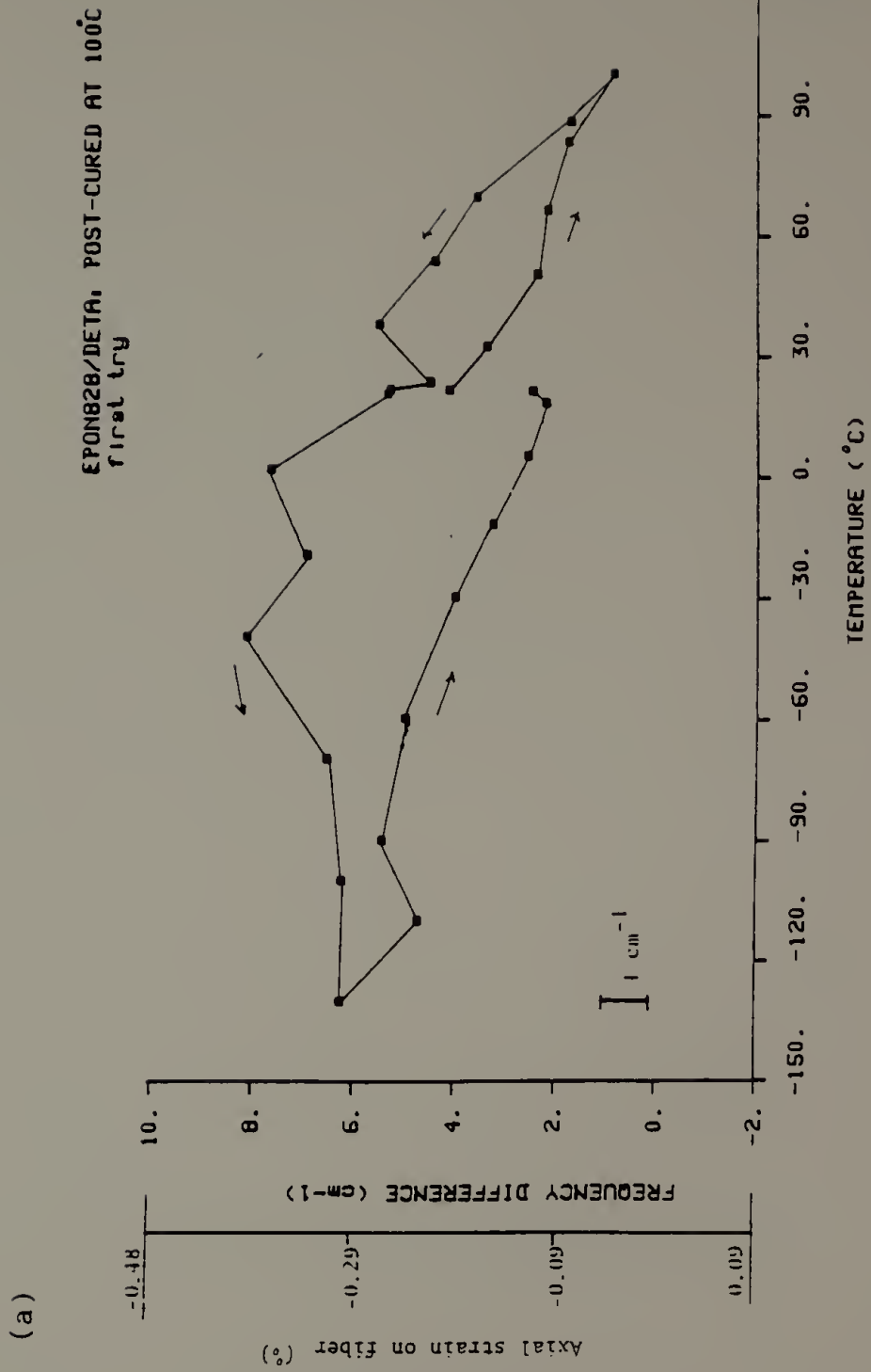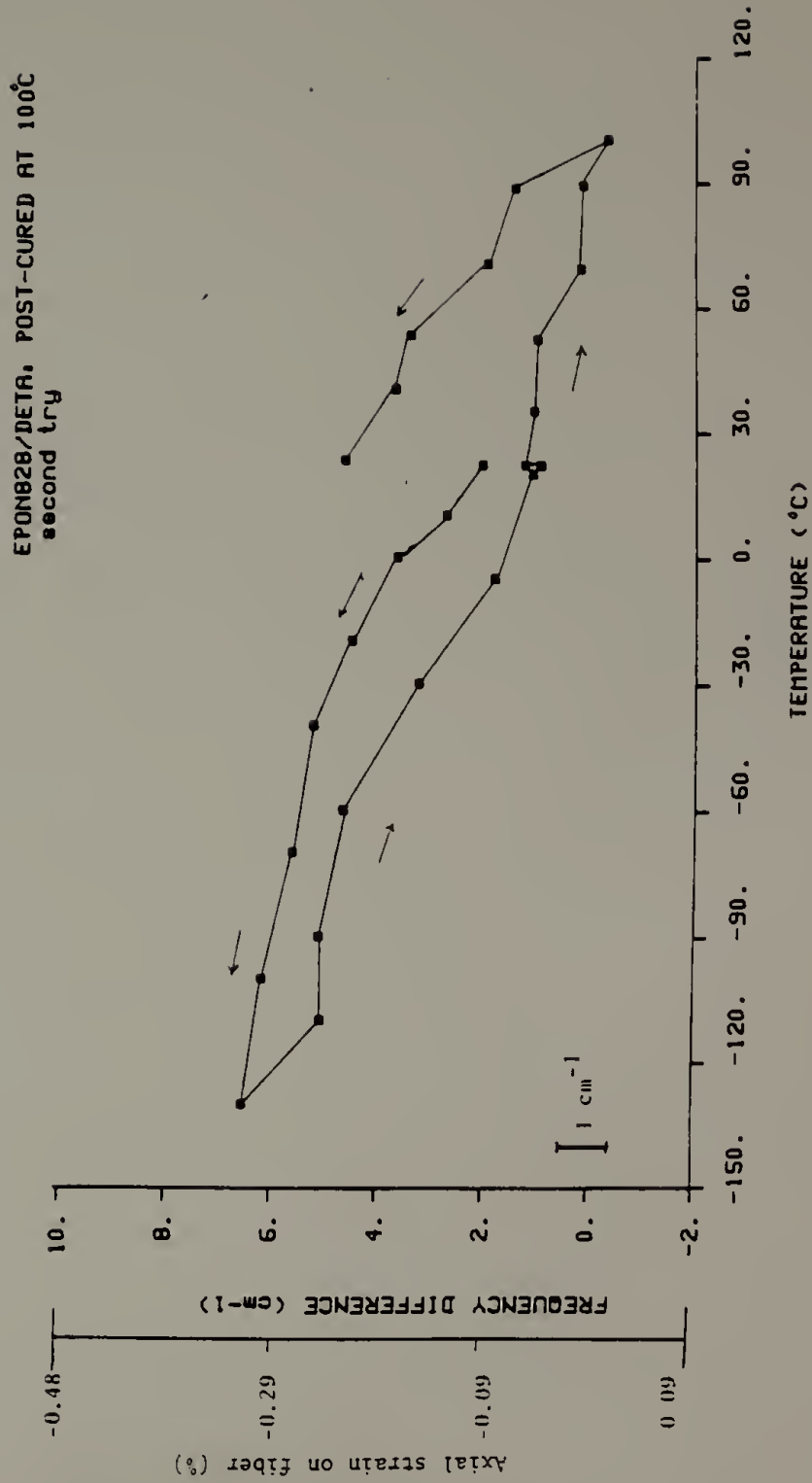
Figure 37.

Figure 37.

constant physical constants for this temperature range. It is possible that some changes in the interface property related to its ability to transfer the thermal stress from the matrix to the fiber may have occured so that the residual strain in the fiber increases more slowly than expected as temperature decreases. Additional evidence of the reduction of the thermal residual strain in the fiber is a decrease in the room temperature frequency after the sample has been cooled to the temperature below $-50\ ^{\circ}C$. The changes in the slope and the room temperature frequency are shown more clearly in Figure 37.

Possible explanations for this slope change and the reduction of room temperature residual strain in the fiber are twinning of P-HDU fiber [145], matrix yielding near the interface, or interfacial bond failure resulting in slip-stick behavior at the interface. According to the thermoelastic analysis [83], the largest residual thermal stress in the matrix and the fiber is the longitudinal thermal stress, under the assumption of perfect bonding at the interface and elastic behavior of constituents. Since P-HDU has negative longitudinal thermal expansion coefficient and the epoxy resin has a positive thermal expansion coefficient, the P-HDU fiber and the epoxy matrix experiences compressive and tensile residual thermal stresses, respectively as temperature decreases. This mismatch in the stress at the interface may ultimately cause either the compressive failure of the fiber such as twinning [148], matrix yielding [149], or interfacial bond failure [111].

When the low temperature cycle is repeated, the frequency (broken line in Figure 35) follows the similar behavior as that of the increasing temperature segment (-130°C to 20°C) of the first cycle. This suggests that whatever changes that may have occured at the interface near -50°C appear to be permanent. This suggests that the twinning of the fiber may not be the cause of the slope change observed in the first temperature cycle. When the temperature is increased to the temperature to near its glass transition temperature and cooled to room temperature again, the frequency at room temperature increased to the value close to the original value. At this time, it is not clear of the mechanism of this recovery of residual strain during this heating cycle. It may be possible that near the glass transition temperature, the motion of lower molecular weight fractions, whose glass transition temperature is lower, increases enough to heal any microcracks and delaminations at or near the interface. It is also interesting to note that there is a hysteresis present during the temperature cycle. The frequency seems to be always higher during heating than cooling. If this is a time dependent phenomenon, then it must be very slow since even after four hours at the same temperature, the same difference still exists. This is expected since the experimental temperature range is all below its glass transition temperature so that all motions are effectively frozen. Based on this experiment alone, it is impossible to distinguish various possibilities of causes for the slope change and mechanisms of residual stress recovery. Additional experiments such as optical birefringence experiment are needed.

V.3.4 Effect of Two-Phase Matrix on Residual Strain in Fiber

The reinforcement fibers in composites are usually coated with various sizing agents of coupling agents to improve specific composite properties. Introduction of this interphase layer may influence the nature of thermal residual strain in composites. In this study, we were interested in studying the effects of the interphase layer on the thermal residual strain of anisotropic reinforcements using P-HDU fiber coated with Solithane 113. Solithane layer will influence the residual stress distribution in the composite because of its lower glass transition temperature compared to the epoxy resin. The effect of glass transition temperature in the residual strain in the embedded fiber is clearly shown in Figure 38. The glass transition temperature of this Solithane matrix is near 0° C based on the dynamic mechanical data shown in Figure 39. Since the glass transition temperature is the temperature where liquid to solid (glass) transition takes place, there should be a change in slope near this temperature as shown in Figure 39. From 20° C to 0° C, the frequency change is indeed similar to that of the fiber alone since all the residual strain caused by the epoxy resin shrinkage is dissipated by the flexible interphase. As temperature is lowered below the glass transition temperature, the frequency increases more rapidly as seen in the epoxy matrix.

Figure 40 shows the plot of the $C \equiv C$ stretching frequency of Solithane coated P-HDU embedded in the epoxy resin as a function of temperature. The thickness of the Solithane interphase layer is very

Figure 38. Frequency variaton of C≡C stretching vibraion as a function of temperature. P-HDU is embedded in Solithane 113 cured with C113-300.

Figure 38.
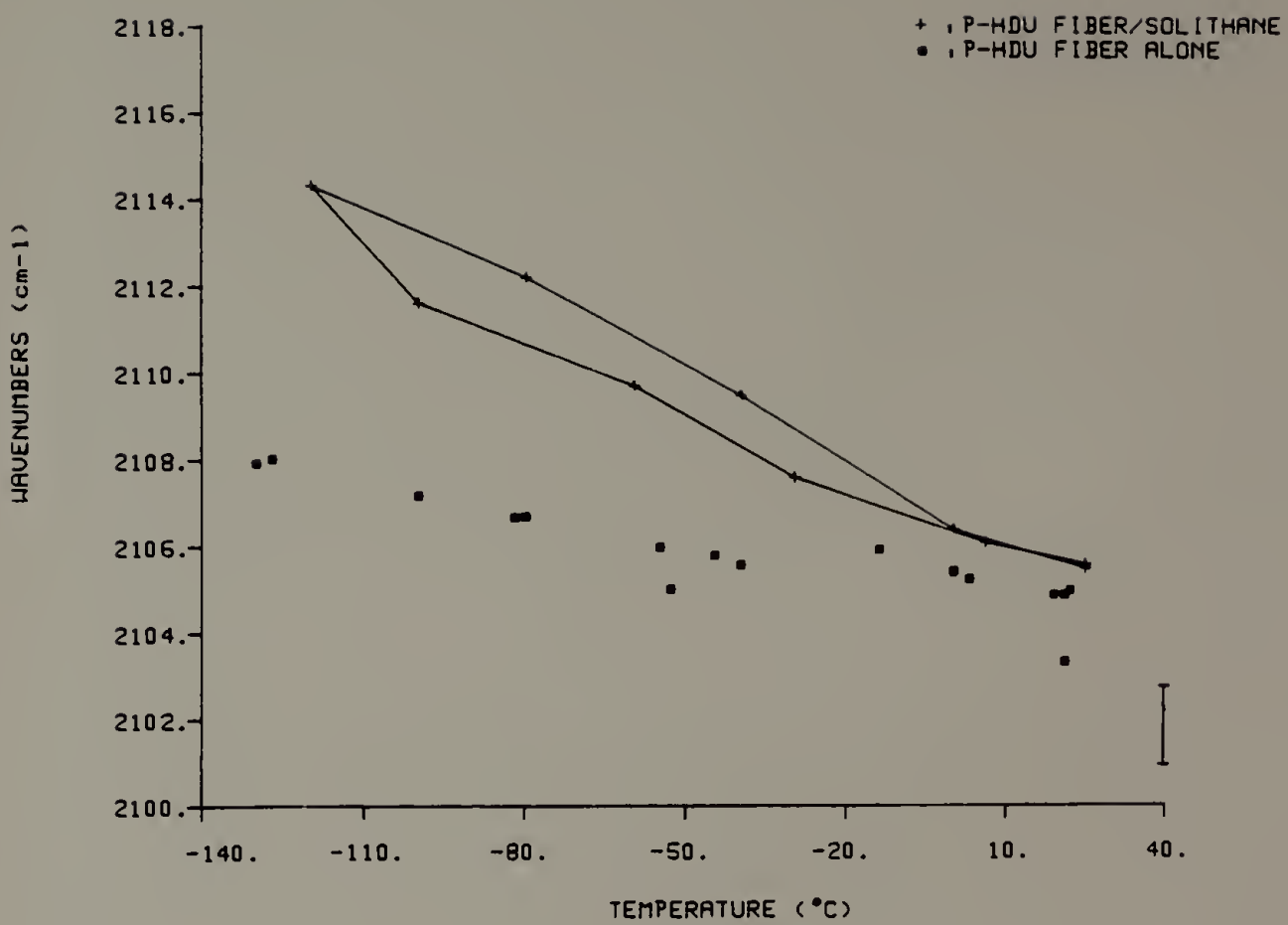
Figure 39. Dynamic mechanical spectrum of Solithane 113 cured with C113-300.
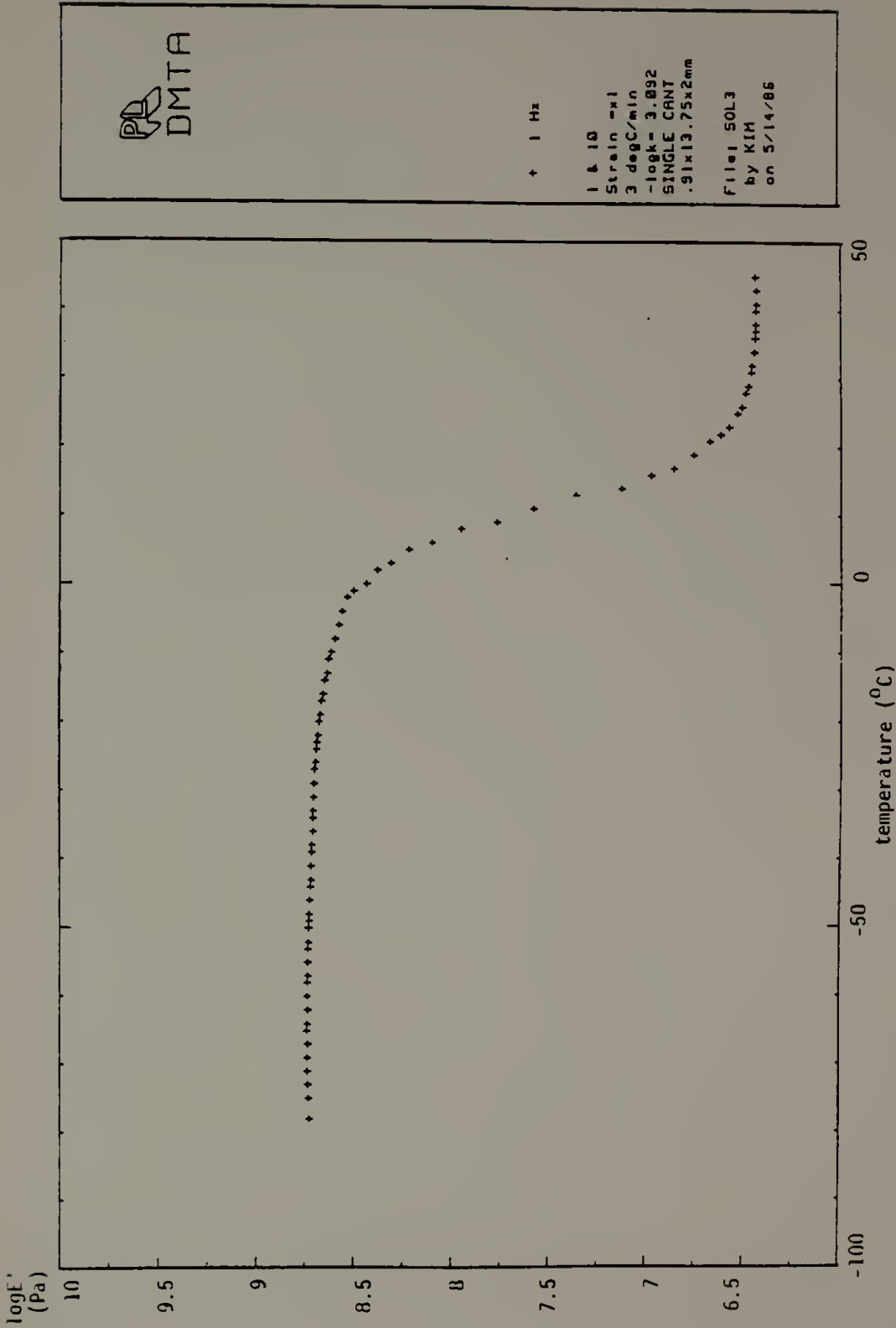
Figure 39.

Figure 40. Frequency variation of the C≡C stretching vibration of P-HDU coated with Solithane 113 as a function of temperature. (Y) fiber alone, (■) Solithane 113 coated fiber embedded in epoxy, and (o) uncoated fiber embedded in epoxy. Epoxy matrix is EPON 828 cured with DTA at 60 C.
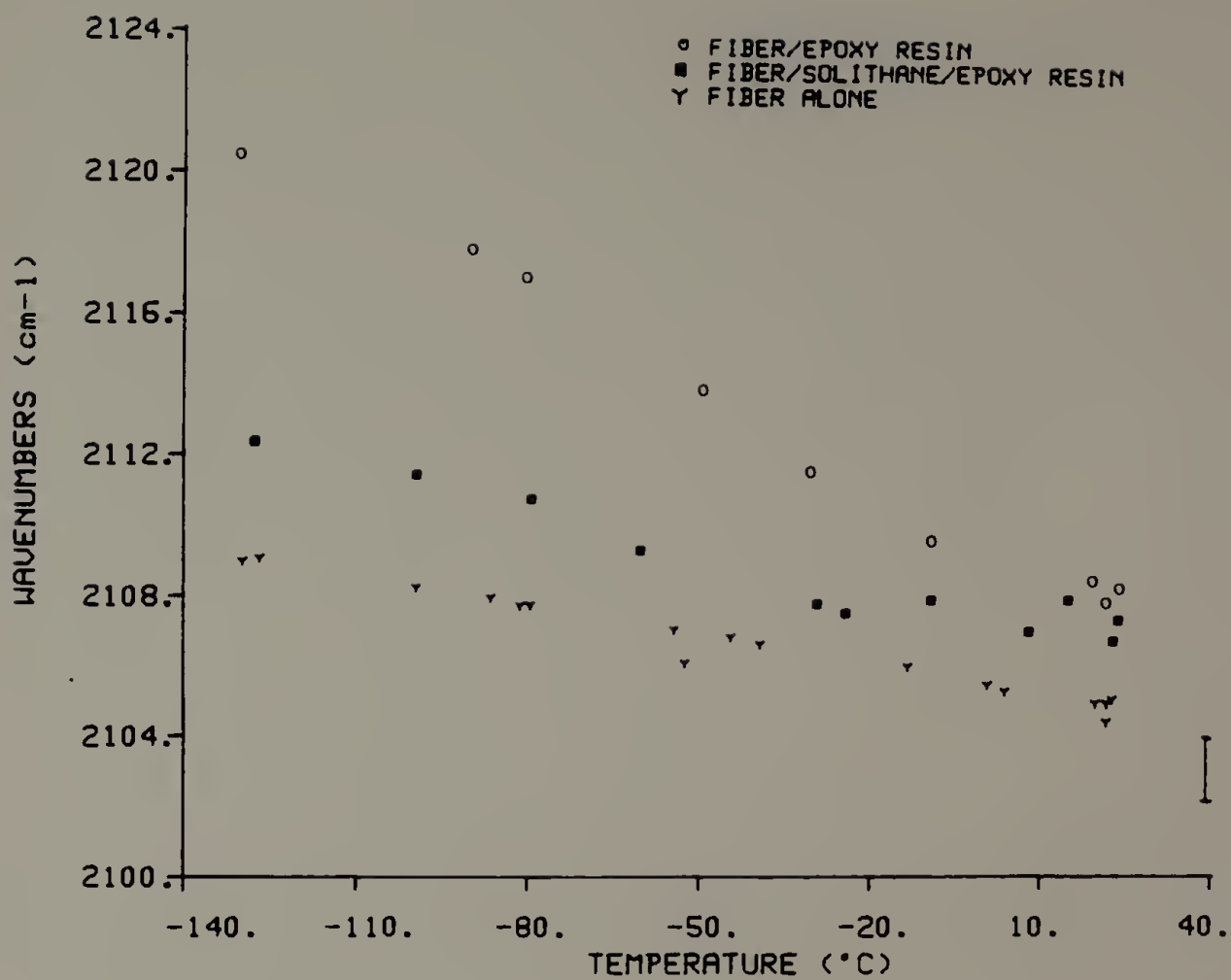
Figure 40.

much thicker than real composites. The overall fiber volume fraction is about 0.001 and the thickness of the interphase layer is about ten times the fiber radius. Although the sizing material applied in composites are actually much thinner, in the order of tenth of fiber radius, this study can provide qualitative understanding of the effect of interphase layers on the residual stress. For Solithane coated fiber, there is a decrease in the frequency for the sized fiber since the glass transition temperature of Solithane is much lower than that of epoxy matrix. This effect of glass transition temperature is seen as a slight change in the slope near 0°C for the sized fiber. Its slope below 0°C is still not as large as that of the fiber without the sizing material although the elastic modulus of Solithane below 0°C is similar to that of epoxy. This could be due to possible delamination between epoxy resin and Solithane interphase layer during cooling from 100°C to 0°C. Since Solithane is viscoelastic material during this temperature range, it would want to shrink a lot more than the epoxy. This could result in the reduction of the thermal residual strain due to epoxy resin since the effect of volume shrinkage cannot be transferred to the fiber. Therefore, the effective matrix that the fiber experiences is that of the interphase layer alone. However, further experiments are needed, again using optical microscopy, to verify this possibility of delaminations.

Lastly, it is important to realize that since epoxy is thermoset, it is very difficult to duplicate the experimental conditions exactly. This may be one of the larger contributions to the scatter in the data.

V.4   CONCLUSIONS

We have applied the Raman spectroscopic-mechanical technique that was developed in Chapter IV to study the effect of the residual thermal and curing strain to the reinforcement fiber using polydiacetylene fiber.   The residual strain due to the volume shrinkage during the crosslinking reaction is compressive and very small.   Additional 10% curing resulted in the frequency increase of only 1 cm^{-1}, which is equivalent to 0.05% axial strain when the temperature is increased from 60°C to 100°C.   Also, it was shown that this compressive effect of residual strain during curing appears only after the matrix has enough solid-like characteristics to transfer the stress to the fiber.

On the other hand, the effect of residual thermal strain during temperature changes is considerably greater than the residual curing strain.   For the matrix consisted of 60% EPON 825 and 40% DER 736, the frequency increased almost 15 cm^{-1} more than the fiber alone during cooling from 20°C to -130°C.   This corresponds to almost 1 GPa of compressive force acting on the fiber and will fail in compression, assuming the effect of transverse stress is minimal.   Its magnitude is greatly dependent of the glass transition temperature, modulus, and volume fraction of the matrix.   Also, because these epoxy are glassy and the fiber volume fraction is very low, it was difficult to reproduce the data exactly.   The exact value of the residual strain are greatly influenced by sample preparation, thermal history, and so on.

Introduction of the interphase layer with a lower glass transition temperature resulted in a large reduction of residual thermal strain.

The effect of residual thermal strain on the integrity of the interface/interphase has been observed with this technique. The thermal strain caused permanent reduction of the stress-transfer efficiency of the interphase by possible debonding at the interface, compressive failure fiber twinning, or matrix yielding near the interface. The magnitude of the residual thermal strain on the fiber is generally lower than that of thermoelastic analysis because of the over simplification in these theoretical analysis such as perfect interfacial bonding.

The analysis of the direction and the magnitude of the residual thermal stress was not possible due to the lack of necessary structural parameters of P-HDU.

C H A P T E R   VI

GENERAL RESULTS AND FUTURE WORK

This chapter contains our conclusions regarding the utilization of vibrational spectroscopy to understand the structure-property relationships of PPTA and the deformation behavior of an anisotropic fiber reinforcement embedded within a polymer matrix. Some suggestions and considerations for future works in this area of research are also presented in this chapter.

The vibrational spectra of PPTA and its model compound, benzanilide, were completely analyzed using normal coordinate analysis in non-redundant coordinates. The problems associated with the complex chemical structure of PPTA, particularly its many redundancies, were overcomed by using non-redundant coordinates in calculating the theoretical vibrational spectra. The construction of non-redundant coordinates and corresponding force field for benzanilide is described in Chapter II. These non-redundant coordinates were constructed in such a manner that the recognition of each vibrational motions was still possible. We used the results of previous studies on both various derivatives of the benzene ring and the amide group in this analysis. The calculated frequencies are in good agreement with observed values without any need for force field refinement. Transferability of the force fields from the benzene and the amide group to benzanilide is also demonstrated by using the same non-redundant coordinate system in the

205

analysis. This is the first time that the non-redundant coordinate system has been used in the normal coordinate analysis of molecules as complex as benzanilide and PPTA.

After the satisfactory result had been obtained for benzanilide, we then extended this approach to the vibrational analysis of PPTA. Almost the identical non-redundant coordinates and force field were applied for PPTA calculation based upon the excellent transferability demonstrated in Chapter II. Again, the calculated frequencies were in good agreement with the observed values without any need for force field refinement. The analysis was greatly assisted by two additional model compounds and deuterated PPTA. Agreement below 900 cm^{-1} was poorer. In this region, the vibrational motions become increasingly mixed, and the effects of intermolecular interactions becomes important as well. Both further normal coordinate analysis including these intermolecular interactions, and more experimental data, are needed for a better understanding of this low frequency region. The generally broad band shape exhibited by the highly oriented PPTA have been explained by the slight differences in the local chemical environments between both the two benzene rings and the two amide groups within the repeat unit. Furthermore, based on the normal coordinate analysis result, we calculated a theoretical modulus of 241 GPa for PPTA chain using the dispersion curve of the longitudinal acoustic mode vibration. The results of this theoretical vibrational analysis of PPTA will be an important and necessary contribution for any future studies on microstructure-property relationships of PPTA. In particular, its deformation behavior at the

molecular level could be ascertained through a study employing spectroscopic-mechanical technique.

The source of motivation for the second part of this thesis was to understand the fundamental mechanism of reinforcement in a composite. A new technique was developed to investigate directly the stress induced structural changes in a fiber embedded within a polymer matrix. This enabled a study which contrasted with most of the previous indirect studies of stress distribution in a fiber. It invoked the application of polydiacetylene single crystal fiber as the fiber, and utilization of Raman spectroscopy coupled to the computer controlled mechanical stretcher built for the Raman spectrometer. Model composite consisted of single polydiacetylene fiber embedded in a epoxy matrix was made for these experiments. The resulting measured axial surface strain distribution in the fiber in epoxy subjected to the tensile deformation parallel to chain axis was in qualitative agreement with the predictions of the composite theories. That is, the surface strain was indeed close to zero near the fiber ends and increased to a limiting value toward the center of the fiber. This limiting strain value or the critical length as a function of the applied composite strain is a direct measure of the stress transfer efficiency of the interphase and the matrix.

As a consequence of this technique, we were able to determine that the residual strain on the fiber arising from the volume change during curing was very small. In addition, the onset of this residual strain occured only toward the completion of curing, when the matrix became solid. In contrast, the residual thermal strain during the temperature

change was much greater. This strain was large enough to cause either compressive failure of the fiber or microcracks and yielding at the interface so that the stress-transfer characteristics of the interface or the matrix is modified. Furthermore, the reduction of residual thermal strain was demonstrated by adding on flexible matix layer in between the fiber and the hard, epoxy matrix. The experimental results of these thermal studies were in qualitative agreement with the thermoelastic analysis, but additional structural parameters of polydiacetylene are needed for further quantitative analysis of residual strain in a composite.

As demonstrated in this thesis, this Raman spectroscopic-mechanical technique using polydiacetylene single crystal fiber is a very powerful technique that can provide currently unavailable data in composite studies. some future applications of this technique are presented here. While this technique is used to study only the embedded fiber, the photoelastic technique can provide information concerning the deformation of the matrix and the compressive failure of fiber. The combination of these two techniques will allow complete analysis of the deformation of whole composite. Using a micro-Raman spectrometer which has a microscope attached to the sample chamber, it is possible to do both experiments simultaneously. In particular, the microscope could be used to study the twinning of polydiacetylene fiber and the formation of interfacial gaps resulting from microcracks and delamination, by consideration of optical tunnelling [150]. These experiments will

provide additional information needed to understand the slope changes seen in the residual thermal strain experiments (see Figure 36).

Although we have shown the effect of two-phase matrix on the residual strain of a fiber, the actual interphase layer of composite is much thinner that what we have tested here. It was difficult to apply thin, uniform coatings of sizing or coupling agent materials to P-HDU fibers. Direct chemical modifications of the P-HDU fiber surface would be a better way to study the effect of specific interfacial bonding on composite properties. Also, since Raman scattering is not affected by the presence of water, this technique could be extended to study the effect of physical aging on the interface arising from environmental moisture absorption.

Experimentally, the measured triple bond stretching vibration frequency corresponded to the apparent axial surface strain of the fiber. The separation of the effects of longitudinal versus transverse components of the residual thermal stress were not possible because the transverse properties of the highly anisotropic P-HDU fiber were not available. The determination of these structural parameters by X-ray diffraction study would greatly advance the understanding of the stress induced structural changes of the embedded fiber.

Although we have studied only a model composite consisted of a single fiber for this thesis, usual composites contain numerous fiber, in the order of 60% by volume. Therefore, in such cases the fiber-fiber interactions become an additional important factor in determining the final composite properties. Since the fiber ends are the locations of

the stress concentration, the net stress field around one fiber will strongly depend on the presence of adjacent fiber ends. Simple composite theories generally ignore this effect due to the complexity of the analysis, and the randomness of the actual fiber distributions in a composite. Riley [151] has derived the effect of fiber-fiber interactions on the stress distribution of the discontinuous fiber composites and many finite element analysis of fiber-fiber interaction are available [58,59], but corresponding experimental data are very limited. Again, using P-HDU fiber and Raman spectroscopy, it is possible to do a systematic study of fiber-fiber interactions by analyzing the strain distributions in the fiber in the model composites made of one, two, three, and more fibers.

Finally, similar studies of composites as accomplished in this thesis, and suggested above, can be undertaken with PPTA as the reinforcement. The microstrtuctural changes of PPTA could be elucidated by the stress induced spectroscopic changes. The experimental difficulties associated with very thin PPTA fiber and weak Raman scattering intensity could be overcomed by using a micro-Raman spectrometer. The chemical modification of the PPTA fiber surface have been well characterized [152]. Although infrared and Raman spectroscopy have been applied to examine polymers in tension, no satisfactory technique is currently available to examine high performance fibers under compression, at the molecular level. This is important since highly oriented fibers like PPTA generally have weak compressive properties. Few microstructural studies have been carried out to

understand the compression induced structural changes in polymers. The Raman spectroscopic-mechanical technique as described above can provide a sensitive well defined method by which one would selectively examine such structural changes on a molecular level in PPTA by using the result attained for the normal vibrational analysis of PPTA as a basis.

REFERENCES

1. B.R. Noton, <u>Engigeering Applications of Composites</u>, Academic Press, New York (1974).

2. R.L. McCullough, <u>Concepts of Fiber-Resin Composites</u>, Marcel Dekker, New York (1971).

3. W.B. Black and J. Preston, <u>High-Modulus Aromatic Fibers</u>, Marcel Dekker, New York (1973).

4. G.B. Carter and V.T.J. Schenk, <u>Ultra-High Modulus OrganicFibers</u>, I.M. Ward, ed., Ch.13, Wiley, New York (1975).

5. W.B. Black, Ann. Rev. Mat. Sci. <u>10</u>, 311 (1980).

6. G. Capaccio and I.M. Ward, Nature Phys. Sci. <u>243</u>, 143 (1973).

7. N.E. Weeks and R.S. Porter, J. Polym. Sci. Polym. Phys. Ed. <u>12</u>, 635 (1974).

8. P. Smith and P.J. Lemstra, J. Mater. Sci. <u>15</u>, 505 (1980).

9. P.W. Morgan, Macromolecules <u>10</u>, 1381 (1977).

10. C.P. Wong, H. Ohnuma, and G.C. Berry, J. Polym. Sci. Polym. Symp. <u>65</u>, 173 (1978).

11. J.F. Wolfe, B.H. Loo, and F.E. Arnold, Macromolecules <u>14</u>, 915 (1981).

12. J.A. Odell, A. Keller, E.D. Atkins, and M.J. Miles, J. Mater. Sci. <u>16</u>, 3309 (1981).

13. D. Bhaumik, H.H. Jaffe, and J.E. Mark, Macromolecules <u>14</u>, 1125 (1981).

14. D.Y. Shen and S.L. Hsu, Polymer <u>23</u>, 969 (1982).

15. S.R. Allen, Ph.D. Thesis, University of Massahusetts (1983).

16. S.L.Kwolek, P.W. Morgan, and W.R. Sorenson, U.S. Patent no. 3,063,966 (1962).

17. L. Penn, H.A. Newey, and T.T. Chiao, J. Mater. Sci. <u>11</u>, 190 (1976).

18. S.L. Kwolek, P.W. Morgan, J.R. Schaefgen, and L.W. Gulrich, Macromolecules <u>10</u>, 1390 (1977).

19. M. Panar, P. Avakian, R.C. Blume, K.H. Gardner, T.D. Gierke, and H.H. Yand, ibid. 21, 1955 (1983).

20. M.G. Dobb, D.J. Johnson, and B.P. Saville, ibid. 15, 2201 (1977).

21. S.C. Simmens and J.W.S. Hearle, J. Polym. Sci. Polym. Phys. Ed. 18, 871 (1980).

22. M.G. Northolt, Eur. Polym. J. 10, 799 (1974).

23. J.W. Ballou, Polym. Preprints, Am. Chem. Soc. 17, 75 (1976).

24. M.G. Dobb, D.J. Johnson, A. Majeed, and B.P. Saville, Polymer 20, 1284 (1979).

25. M.G. Northolt and J.J. Van Aartsen, J. Polym. Sci. Polym. Symp. 58, 283 (1977).

26. D.M. Riggs, R.J. Shuford, and R.W. Lewis, Handbook of Composites, G. Lubin ed., Ch. 11, Van Nostrand, New York (1982).

27. "Kevlar 49 Data Manual", E.I. duPont de Nemours, Wilmington, DE (1974).

28. R.E. Allred and E.P. Gerstle, Jr., Proc. 30th Rein. Plast./ Compos. Inst. Tech. Conf., paper 9-B, SPI, New York (1975).

29. M.G. Dobb, D.J. Johnson, and B.P. Saville, Polymer 22, 960 (1981).

30. S.J. DeTeresa, Ph.D. Thesis, University of Massachusetts, (1985).

31. M.M. Schoppee and J. Skelton, Tex. Res. J. 44, 968 (1974).

32. L. Konopasek and J.W.S. Hearle, J. Appl. Polym. Sci. 21, 2791 (1977).

33. M.G. Northolt and J.J. Van Aartsen, J. Poly. Sci. B11, 333 (1973).

34. R. Hasegawa, K. Kimoto, Y. Chatani, and H. Tadokoro, Meet. Soc. Cryst. Japan, Abstr., Osaka, Japan, p.21 (1973).

35. K. Haraguchi, T. Kajiyama, and M. Takayanagi, J. Appl. Polym. Sci. 23, 903 (1979).

36. K. Haraguchi, T. Kajiyama, and M. Takayanagi, ibid. 23, 915 (1979).

37. C. Galiotis, I.M. Robinson, R.J. Young, B.J.E. Smith, D.N. Batchelder, Polym. Communs. 26, 354 (1985).

38. C. Chang and S.L. Hsu, unpublished work.

39. W. Glenz and A. Peterlin, J. Macromol. Sci.-Phys. B4, 473 (1970).

40. J.L Koenig, S.W. Cornell, and D.E. Witenhafer, J. Polym. Sci. Part A-2 5, 301 (1967).

41. P.J. Miller, J.F. Jackson, and R.S. Porter, J. Polym. Sci. Polym. Phys. Ed. 11, 2001 (1973).

42. J.E. Lasch, T. Masaoka, D.J. Burchell, and S.L. Hsu, Polym. Bull. 10, 51 (1983).

43. K. Tashiro, M. Kobayashi, and H. Tadokoro, Macromolecules 10, 413 (1977).

44. L. Penn and F. Milanovich, Polymer 20, 31 (1979).

45. L. Penn and F. Larsen, J. Appl. Polym. Sci. 23, 59 (1973).

46. P. McMullen, Composites 15, 222 (1984).

47. J. Delmonte, Technology of Carbon and Graphite Fiber Composites, Van Nostrand, New York (1981).

48. G.S. Holister and C. Thomas, Fiber Reinforced Materials, Elsevier (1966).

49. D.H. Kaelble, Physical Chemistry of Adhesion, Wiley, New York (1971).

50. D.A. Scola, Interfaces in Polymer Matrix Composites, E.P. Pluddemann, ed., pp. 217-284, Academic Press, New York (1974).

51. A.T. DiBenedetto and L. Nicolais, Advances in Composite Materials, G. Piatti, ed., pp. 153-181, Applied Science, London, (1978).

52. S. Wu, Polymer Interface and Adhesion, Marcel Dekker, New York (1982).

53. H.L. Cox, Brit. J. Appl. Phys. 3, 72 (1952).

54. N.F. Dow, General Electric Co. Missile and Space Division, Report No. R63SD61 (1963).

55. B.W. Rosen, Fiber Composite Materials, Ch.3, A.S.M. publications (1964).

56. A. Kelly and W.R. Tyson, J. Mech. Phys. Solids 13, 329 (1965).

57. A.S. Carrara and F.J. McGarry, J. Comp. Mater. 2, 222 (1968).

58. E.D. Reddy, Jr., ibid. 19, 533 (1985).

59. E.D. Reddy, Jr., ibid. 18, 595 (1984).

60. L.J. Broutman and B.D. Agarwal, Polym. Eng. Sci. 14, 581 (1974).

61. B.D. Agarwal and R.K. Bansal, Fibre Sci. Tech. 10, 281 (1977)

62. W.R. Tyson and G.J. Davies, Brit. J. Appl. Phys. 16, 199 (1965).

63. D.M. Schuster and E. Scala, Trans. AIME 230, 1635 (1964).

64. S.W. Tsai and H.T. Hahn, Introduction to Composite Materials, Technomic Publishing Co., Westport, CT (1980).

65. B. Gershon and G. Marom, J. Mater. Sci. 10, 1549 (1975).

66. J.A. Nairn and P. Zoller, J. Mater. Sci. 20, 355 (1985).

67. M.G. Huson and W.J. McGill, J. Polym. Sci. Polym. Phys. Ed. 23, 121 (1985).

68. C.C. Chamis, Proc. ICCM 2, 221 (1978).

69. J.R. Huntsberger, J. Polym. Sci. 43, 582 (1960).

70. S.J. DeTeresa, S.R. Allen, R.J. Farris, and R.S. Porter, J. Mater. Sci. 19, 57 (1984).

71. P.S. Chua and M.R. Piggott, Compos. Sci. Tech. 22, 107 (1985).

72. P.S. Chua and M.R. Piggott, ibid. 22, 185 (1985).

73. I.M. Daniel and A.J. Durelli, Exp. Mechs. 2, 240 (1962).

74. P. So and L.J. Broutman, Polym. Eng. Sci. 16, 785 (1976).

75. H. Dannenberg, SPE J. 21, 669 (1965).

76. H. Poritsky, Physics 5, 406 (1934).

77. J.D. Eshelby, Proc. Roy. Soc. Lond. A241, 376 (1957).

78. P.J. Fritz and R.A. Queeney, J. Compos. Mater. 17, 224 (1983).

79. G.Z. Voyiadjis, P.D. Kiousis, and C.S. Hartley, Exp. Mechs. 25, 145 (1985)

80. W.H. Haslett and F.J. McGarry, Mod. Plasts. 40, 135 (1962).

81. B. Yates, B.A. McCalla, L.N. Phillips, D.M. Kingston-Lee, and K.F. Rogers, J. Mater. Sci. 14, 1207 (1979).

82. Y. Mikata and M. Taya, J. Comp. Mater. 19, 554 (1985).

83. J.A. Narin, Polym. Composites 6, 123 (1985).

84. E.B. Wilson, Jr., J.C. Decius, and P.C. Cross, Molecular Vibrations, McGraw-Hill, New York (1965).

85. P. Groner and H. Gunthard, J. Mol. Spectrosc. 61, 151 (1976).

86. P. Pulay, G. Fogarasi, and J.E. Boggs, J. Chem. Phys. 74, 3999 (1981).

87. A. Dwivedi and S. Krimm, Macromolecules 15, 177 (1982).

88. S. Kashino, K. Ito, and M. Haisa, Bull. Chem. Soc. Jpn. 52, 365 (1979).

89. M. Gussoni and G. Zerbi, Atti. Acc. Naz. Lincei 40, 1032 (1966).

90. T. Cheam, Ph.D. Thesis, University of Michigan (1983).

91. Y. Abe and S. Krimm, Biopolymers 11, 1817 (1972).

92. C. La Lau and R.G. Snyder, Spectrochim. Acta 27A, 2073 (1971).

93. J.H. Schachtschneider and R.G. Snyder, ibid. 19A, 117 (1963).

94. F.J. Boerio and S.K. Bahl, ibid. 32A, 987 (1976).

95. R. Zwarich, J. Smolavek, and L. Goodman, J. Mol. Spectrosc. 38, 336 (1971).

96. T. Miyazawa, J. Polym. Sci. 55, 215 (1961).

97. T. Shimanouchi, M. Asahina, and S. Enomoto, J. Polym. Sci. 59, 93 (1962).

98. I. Sakurada, T. Ito, and K. Nakamae, J. Polym. Sci. C15, 75 (1966).

99. D.Y. Shen, S.E. Molis and S.L. Hsu, Polym. Sci. Eng. 23, 543 (1983).

100. S.N. Zhurkov, V.I. Vettegren, V.E. Korsukov, and J.I. Novak, Fracture 2, 545 (1969).

101. R.P. Wool and R.H. Boyd, J. Appl. Phys. 51, 5116 (1980).

102. L.R.G. Treloar, Polymer 1, 290 (1960).

103. G.S. Fielding-Russell, Text. Res. J. 41, 861 (1971).

104. H. Sugeta and T. Miyazawa, Polymer J. 1, 226 (1970).

105. H. Tsubomura, J. Chem. Phys. 24, 927 (1956).

106. G.B. Carter and V.T.J. Schenk, Structure and Properties of Oriented Polymers, I.M. Ward, ed., Wiley, New York (1975).

107. R.J. Gaymans, J. Tijssen, S. Harkema, and A. Bantjes, Polymer 17, 517 (1976).

108. K. Yabuki, H. Ho, and T. Ota, Sen.-i Gakkaishi 31, T524 (1975).

109. T.F. MacLaughlin, Exp. Mechs. 11, 408 (1971).

110. C.K.L. Davies, S. Turner, and K.H. Williamson, Composites, 16, 250, (1985).

111. C. Galiotis, R.J. Young, P.H.J. Yeung, and D.N. Batchelder, J. Mater. Sci. 19, 3640 (1984).

112. H. Bassler, "Photopolymerization of Diacetylenes" in Advances in Polymer Science, H.-J. Cantow, ed., Vol. 63, pp. 1-45, Springer-Verlag, New York (198).

113. A. Baeyer and L. Lansberg, Ber. Deutsch. Chem. Ges. 15, 57 (1882).

114. G. Wegner, Z. Naturforsch. 246, 824 (1969).

115. G. Wegner, Makromol. Chem. 145, 85 (1971).

116. G. Wegner, ibid. 154, 35 (1972).

117. R.H. Baughman, H.G. Gleiter, and N. Sendfeld, J. Polym. Sci. Polym. Phys. Ed. 13, 1871 (1975).

118. V.K. Mitra, W.M. Risen, Jr., and R.H. Baughman, J. Chem. Phys. 66, 2731 (1979).

119. D.N. Batchelder and D. Bloor, J. Polym. Sci. Polym. Phys. Ed. 17, 569 (1979).

120. C. Galiotis, R.J. Young, and D.N. Batchelder, ibid., 21, 2483 (1983).

121. J. Behringer, Raman Spectroscopy, Vol. 1, Ch. 6, H.A. Szymanski ed., Plenum Press, New York (1967).

122. D. Bloor, L. Koski, G.C. Stevens, F.H. Preston, and D.J. Ando, J. Mater. Sci. 10, 1678 (1975).

123. W.F. Lewis and D.N. Batchelder, Chem. Phys. Lett. 60, 232 (1979).

124. ASTM Standards, D-638, Am. Soc. Test. Mater., Philadelphia, PA (1979).

125. H. Lee and K. Neville, Handbook of Epoxy Resins, Ch. 6, McGraw-Hill, New York (1967).

126. K. Selby and L.E. Miller, J. Mater. Sci. 10, 12 (1975).

127. R.J. Morgan, J. Appl. Polym. Sci. 23, 2711 (1979).

128. R.J. Morgan, F.M. Kong, and C.M. Walkup, Polymer 25, 375 (1984).

129. Dow Chemical Company technical literature.

130. Shell Chemical Company technical literature.

131. R.H. Baughman and E.A. Turi, J. Polym. Sci. Polym. Phys. Ed. 11, 2453 (1973).

132. Advanced Micro Systems Inc. Users Manual for SM-2 Smart Stepper Driver and Controller (1984).

133. D.N. Batchelder and D. Bloor, Advances in Infrared and Raman Spectroscopy, Vol. 11, p.133, R.J.H. Clark and R.E. Hesters, eds., Wiley Heydon, Chichester, 1983.

134. A.H. Nayfeh and S.R. Baker, Fibre Sci. Tech. 10, 139 (1977).

135. K.M. Liechti, Exp. Mechs. 25, 226 (1985).

136. F.S. Chang, J.L. Kardos, and T.J. Tolbert, SPE J. 26, 62 (1970).

137. H.T. Hahn, J. Adhesion 17, 21 (1984).

138. E.P. Pluddemann, Silane Coupling Agents, Plenum Press, New York (1982).

139. L.D. Tyson and J.L. Kardos, Preprints 36th Ann. Conf., Rein. Plast./Comp. Inst., SPI, Sec. 2-E, 1 (1981).

140. D.M. Bigg, Polym. Compos. 7, 69 (1986).

141. W.G. Knauss and H.K. Mueller, Air Force Technical Report, AFRPL-TR-68-125, California Institute of Technology, (1967).

142. F.A. Miller and B.M. Harney, Appl. Spectrosc. 24, 291 (1970).

143. H. Lee and K. Neville, Handbook of Epoxy Resins, P.17-13, McGraw-Hill, New York (1967).

144. A.C. Cottle, W.F. Lewis, and D.N. Batchelder, J. Phys. C: Solid State Phys. 11, 605 (1978).

145. D.N. Batchelder, J. Polym. Sci. Polym. Phys. 14, 1235 (1976).

146. G. Wegner, private communication

147. M.L. Shand, R.R. Chance, M. LePostollec, and M. Schott, Phys. Rev. B 25, 4431 (1982).

148. R.T. Read and R.J. Young, Phil. Mag. A42, 629 (1980).

149. A.S. Argon and M.I. Bessonov, Polym. Eng. Sci. 17, 174 (1977).

150. J.P. Sargent and C. Upstill, Composites 17, 49 (1986).

151. V.R. Riley, J. Comp. Mater. 2, 436 (1968).

152. R.E. Allred, D.Sc. Thesis, Massachusetts Institute of Technology (1983).

Indeterminancy of Force Constants in Redundant Coordinates

Potential energy of a molecule, V

$$V = \frac{1}{2} \sum_{i,j} F_{ij} R_i R_j$$

where R_i's are rectilinear coordinates with one redundancy condition

$$\sum_i g_i R_i = 0.$$

The same potential energycan be written as follow,

$$V' = \frac{1}{2} \sum_{i,j} F_{ij} R_i R_j + \frac{1}{2} A \left(\sum_i g_i R_i \right)^2$$

$$= \frac{1}{2} \sum_{i,j} F_{ij} R_i R_j + \frac{1}{2} A \sum_{i,j} g_i g_j R_i R_j$$

$$= \frac{1}{2} \sum_{i,j} (F_{ij} + A g_i g_j) R_i R_j$$

$$= \frac{1}{2} \sum_{i,j} F'_{ij} R_i R_j \qquad \text{where A = constant.}$$

Since $V' = V$, one would obtain the same eigenvalues and eigenvectors

from the secular equation.

But, force constant matrix is modified from F to F' where

$$F'_{ij} = F_{ij} + A g_i g_j$$

However, only elements for which $g_i g_j \neq 0$ are affected, i.e. force constants for coordinates that are not involved in the redundancy condition remain the same.

Program to Control Stretcher

```
PROGRAM STRETCHER;
(* this program is for controlling SM-2 stepping motor driver and    *)
(* to collect the digitized load cell values from the A/D converter  *)
(* load cell calibration is LOAD = -0.00023+0.05089xTOTAL            *)

VAR
    SERIN, SEROUT :INTEGER;
    CH :CHAR;

PROCEDURE TESTDRV;

VAR
    F :TEXT;
    A,B,C,I,I1,I2,I3,REV,DELAY,PERIOD1  :INTEGER;
    NUM,TOTAL,WEST,RESULT :INTEGER;
    TIME,TOTAL1,PERIOD,P1  :REAL
    FILENAME :STRING;

    BEGIN
        WRITELN('INPUT FILENAME: ');
        READLN(FILENAME);
        ASSIGN(F,FILENAME);
        REWRITE(F);

        WRITELN('ENTER NUMBER OF CYCLE..');
        READLN(NUM);
        WRITELN('ENTER PERIOD IN SECONDS..');
        READLN(PERIOD);
        WRITELN(F,'                         ');
        WRITELN(F,'TIME IN SECONDS    LOAD IN KG      A/D VALUES');
        WRITELN(F,'--------------------------------------------------');

        FOR I1 := 1 TO NUM DO
            BEGIN
                OUT[$5D]:=$2;
                OUT[$5D]:=0;
                FOR I2 := 1 TO 100 DO;
                    A:=ORD(INP[58] & $FF);
                    B:=ORD(INP[5C] & $7);
                    C:=SHL(B,8);
                    TIME:=I1*PERIOD/1.0;
                    TOTAL:=C+4;
```

```
          TOTAL1 :=0.0589*TOTAL;
          WRITELN(F,TIME,'   ',TOTAL1,'    ',TOTAL);
          WRITELN(TIME,'   ','   ',TOTAL);

          PI:=(PERIOD-0.1583)/0.01400;
          PERIOD1 :=ROUND(P1);

          FOR I2:=1 TO PERIOD1 DO
              BEGIN
              FOR I3:=1 TO 500 DO
              END;
          END;

          WRITELN(F,'    ');
          WRITELN(F,'TOTAL NUMBER OF DATA POINT IS',NUM);
          WRITELN(F,'PERIOD OF CONVERT DATA SIGNAL IS',PERIOD,
          ' SECOND');
          WRITELN(APPROXIMATE TOTAL TIME OF A/D DATA AQUISITION
          IS ',NUM*PERIOD,' SECOND');

          CLOSE(F,I1);
          WRITELN('A/D FILE CLOSED; RETURN TO TERMINAL MODE');
          WRITELN('% TO EXIT, @ TO RETURN TO A/D CONVERSIONS');
          WRITELN('OR TYPE COMMANDS TO CONTROL STRETCHER');

     END

PROCEDURE INISERA( BAUD: INTEGER );
(* this will initialize the CCS 2S2P interface        *)
(* port 50H is the CTC chip and must be set for the baud *)
(* rate.  port 58H is the dart and must be set up in the *)
(* proper modes                                        *)

CONST
     BAUD300 = 52;
     BAUD600 = 192;
     BAUD1200 = 96;
     BAUD2400 = 48;
     BAUD4800 = 24;
     BAUD9600 = 12;
     BAUD19200 = 10;

     LOWMODE = $07; (* this is the reset for bauds < 300 *)
     CTCMODE = $47;

BEGIN
     OUT[$55] := 4;
     OUT[$55] := $44;
     OUT[$55] := 5;
     OUT[$55] := $EA'
```

```
        OUT[$55] := 3
        OUT[$55] :=C1;
IF BAUD = 300 THEN
    BEGIN
    OUT[$50] := LOWMODE;
    OUT[$50] := BAUD300;
    END
ELSE
    BEGIN
    OUT[$50] := CTCMODE;
    IF BAUD = 600 THEN OUT[$50] := BAUD600;
    ELSE IF BAUD = 1200 THEN OUT[$50] := BAUD1200;
    ELSE IF BAUD = 2400 THEN OUT[$50] := BAUD2400;
    ELSE IF BAUD = 4800 THEN OUT[$50] := BAUD4800;
    ELSE IF BAUD = 9600 THEN OUT[$50] := BAUD9600;
    ELSE IF BAUD = 19200 THEN OUT[$50] := BAUD19200;
    END;
END; {PROCEDURE INITSERA }

FUNCTION SAOST:BOOLEAN; {TRUE IF OK TO OUTPUT TO SERIAL A}
    BEGIN
    SAOST := (ORD(INP[$55] & $04) <> 0);
    END;

PROCEDURE SAOUT(CH:CHAR); {SERIAL A OUT}
    BEGIN
    REPEAT {} UNTIL (SAOST=TRUE); {PUTS CHAR OUT}
    OUT[$54]:=CH; {SERIAL PORT A OF CCS 2S2P}
    END;

FUNCTION SAIST:BOOLEAN; {TRUE IF CHAR IS AVAIL. AT SER A IN}
    BEGIN
    SAIST := (ORD(INP[$55] & 01) <> 0)
    END;   {EI BIT ONE IS ONE WHEN READY}

FUNCTION SAIN:CHAR; {GET CHAR FROM SERIAL A IN}
    BEGIN REPEAT {} UNITL (SAIST = TRUE)
    SAIN:=CHAR(INP[$54] & $7F); {'&' REMOVES PARITY BIT}
    END; {SAIN}

FUNCTION CONIST:BOOLEAN; {TRUE IF CHAR IS AVAIL. AT CONSOLE
                           INPUT}
    BEGIN
    CONIST := (ORD(INP[$25] & 01) <> 0);
    END; {BIT ONE IS HIGH WHEN READY}

FUNCTION CONIN: CHAR; {GETS CHAR FROM CONSOLE TERMINAL}
    BEGIN
    REPEAT {} UNTIL (CONIST=TRUE);
    CONIN:=CHAR(INP[$20] & $7F);
```

```
                END;  {CONIN}

        BEGIN {MAIN PROGRAM}
                                        {SET UP PARALLEL PORTS}
                OUT[$5A]  := $38;
                OUT[$58]  := $0;
                OUT[$5A]  := $3C;
                OUT[$5B]  := $38;
                OUT[$59]  := $FF;
                OUT[$5B]  := $3C;
                OUT[$5E]  := $38;
                OUT[$5C]  := $0;
                OUT[$5E]  := $3C;
                OUT[$5F]  := $38;
                OUT[$5D]  := $FF;
                OUT[$5F]  := $3C;

                INITSERA(2400);
                SEROUT := ADDR(SAOUT);
                SERIN := ADDR(SAIN);
                WRITELN('% TO EXIT, @ TO CREATE A/D FILE');
                    REPEAT
                    WHILE SAIST DO
                        BEGIN
                            READ([SERIN],CH);  WRITE(CH);
                        END;
                    IF CONIST THEN
                        BEGIN
                            CH:=CONIN;
                            IF  ((CH<>'%')  OR  (CH<>'@'))  THEN
WRITE([SEROUT],CH);
                            IF CH='@' THEN TESTDRV;
                        END;
                    UNTIL CH='%';
                END.
```